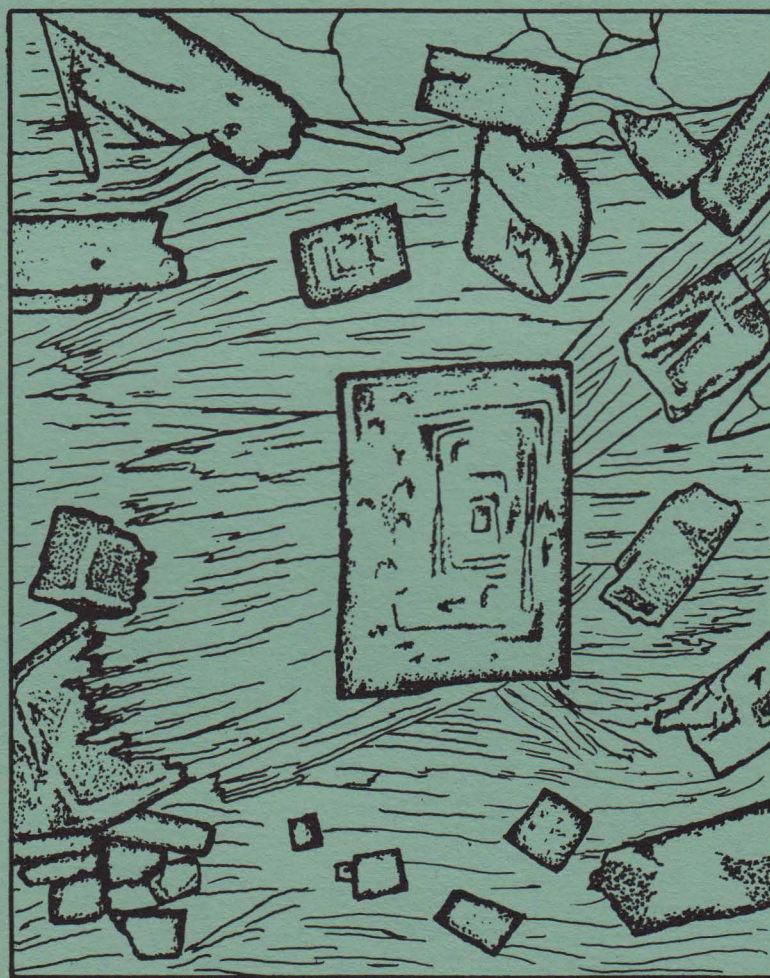


MINERAL CHEMISTRY AND PHASE RELATIONS
IN VOLCANOGENIC SEDIMENTS METAMORPHOSED
TO PUMPELLYTE-ACTINOLITE FACIES,
CHATHAM ISLAND, NEW ZEALAND PLATEAU,
SOUTHWEST PACIFIC

BY JOHN JEFFREY JOSEPHSON



CONTRIBUTION NO. 55
DEPARTMENT OF GEOLOGY & GEOGRAPHY
UNIVERSITY OF MASSACHUSETTS
AMHERST, MASSACHUSETTS

THE MINERAL CHEMISTRY AND PHASE RELATIONS IN VOLCANOGENIC SEDIMENTS
METAMORPHOSED TO THE PUMPELLYITE-ACTINOLITE FACIES,
CHATHAM ISLAND, NEW ZEALAND PLATEAU,
SOUTHWEST PACIFIC
(M.S. Thesis)

by

John Jeffrey Josephson

Contribution No. 55

Department of Geology and Geography

University of Massachusetts

Amherst, Massachusetts

June, 1985

TABLE OF CONTENTS

	Page
ABSTRACT.....	1
INTRODUCTION.....	3
Regional Setting.....	3
Rock Types and Stratigraphy.....	5
Structural and Metamorphic History.....	8
Purpose of Study.....	9
Acknowledgments.....	9
PETROGRAPHY.....	9
Introduction.....	9
Quartz-Albite Schists.....	15
Black Argillaceous Schist.....	17
Greenschists.....	17
Garnet-bearing Schist.....	20
Relations Between Tectonic Fabrics and Metamorphic Recrystallization.....	20
WHOLE ROCK GEOCHEMISTRY.....	22
Analytical Methods.....	22
Introduction.....	22
Major Element Data.....	23
Trace Element Data.....	23
Discussion.....	26
MINERALOGY.....	30
Analytical Procedure.....	30
White Mica.....	30
Thin section description.....	30
Chemistry.....	33
Chlorite.....	40
Thin section description.....	40
Chemistry.....	40
Epidote-Clinzoisite.....	50
Thin section description.....	50
Chemistry.....	50
Pumpellyite.....	54
Thin section description.....	54
Chemistry.....	56
Actinolite-Hornblende.....	66
Thin section description.....	66
Chemistry.....	66
Garnet.....	69
Thin section description.....	69
Chemistry.....	69
Albite.....	72
Thin section description.....	72
Chemistry.....	72
Sphene.....	72
Thin section description.....	72
Chemistry.....	72

Calcite.....	77
Thin section description.....	77
Chemistry.....	77
Quartz.....	77
Minor minerals.....	77
METAMORPHIC PHASE RELATIONS.....	79
Introduction.....	79
$[Al_2O_3 + Fe_2O_3 - Na_2O - K_2O] - [CaO] - [FeO + MgO + MnO]$	79
Epidote Projection.....	81
Chlorite Projection.....	86
Element Partitioning.....	86
Mineral Reactions with Pumpellyite.....	91
Phase Relations and Mineral Reaction Involving Garnet.....	98
$[Al_2O_3 + Fe_2O_3] - [KAlO_2] - [FeO + MgO + MnO]$	105
Conditions of Metamorphism.....	110
CONCLUSIONS.....	113
REFERENCES.....	116

LIST OF TABLES

1. Estimated modes of metamorphic rocks from Chatham Island....	11
2. Hand specimen description of analyzed schist samples.....	12
3. Whole rock major and trace element analyses of Chatham Island schist samples.....	24
4. Electron microprobe analyses of white mica.....	34
5. Electron microprobe analyses of chlorite.....	44
6. Relations between compositional parameters and some optical properties of some chlorites.....	49
7. Electron microprobe analyses of epidote.....	51
8. Electron microprobe analyses of pumpellyite.....	62
9. Electron microprobe analyses of actinolite.....	67
10. Electron microprobe analyses of garnet.....	70
11. Electron microprobe analyses of albite.....	73
12. Electron microprobe analyses of sphene.....	75
13. Electron microprobe analyses of calcite.....	78
14. $(Mg/Fe)_{act}$ vs. $(Mg/Fe)_{chl}$ and $(Mn/Mg)_{pumpellyite}$ vs. $(Mn/Mg)_{chlorite}$	89
15. Electron microprobe analyses of carbonate, and garnet from sample 331.....	99

LIST OF FIGURES

	Page
1. Location map of Chatham Island.....	4
2. Generalized geologic map of the Chatham Islands.....	6
3. Structure section across the western end of Chatham Island....	7
4. Sample location map.....	10
5. Metamorphic textures from two quartz-albite schists.....	16
6. Metamorphic texture of sample 224B.....	19
7. Metamorphic texture of sample 427.....	21
8. Thin section drawing of sample 210B garnet-bearing schist.....	21
9. Whole rock major element variation vs. SiO_2	25
10. Whole rock trace element variation vs. SiO_2	27
11. Zr/TiO_2 vs. Ce discriminant plot of Chatham Island schists....	28
12. Na_2O vs. SiO_2 plot of quartz-albite schists.....	29
13. Zr^2 vs. Nb plot of Chatham Island schists.....	31
14. Whole rock analyses plotted on an ACF diagram.. $2+$	32
15. White mica analyses in terms of $\text{Al}(\text{VI}) - (\text{Mg} + \text{Fe}^{2+} + \text{Mn}) - \text{Fe}^{3+}$..	37
16. Ternary plot of white mica analyses in terms of pyrophyllite- muscovite - leucophyllite.....	39
17. Reciprocal prism diagram illustrating the Fe^{3+} substitution in Chatham Island white micas.....	41
18. $\text{KAlO}_2 - \text{Al}_2\text{O}_3 - \text{NaAlO}_2 - \text{MgO} + \text{FeO} + \text{MnO}$ diagram illustrating the paragonite substitution in white micas.. $3+$	42
19. $\text{Mg}/(\text{Mg} + \text{Fe} + \text{Mn})$ vs. Al_{total} and $\text{Fe}^{3+}/(\text{Fe}^{3+} + \text{Al})$ vs. Al_{total} for white mica analyses.....	43
20. Chlorite microprobe analyses in terms of $\text{Mg}/(\text{Mg} + \text{Fe}^{2+} + \text{Mn})$ vs. Al_{total}	48
21. Frequency diagram of epidote analyses in terms of $\text{Fe}^{3+}/(\text{Fe}^{3+} +$ $\text{Al})$	53
22. Crystal habit of type 1 and 2 pumpellyites.....	55
23. Two different optic orientation diagrams of pumpellyite.....	59
24. Pumpellyite composition space in terms of molecular % $\text{Al}-$ $\text{Fe}^{2+} - \text{Mg}$	60
25. Enlarged pumpellyite composition space illustrating pumpellyite microprobe analyses.....	61
26. Pumpellyite analyses plotted in terms of $\text{Mg}/(\text{Mg} + \text{Fe}^{2+} + \text{Mn})$ vs. $\text{Fe}^{3+}/(\text{Fe}^{3+} + \text{Al})$	65
27. Amphibole classification in terms of Si vs. $\text{Fe}^{2+}/(\text{Fe}^{2+} + \text{Mg})$	68
28. Garnet analyses plotted in terms of Mn - Ca - $(\text{Fe}^{2+} + \text{Mg})$	71
29. Albite analyses plotted on a portion of the feldspar plane....	74
30. Sphene analyses plotted in terms of Al - Ti - Fe^{2+}	76
31. ACF diagram illustrating phase relations of Chatham Island schist samples.....	80
32. Geometry of the epidote projection.....	82
33. Greenschist microprobe analyses projected from epidote onto the basal plane of the $[\text{Al} + \text{Fe}^{3+} - \text{Na} - \text{K}] - [\text{Ca}] - [\text{Mg}] -$ $[\text{Fe}^{2+} + \text{Mn}]$ tetrahedron.....	83

34.	Quartz-albite schist microprobe analyses projected from epidote onto the basal plane of the $[Al+Fe^{3+}-Na-K] - [Ca] - [Mg] - [Fe^{2+}+Mn]$ tetrahedron.....	84
35.	Summary epidote projection of Chatham Island schist samples..	85
36.	Geometry of the chlorite projection.....	87
37.	Modified chlorite projection illustrating phase relations for schist samples.....	88
38.	(Mg/Fe^t) actinolite vs. (Mg/Fe^t) chlorite.....	90
39.	(Mn/Mg) pumpellyite vs. (Mn/Mg) chlorite.....	92
40.	Modified chlorite projection illustrating ferric pumpellyite consuming reaction.....	94
41.	Chlorite projection used to illustrate ferric pumpellyite consuming reaction with microprobe data from sample 224B.....	94
42.	Predicted change of Mg ratio for the assemblage pumpellyite-chlorite- actinolite depicted on an epidote projection.....	95
43.	Equilibrium domains schematically illustrated on an $[Al_2O_3 + Fe_2O_3] - [CaO] - [MgO+FeO+MnO] - [KA1O_2]$ tetrahedron (sample 77).....	96
44.	ACF diagram illustrating a possible reaction for the three phase assemblage chlorite-pumpellyite-actinolite.....	97
45.	Microprobe data from carbonate nodule (sample 331) and garnet-bearing schist sample (210) plotted in terms of Ca - Fe+Mg - Mn.....	100
46.	ACF diagram illustrating phase relations of garnet-bearing schist sample 210.....	102
47.	Schematic $[Al_2O_3 + Fe_2O_3] - [CaO] - [MnO] - [FeO + MgO]$ tetrahedron illustrating phase relations in garnet-bearing schist sample 210B.....	103
48.	Epidote projection of mineral analyses onto the basal plane of the $[Al_2O_3+Fe_2O_3] - [CaO] - [FeO+MgO] - [MnO]$ tetrahedron illustrating phase relations and reaction direction for a garnet-forming reaction.....	104
49.	AKF diagram illustrating common phases in low-grade metamorphic rocks.....	106
50.	AKF diagram illustrating white chlorite phase relations.....	108
51.	Averaged white mica and chlorite analyses plotted in terms of the $(Mg+Fe^{2+}+Mn + Si) = (Al + Al)$ substitution.....	109
52.	Schematic chlorite projection illustrating the change in white mica composition during a continuous pumpellyite-consuming reaction.....	111

ABSTRACT

The metamorphic rocks of Chatham Island, 800 km east of New Zealand, are the only on-land exposures of the eastern half of the so-called "New Zealand Geosyncline". They represent a stratified sequence dominated by water-laid volcanogenic sediments of dacitic composition, with subordinate terrigenous graywacke and minor intermediate to mafic tuffs and cherts, that were probably deposited in the Permian or Triassic. These were multiply deformed and metamorphosed to the pumpellyite-actinolite facies during the Jurassic-Cretaceous Rangitata Orogeny.

Whole rock analyses on characteristic rock types indicate that quartz-albite schists are a compositionally homogenous series of metamorphosed volcanogenic sediments of dacitic to rhyodacitic composition, while greenschists are chemically heterogeneous and are probably chemically altered and metamorphosed mafic tuffs.

Metamorphic mineral assemblages in the quartz-albite schists and greenschists include quartz, albite, white mica, epidote, pumpellyite, actinolite, chlorite, calcite, and sphene. Microprobe analyses of the minerals indicate that the white mica is phengite with Si per 11 oxygens

of 3.40 to 3.54, $Mg/(Mg + Fe^{2+} + Mn)$ of 0.70 to 0.97, $Fe^{3+}/(Fe^{3+} + Al)$ of 0.04 to 0.10 and $K/(K + Na)$ from 0.969 to 0.993. Chlorite has

$Mg/(Mg + Fe^{t} + Mn)$ from 0.386 to 0.534, and total Al varies as a function of mineral assemblage and localized mineral equilibrium. Epidote has

$Fe^{3+}/(Fe^{3+} + Al)$ from 0.136 to 0.326 and, in general, is zoned from ferric cores to aluminous rims. Both relict ferric pumpellyite and Mg-Al pumpellyite are present in all analyzed samples. Detailed petrographic study on unusually well developed crystal faces of Mg-Al pumpellyite suggest that some grew as hollow-ended "hopper" crystals. Mg-Al pumpellyite in one greenschist sample has a different optic orientation than previously reported. This pumpellyite has the X vibration direction, as opposed to the Y vibration direction, parallel to the b -axis that is the long direction of the crystal. The change in optic orientation is thought to be a function of the iron content. The Mg-Al pumpellyite is similar in composition to pumpellyite from other intermediate to high pressure metamorphic terranes. Cation-normalized

microprobe data indicate that $Mg/(Mg + Fe^{2+} + Mn)$ varies in these pumpellyites from 0.675 to 0.819 in greenschists and from 0.366 to 0.824 in quartz-albite schists. Actinolites are typically low in Al and Na although some rim analyses have Al up to 0.467 and Na up to 0.255 per

formula unit. $Mg/(Mg + Fe^{2+} + Mn)$ varies from 0.568 to 0.628 in quartz-albite schists and from 0.616 to 0.643 in greenschists. All plagioclase analyzed is albite with composition ranging from An_0 to $An_{.009}$.

Graphical analysis of quartz-albite schists and greenschist assemblages in the system $\text{SiO}_2\text{-Al}_2\text{O}_3\text{-Fe}_2\text{O}_3\text{-CaO-MgO-FeO-MnO}$ indicates two three-phase ferromagnesian assemblages coexisting with quartz, albite, and sphene with or without white mica. These are pumpellyite-chlorite-epidote, and pumpellyite-chlorite-actinolite. Rocks with the actinolite assemblage also contain ferric epidote stabilized as an additional phase by Fe_2O_3 . Element fractionation indicates that $\text{XMg pumpellyite} >$

$\text{XMg actinolite} > \text{XMg chlorite}$. The continuous reaction that seems to be responsible for the actinolite-bearing assemblages is $\text{Fe}^{3+}\text{-pumpellyite+chlorite} = \text{epidote} + \text{actinolite} + \text{more aluminous pumpellyite}$. This reaction in chlorite-rich rocks will produce more magnesian product assemblages until all pumpellyite is consumed. In pumpellyite-rich rocks the reaction produces more magnesian product assemblages until all chlorite is consumed. In rocks without actinolite, ferric pumpellyite and aluminous chlorite are continuously consumed while less aluminous chlorite, epidote and aluminous pumpellyite are formed.

An unusual garnet-bearing schist contains the assemblage quartz-albite-epidote - Mn-calcite -garnet-chlorite- white mica -sphene. Microprobe analyses indicate the following mineral compositions:

epidote- $\text{Fe}^{3+}/(\text{Fe}^{3+}+\text{Al}) = 0.136$ to 0.341 ; garnet - spessartine 0.482 , grossular 0.370 , almandine 0.112 , ranging to spessartine 0.361 , grossular 0.433 almandine 0.196 ; chlorite- $\text{Mg}/(\text{Mg}+\text{Fe}^{3+}+\text{Mn}) = 0.456$ (cores) to 0.488 (rims), calcite-calcite 0.959 , rhodochrosite 0.024 ranging to calcite 0.967 , rhodochrosite 0.009 . Garnet seems to have formed by a continuous dehydration decarbonation reaction: $\text{Mn-calcite} + \text{epidote} + \text{chlorite} = \text{garnet} + \text{H}_2\text{O} + \text{CO}_2$.

White mica is the only additional phase in Chatham Island schists when K_2O is considered as an additional component. The close spatial association of white mica and pumpellyite suggests that a continuous reaction: $\text{muscovite} + \text{Fe}^{3+}\text{-pumpellyite} = \text{phengite} + \text{chlorite} + \text{epidote} + \text{aluminous pumpellyite} + \text{H}_2\text{O}$ has occurred in these rocks.

The mineral chemistry and element fractionation between metamorphic minerals in Chatham Island schists are compatible with metamorphism at temperatures between 270 and 340°C , and pressures of 4.8 to 7 kbars.

INTRODUCTION

Relatively few detailed studies of mineral compositions and phase equilibria in metamorphosed volcanic sediments in the pumpellyite-actinolite facies have been published. The few important contributions include those of Kawachi (1975), who studied pumpellyite-actinolite facies metamorphosed volcanogenic sediments from the upper Wakatipu area, New Zealand, and Coombs et al. (1976), who analyzed pumpellyite-actinolite facies graywackes and intercalated slates from Loeche, Switzerland.

The pumpellyite-actinolite facies (Seki, 1969) separates very low grade zeolite and prehnite-pumpellyite facies rocks from low-grade greenschist facies and high pressure blueschist facies rocks. Pumpellyite-actinolite facies schists derived from volcanogenic sediments, marine clays, and muds may have relict igneous or clastic mineral cores with recrystallized metamorphic rims, or the schists may be completely recrystallized. Primary sedimentary and volcanogenic textures are common, but many pumpellyite-actinolite facies rocks have metamorphic deformational textures. The deformation associated with this type of metamorphic regime is thought to be transitional between non-penetrative deformation and deformation that is responsible for commonly observed penetrative structural features such as schistosity and preferred mineral orientation (Bishop, 1972; Coombs et al., 1976).

This thesis contributes to a better understanding of mineral chemistry, phase equilibria, whole rock chemistry, and some micro-structural interpretations of pumpellyite-actinolite facies schists derived from metamorphosed volcanogenic sediments from the Chatham Islands, New Zealand Plateau, Southwest Pacific.

Regional Setting

The Chatham Islands are located approximately eight hundred kilometers southeast of the North Island of New Zealand (Figure 1) and are the easternmost on-land exposure of the Chatham Rise that has been determined to be continental in nature based on geophysical evidence and dredge samples (Adams and Robinson, 1977). Paleogeographic reconstructions, plate tectonic models, and similarities in stratigraphy, deformation, and metamorphism suggest that the schistose rocks of the Chatham Rise and the Chatham Islands are a part of the Haast schist belt (Coombs et al., 1976) of the Torlesse facies, which is one of the two stratigraphic and structural subdivisions (Landis and Bishop, 1972) of the "New Zealand Geosyncline" (Wellman, 1952; Reed, 1957; Grindley et al., 1961; Landis, 1969; Dickinson, 1971; Landis and Bishop, 1972) or the Rangitata terrane (Coombs et al., 1976; Carter and Norris, 1977; Crook and Feary, 1982). The Haast schist belt extends along much of the entire length of the South Island of New Zealand (Figure 1) and is believed to have formed from volcanics and sediments, possibly derived from a now absent eastern source area (Coombs et al., 1976), during periods of plate divergence and plate consumption from the

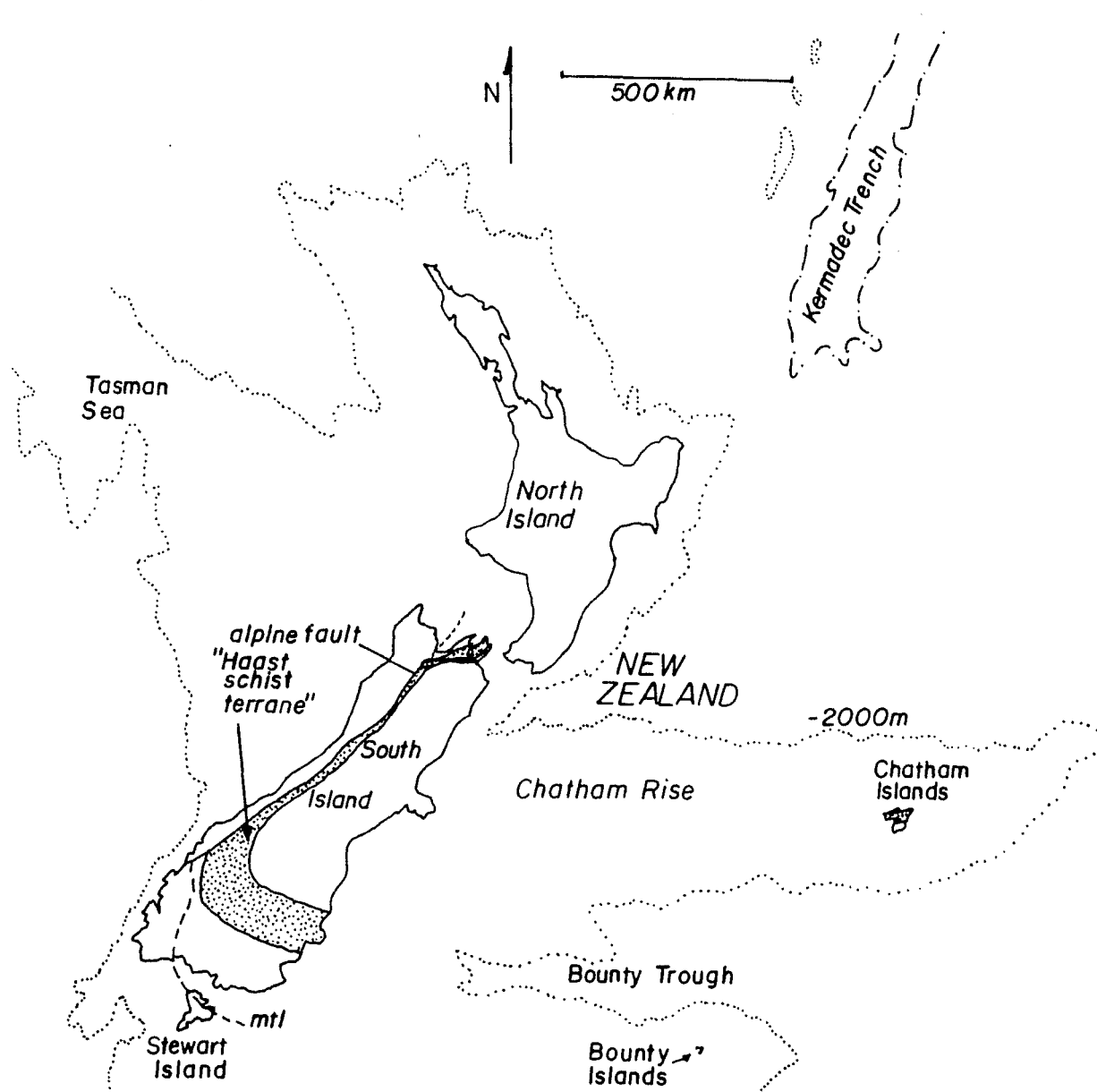


Figure 1. Location map of the Chatham Islands. The islands are located at the eastern end of the Chatham Rise. The New Zealand Plateau is delineated by the -2000 meter contour. mtl = median tectonic line (Landis and Bishop, 1972), marking the western margin of the "New Zealand Geosyncline".

Permian through the Triassic. These deposits were then deformed and metamorphosed during the late Jurassic Rangitata Orogeny when the plate margin became totally consuming and some Torlesse facies rocks were dragged along a west-directed subduction zone under the New Zealand region into juxtaposition against the Caples-Pelorus terrane (Coombs et al., 1976; Landis and Bishop, 1972; Crook and Feary, 1982; Fleming, 1970).

The general geology of the Chatham Islands has been summarized by Hay et al. (1970). The stratigraphy, structure, and metamorphism of the pre-Cretaceous basement schists has been described briefly by Robinson (Adams and Robinson, 1977). The schists are overlain by younger undeformed Late Cretaceous and Tertiary sediments (Grindley et al., 1977).

The basement schists are a stratified sequence of water-laid dacitic volcanic sediments with subordinate terrigenous graywacke, and minor intermediate to mafic tuffs and cherts. The sequence is thought to have been deposited in the Permian or Triassic and was metamorphosed to the pumpellyite-actinolite facies during the Jurassic-Cretaceous Rangitata Orogeny (Adams and Robinson, 1977).

Rock Types and Stratigraphy

The Chatham Island schists have been subdivided by Robinson (Adams and Robinson, 1977) into three stratigraphic units based on the proportions of four major and two minor rock types. The rock types are:

- 1) Medium- to coarse-grained quartz-albite schists interpreted to have been dacitic pyroclastic material or water-laid tuffs deposited in a marine environment. The quartz-albite schists also contain white mica, chlorite, epidote, pumpellyite, and actinolite.
- 2) Very fine-grained green argillaceous schists consisting of quartz, albite, epidote, sphene, pumpellyite, actinolite, and a higher proportion of white mica and chlorite than the quartz-albite schists. These are interpreted to have been finer-grained volcanogenic sediments.
- 3) Black argillaceous schists interpreted to have been marine black shales, consisting of quartz, albite, white mica, chlorite, epidote, carbonaceous matter, and pyrite.
- 4) Graywackes and graywacke schists which contain detrital micas and rock fragments indicating a terrigenous source terrane composed of metamorphic rocks.

Minor rock types are:

- 1) Greenschists, which are interpreted to have been water-laid tuffs of intermediate to mafic composition. The greenschists contain quartz, albite, chlorite, epidote, pumpellyite, actinolite, white mica, and sphene.
- 2) Cherts or siliceous schists which contain quartz, albite, spessartine-rich garnet, Ca-Mn carbonate, chlorite, epidote and sphene.

The three stratigraphic units (Figure 2) are characterized as follows: The Teraki Formation, a 2000 meter thick section, is the

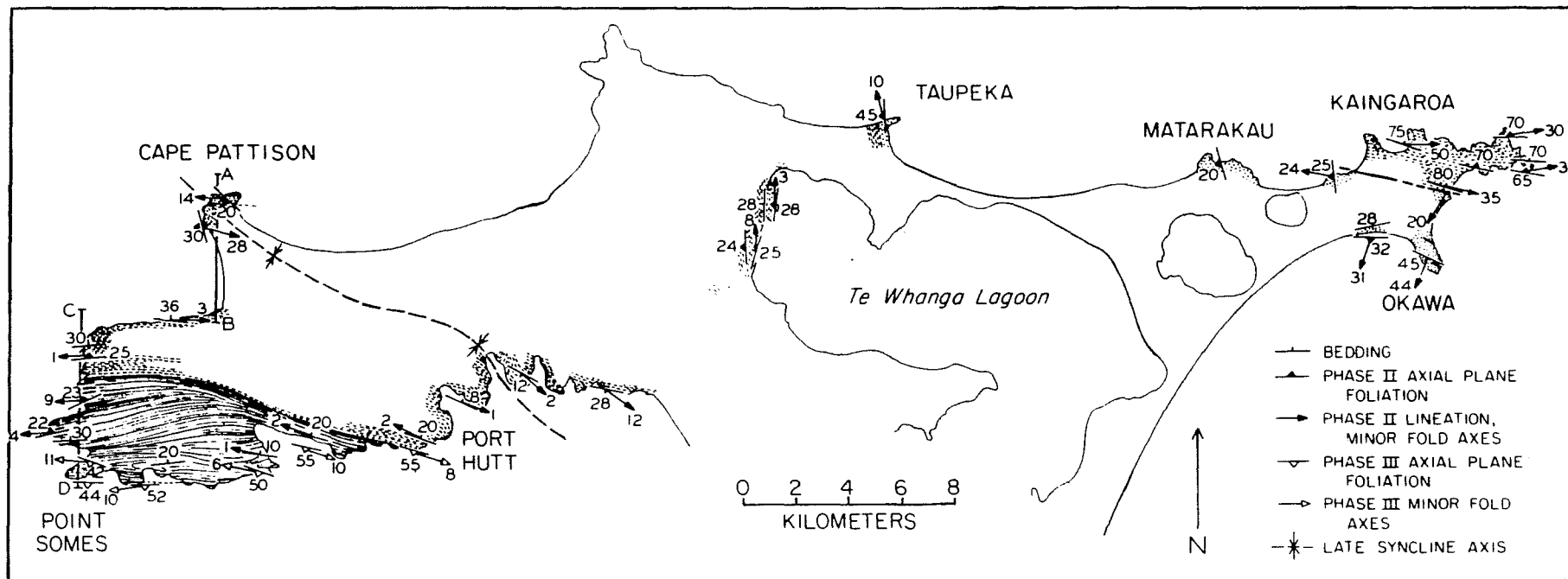


Figure 2. Generalized geologic and structure map of pre-Cretaceous basement rocks of northern Chatham Island. Stratigraphic units from oldest to youngest are: "Teraki Formation" (solid line pattern with individual greenstone beds exaggerated in heavy black); "Kaingaroa Volcanics" (short-dashed line pattern); and "Matarakau Greywacke" (stippled pattern with individual greenstone beds exaggerated in heavy black). Lines of cross sections A-B, and C-D (Figure 3) are indicated on the west coast, from Cape Pattison to Point Somes (Adams and Robinson, 1977).

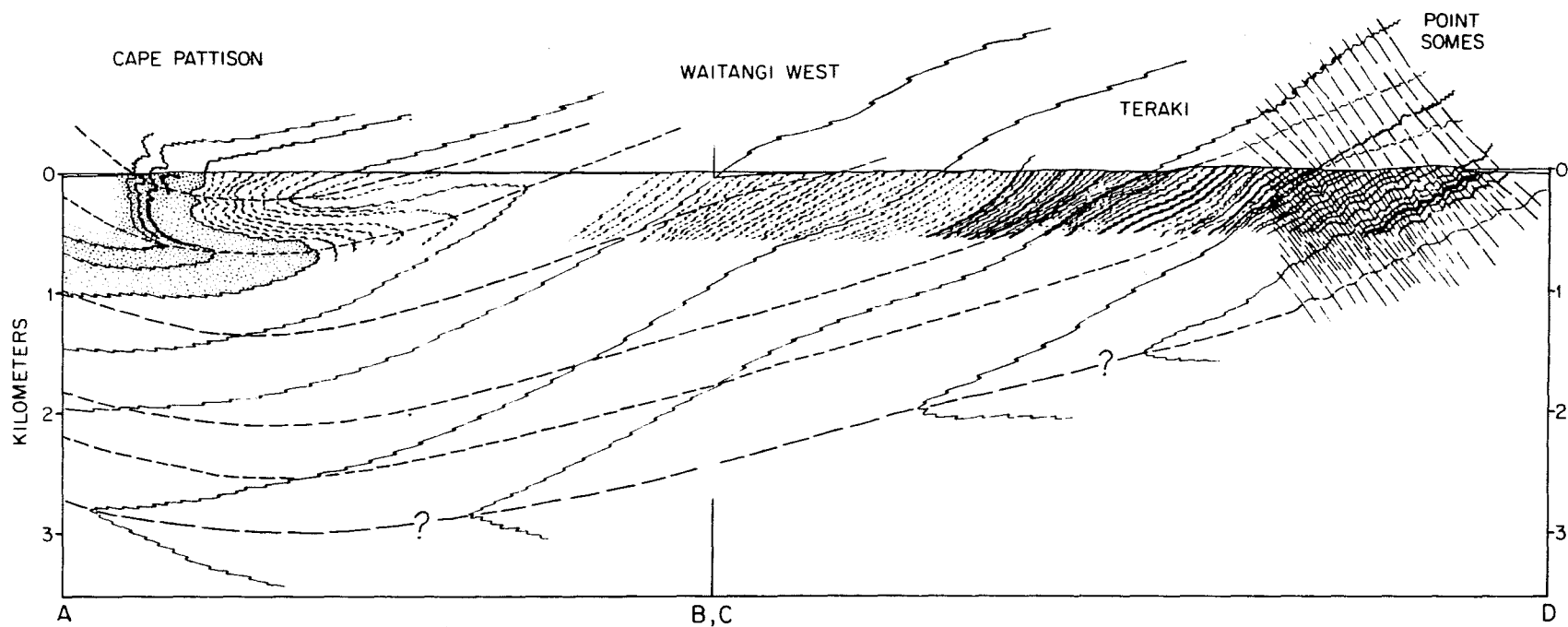


Figure 3. Geologic structure section along lines A-B, and C-D at west end of Chatham Island. Stratigraphic units from oldest to youngest (right to left) are "Teraki Formation" (solid line pattern with individual greenstone beds exaggerated in heavy black); "Kaingaroa Volcanics" (short-dashed line patterns); and "Matarakau Greywacke" (stippled pattern with individual greenstone beds exaggerated in heavy black). Gently dipping long-dashed lines are Phase II axial plane foliation folded into a broad late syncline near Cape Pattison. Phase III folds and axial plane foliation are superimposed on earlier features near Point Somes (Adams and Robinson, 1977).

oldest and the lowest portion of the stratigraphic section. The Teraki Formation consists of approximately 30% quartz-albite schist, 35% green argillaceous schist, and fourteen distinct greenschist beds ranging in thickness from one to five meters. The Kaingaroa Volcanics, which are 2000 meters thick, overlie the Teraki Formation and are characterized by interbedded quartz-albite schist 70%, green argillaceous schist 20%, and black argillaceous schist 10%. The upper 750 meters of the stratigraphic column is the Matarakau Graywacke characterized by graded graywacke and black argillite, but also containing some greenschist, chert, green argillaceous schist, and quartz-albite schist.

Structural and Metamorphic History

The structural history of the metamorphic rocks of Chatham Island is divided by Robinson into three phases (Adams and Robinson, 1977). A cross section (Figure 3) from Adams and Robinson (1977) is provided to assist the reader.

Phase 1: Folding of strata into northwest-trending minor folds and the formation of mineral lineations. Formation of a metamorphic foliation defined by the parallel alignment of interlocking micaceous minerals and/or actinolite in quartz-albite schists and micaceous greenschists, and actinolite-chlorite alignment in greenschists.

Phase 2: Folding of earlier foliation and lineation into a large recumbent anticline with overturning from south towards the north, and formation of an axial plane foliation. At the west end of Chatham Island the foliation dips gently north at an angle less steep than bedding, and nearly horizontal minor folds trend east-west. Movement line orientation was determined to be N40W 25NW.

Phase 3: Formation of a moderately steep south-dipping crenulation cleavage and slip cleavage in the southwest portion of Chatham Island with local concentration of metamorphic minerals along cleavage surfaces.

Later faulting and rotation of the basement rocks in the northeastern portion of Chatham Island occurred and is responsible for the unusual orientation of structural features in that area (Figure 2).

Metamorphic recrystallization is thought to have occurred primarily during the second phase of deformation, but locally mineral segregation and growth occurred along phase 3 slip cleavage (Adams and Robinson, 1977). Results of K-Ar ages on quartz-albite schist and greenschist whole-rock samples, and white mica-chlorite separates by Adams and Robinson (1977) indicate that metamorphism occurred at least as long ago as 164 m.y., although some ambiguity exists due to older ages of 168, 171, and 193 m.y. Adams and Robinson (1977) concluded that most metamorphic micas in the Chatham schists passed through their blocking temperature about 164 m.y ago but that the main metamorphic event was probably earlier at 193 m.y.

Purpose of Study

The purpose of this study was to examine in detail the petrography, mineral chemistry, and mineral phase relations of some typical metamorphosed volcanogenic sediments from Chatham Island. Metamorphic reactions that are important are proposed and discussed. Also, whole rock analyses of typical Chatham Island schists were obtained to characterize chemically the metamorphic rocks. This study helps to clarify the relationships between deformation and metamorphism of Chatham Island schists. In a more general way it points the way toward future studies concerned with the mineral chemistry and metamorphism of the "Rangitata terrane" and other worldwide occurrences of pumpellyite-actinolite facies rocks associated with plate margins.

Acknowledgments

The author thanks Peter Robinson for suggesting the topic of this study and providing the samples. I also appreciate and thank Peter Robinson for sacrificing many hours during numerous thought provoking sessions, and for critical review and suggestions. I also thank L. M. Hall and J. T. Cheney for helpful discussions, careful review, and numerous suggestions.

I thank John Brady and the Department of Geology at Smith College for the teaching assistantship during the 1982-1983 year. I thank the Department of Geology and Geography at the University of Massachusetts for the teaching assistantship, financial aid, and numerous jobs. Also thanks go to Carol Birney, Peter Morton, and Stephen Field for emergency loans.

I thank my sister Kim and her family, and my brother Greg and his wife for moral support. I thank my father, John W. Josephson for his moral and financial support, and my mother, Elizabeth J. Josephson for moral support, financial aid and continued encouragement even during a courageous but unsuccessful fight for life during the fall and winter of 1983-1984.

PETROGRAPHY

Introduction

This section covers the petrography of Chatham Island schist samples chosen for microprobe studies of coexisting minerals and/or chemical analyses for major and trace elements. Particular emphasis is placed on describing the degree that the compositional layering and metamorphic mineral segregation have developed during the deformational history. This information is used to infer how the deformational history and metamorphism are related in Chatham Island schists. A detailed description of each mineral is in the Mineralogy section. Figure 4 is a sample location map. Table 1 gives modes of each sample, and Table 2 gives hand-specimen descriptions of each sample.

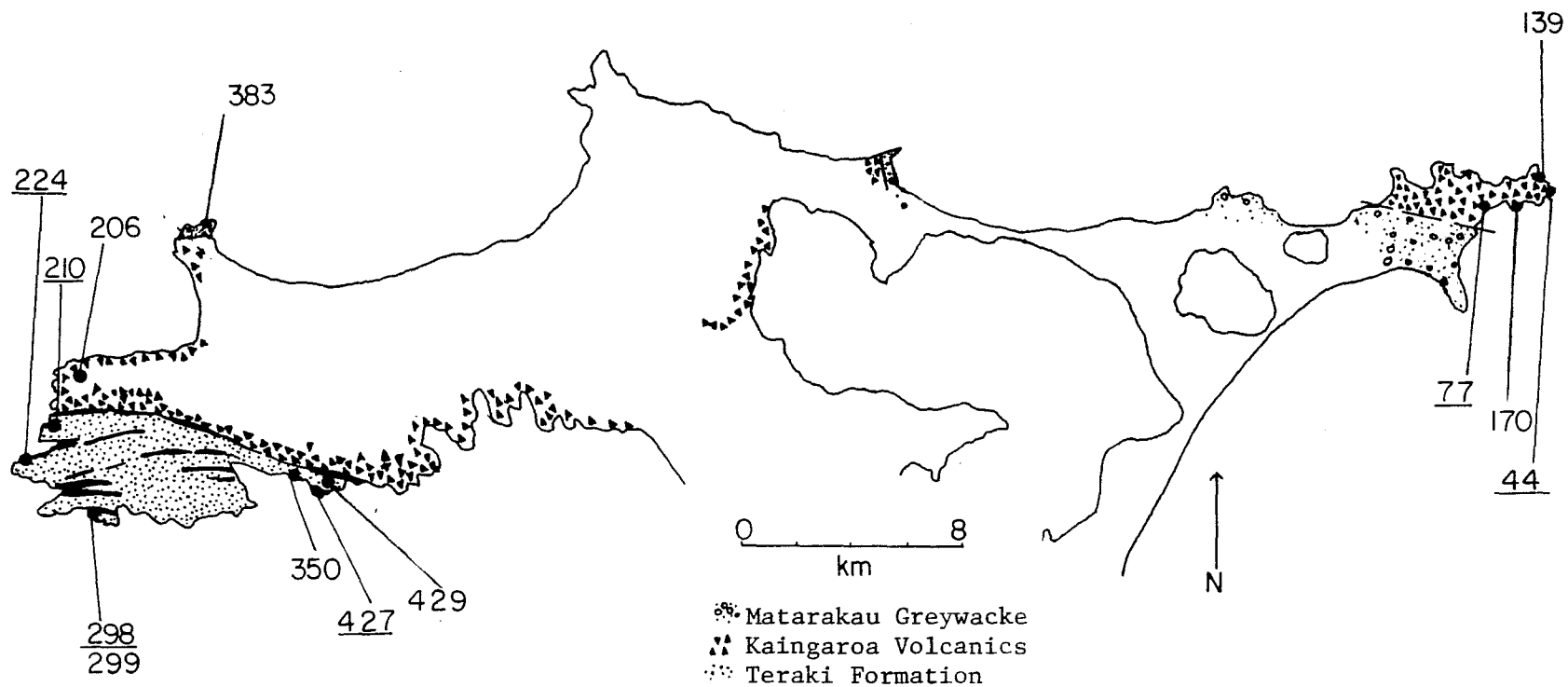


Figure 4. Sample location map. Underlined samples were chosen for microprobe analysis. Heavy lines in the Teraki Formation are individual greenschist beds which have been exaggerated for clarity.

Table 1. Estimated modes of metamorphic rocks from Chatham Island.

Number	quartz-albite schists						argillaceous schist	greenschists					garnet-bearing schist
	44*	77*	139	170	206	298*		383A	224B*	299	427*	429	
quartz	38	39	33	34	39	44	46	19	24	17	28	14	37
albite	29	24	32	30	37	29	28	21	23	30	24	17	18
white mica	17	13	19	16	13	16	20			21			8
epidote	6	9	7	8	9	4	tr	24	13	4	7	29	9
chlorite	7	7	9	tr	2	4	4	14	19	19	25	38	10
pumpellyite	3	3		tr		3		tr	5		13		
actinolite		5		10				17	14				
sphene	tr	tr	tr	2	tr	tr	1	3	2	4	3	2	2
ilmenite	tr	tr	tr	tr	tr	tr	tr	tr	tr	tr	tr	tr	tr
apatite	tr	tr	tr	tr	tr	tr	tr	?	tr	tr	tr	tr	tr
calcite								2	tr	5		tr	5
<u>garnet</u>													<u>11</u>
zircon	tr	tr	?	?	tr	tr							
pyrite							1						tr
<u>chalcopyrite</u>									tr				
Total	100	100	100	100	100	100	100	100	100	100	100	100	100

* = microprobe samples

tr = trace amounts

Table 2. Hand specimen description of Chatham Island schists.
Stratigraphic units of samples are shown on Figure 4.

Quartz-albite schists

44. Green, fine-grained, quartz-albite schist. Primary quartz and albite occur as ellipsoids with short axes perpendicular to foliation. The shape of the grains is presumably due to grain-size reduction and elongation parallel to a strong second phase foliation.
77. Compositionally massive, well foliated quartz-albite schist. Contains larger recognizable primary grains of feldspar and quartz in a very fine-grained matrix. Edges of primary quartz and albite grains show tectonically induced grain-size reduction. They are elongated parallel to metamorphic foliation. Later quartz veins cut across foliation.
139. Light-green, fine-grained, well bedded quartz-albite schist. Metamorphic foliation is well developed and is at a low to moderate angle to bedding. Bedding is defined by alternating thin dark layers and light colored layers which contain recognizable clasts of quartz that are elongate parallel to the foliation. A lineation defined by oriented white mica is parallel to the intersection of foliation and bedding.
170. Fine-grained, gray quartz-albite schist. This sample has a massive appearance but does have a metamorphic foliation with an associated mineral lineation defined by oriented white mica and chlorite.
206. Light-green, well layered, quartz-albite schist. The compositional layering is defined by quartz and feldspar-rich layers, which alternate with layers composed of white mica, and other fine-grained minerals. A metamorphic foliation appears to be essentially parallel to the layering.
298. Well layered, light green, quartz-albite schist. Layers are defined by compositional differences between the green matrix composed of white mica, chlorite, epidote, and pumpellyite, and layers of white mica and light-blue quartz and feldspar. A pronounced second phase mineral lineation defined by oriented white mica and chlorite is present on foliation surfaces. A cross-cutting third phase foliation can only be seen in thin section.

Table 2 (cont.)

Black argillaceous schist

350. Gray and black, very fine-grained argillaceous schist. A compositional layering defined by alternating quartz and albite layers with mica and chlorite layers. A lineation defined by crenulated white mica is on foliation surfaces. Small asymmetrical third phase folds deform earlier foliation. A mica lineation associated with the third phase folds is present.

Greenschists

383. Very fine-grained chlorite actinolite greenschist. Chlorite and actinolite are interlocked and aligned parallel to form foliation surfaces. This foliation is complexly folded into tight symmetrical folds.
- 224B. Very fine-grained foliated greenschist. Second phase deformational structures dominate the fabric of this rock. They include a pronounced solution cleavage that is axial planar to minor second phase folds. Small, tight, second phase folds are truncated against solution surfaces. A light colored mineral optically identified as sphene has aggregated along the solution surfaces.
299. Fine-grained chlorite-white mica greenschist. Pronounced third phase mineral lineation formed by crenulation of white mica and chlorite on foliation surfaces is associated with tight third phase folds. An axial planar solution cleavage with fine-grained mineral aggregates is visible on the sawed slab.
429. Fine-grained massive to poorly foliated yellow-green greenschist which has late calcite veins that cut across layering. A second phase lineation defined by parallel aligned epidote and crenulated chlorite is visible.
427. Fine-grained yellowish green to bluish green compositionally layered greenschist. Although compositionally layered, the rock has a generally massive appearance. The sawed slab shows fine-grained layering wrapping around larger quartz and albite grains. Yellow blotches are possibly weathering. A conspicuous dark band of sphene forms a margin along a quartz-calcite layer.

Table 2 (cont.)

Garnet-bearing schist

- 210B. Fine-grained garnet bearing schist composed of epidote, chlorite, white mica, calcite, albite, quartz, and sphene. A compositional layering defined by alternating quartz, albite, and calcite layers with mica, chlorite, epidote, and garnet layers is deformed by a second phase cleavage that has calcite and quartz along the cleavage surfaces. Two mineral lineations can be observed. One lineation is defined by oriented, interlocked white mica and chlorite, while a later lineation is defined by crenulated, interlocked white mica and chlorite.

Quartz-Albite Schists

Sample 44 is from the Kaingaroa Volcanics in the northeastern part of Chatham Island. This rock is characterized by a poorly developed second phase foliation defined by lenses formed from partially crushed primary quartz and albite grains separated by a thin, interlocking, parallel-aligned, matrix of white mica, and chlorite. The white mica-chlorite matrix also contains epidote which is zoned and has green cores and colorless rims, three types of pumpellyite, anhedral and subhedral sphene, brownish and dusty-appearing apatite, relict zircon, relict ilmenite, relict quartz and plagioclase phenocrysts, and one fragmented relict amphibole which has light brown and green pleochroism and is surrounded by a very thin actinolite rim. The quartz and albite relict phenocrysts range from 0.5 mm. up to 2 mm. in diameter and these are much larger than the metamorphic quartz and albite which are from 0.05 mm. up to 0.1 mm. in diameter. The white mica-chlorite foliation wraps around the relict phenocrysts, which are represented by single crystal cores surrounded by finely segmented exteriors, together forming lens-shaped volumes. The fine-grained portions of the lenses are considered to be the product of strain-induced dynamic recrystallization. The lenses are elongated in the plane of the foliation and shortened perpendicular to the plane of the foliation. Most of the albites that are relict plagioclase phenocrysts have cores that are riddled with pumpellyite. The majority of the pumpellyite, however, occurs as anhedral, pale green to colorless pleochroic individual crystals or crystal aggregates within the matrix or as subhedral to euhedral colorless crystals within the micaceous layers. The parallel alignment of the mica layers is pervasive throughout the entire thin section, but there is little evidence of metamorphic segregation between the mica-rich matrix and deformed quartz and albite clasts. Figure 5a illustrates the metamorphic fabric in sample 44.

Sample 77 is very similar to sample 44 except that it contains actinolite. The actinolite occurs in the mica-rich matrix, but does not have a preferred orientation. Most actinolite crystals have grown as individual subhedral and euhedral crystals but there are also some crystal aggregates. As in sample 44, white mica and chlorite are aligned parallel to each other and are interlocked. This foliation wraps around relict volcanic plagioclase and quartz phenocrysts. The recrystallization and flattening of the phenocrysts is not so pronounced in sample 77 as in sample 44. Again the majority of the pumpellyite in this rock is anhedral and pleochroic, whereas lesser amounts of nonpleochroic euhedral pumpellyite occur in the foliation. Cores of albites also contain pumpellyite.

Sample 139 is a fine-grained quartz-albite schist characterized by a metamorphic foliation defined by parallel alignment of white mica and chlorite grains. The foliation wraps around flattened relict quartz and plagioclase phenocrysts. The rock also contains epidote, sphene, and relict ilmenite. Like samples 44 and 77 the actual segregation of white

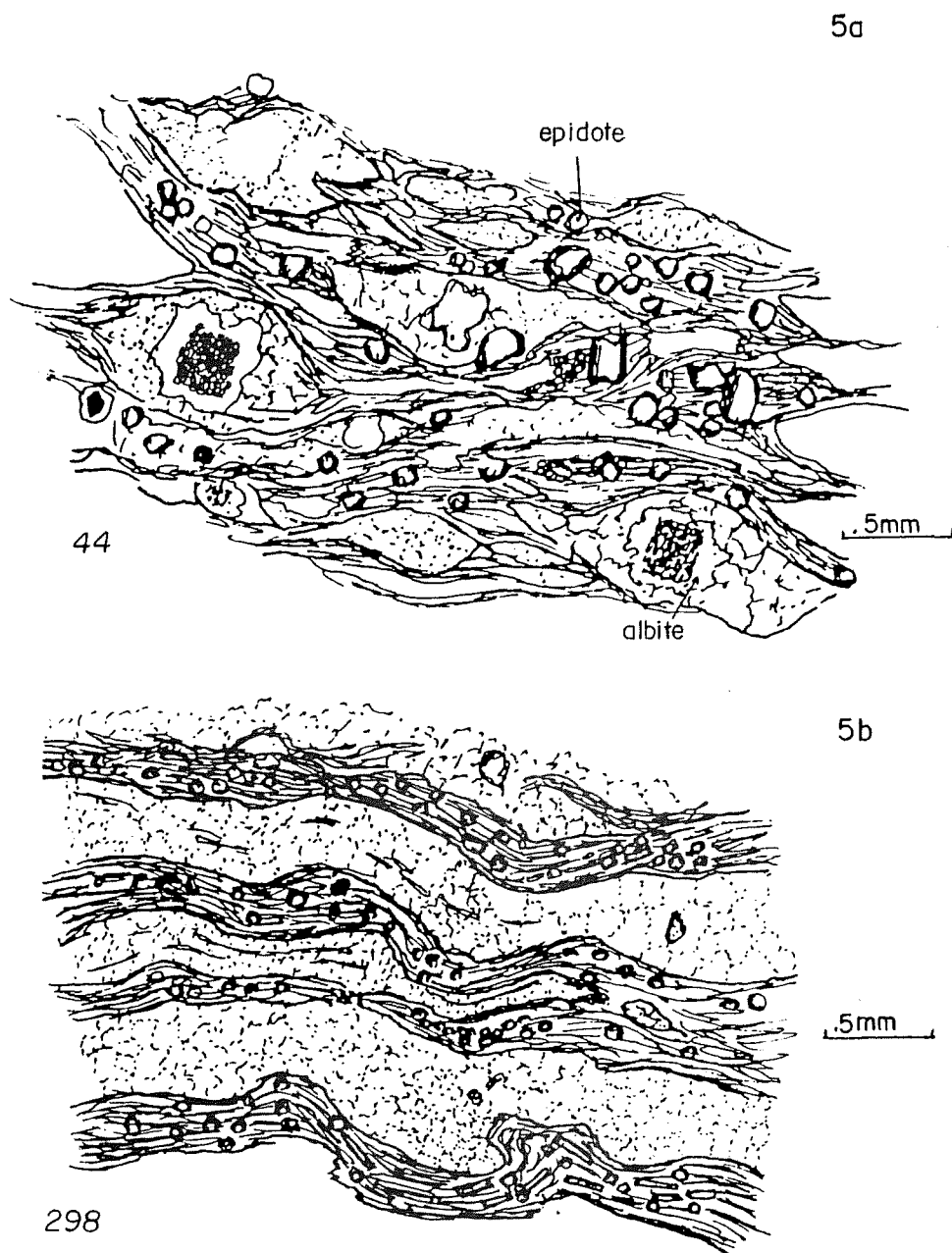


Figure 5a. Poorly developed mineral segregation in sample 44 associated with the second-phase deformation. The figure shows relict quartz and albite phenocrysts. Albite phenocrysts are riddled with pumpellyite. 5b. Sample 298 from southwestern Chatham Island has a better developed compositional layering parallel to second-phase foliation. Relict quartz and albite phenocrysts although present are smaller and less abundant than in sample 44.

mica and chlorite layers from quartz and albite layers is not well developed.

Sample 170 is the most poorly recrystallized sample analyzed. This sample contains a metamorphic foliation defined by oriented white mica and chlorite grains. Unlike the other samples, this rock contains many small relict hornblendes which all have actinolite rims.

Sample 206 is a fine-grained quartz-albite schist with a metamorphic foliation defined by oriented white mica and chlorite which wraps around partially to totally recrystallized quartz and albite grains.

Sample 298 is a quartz-albite schist collected from the Teraki Formation near the southwestern end of Chatham Island. Sample 298 has well developed compositional layers defined by parallel aligned, interlocked, white mica and minor chlorite which also contain epidote, pumpellyite, quartz, albite, relict zircon, brown and dusty appearing apatite, and sphene which surrounds relict ilmenite. These layers are separated by quartz- and albite-rich layers. Sample 298 has far fewer larger-grain-size crystals of relict quartz and albite phenocrysts that are typical of the quartz-albite schists from the Kaingaroa Volcanics described above. The quartz- and albite-rich layers are probably severely granulated, flattened, and recrystallized remains of original phenocrysts with a very few relict larger grains. A larger proportion of the pumpellyite in sample 298 is in the form of euhedral and subhedral prismatic crystals as opposed to the anhedral and pleochroic variety. As in other samples described, the cores of albites contain pumpellyite. There are minor folds in the second-phase foliation about third phase axial planes at right angles to the 2nd-phase foliation. Although no evidence for major recrystallization of mica or chlorite during third-phase folding is observed, the quartz and albite-rich layers have anhedral quartz and albite with sutured articulation suggesting recrystallization of these minerals. Figure 5b illustrates the nature of the layering in sample 298.

Black Argillaceous Schist

Black argillaceous schist sample 350 has a very well developed 2nd-phase compositional layering defined by wide, quartz- and albite-rich layers separated by thinner white mica, chlorite, epidote, sphene, pyrite, carbonaceous matter, relict zircon, and apatite layers. This rock has a pronounced third-phase solution cleavage which has sphene, carbonaceous material, and minor epidote aggregated in trains within the cleavage planes. In parts of the rock which are heavily deformed by the third phase deformation, white mica is aligned parallel within the cleavage planes.

Greenschists

Sample 383A was collected near Cape Pattison from a greenschist bed

within the Matarakau Graywacke. It is a fine-grained greenschist with actinolite, chlorite, quartz, epidote, and sphene, and may contain trace amounts of colorless, euhedral pumpellyite. This sample has a phase-one compositional layering which is well developed in places and is defined by parallel-aligned actinolite needles interlocked with chlorite separated by quartz- and albite-rich layers. In other parts of the rock the compositional layering is not so well developed and instead a second-phase crenulation cleavage cuts across an earlier 1st-phase foliation at a moderate angle. Parallel aligned and interlocked actinolites and chlorites are within the axial planar cleavage.

Sample 224B is an actinolite, epidote, pumpellyite, chlorite, quartz, albite greenschist which also contains sphene, calcite, trace amounts of anhedral and interstitial chalcopyrite which has hematite weathering rims, and relict ilmenite and apatite. This rock has a pronounced second-phase solution cleavage which is axial planar to 1-2 cm. wavelength, tight, second-phase folds. The solution cleavage is defined by segregations of insoluble minerals such as sphene, minor epidote, and parallel alignment of actinolite within the axial-planar solution-cleavage planes. The solution phenomena are similar to those described by Gray (1979) for pelitic, argillaceous, and mixed layer materials. The cleavage developed by: 1) Formation and tightening of minor (second-phase) folds. 2) Migration of quartz and albite out of the limbs of the folds into the hinge regions which results in some almost monomineralic layers composed of epidote. 3) Continued solution of more soluble material and accumulation of insoluble minerals such as sphene, and parallel alignment and possibly growth of elongate minerals (actinolite) within the third-phase solution-cleavage plane. The solution cleavage took advantage of limbs of second-phase folds that were parallel to the axial-planar cleavage and these are now solution surfaces which wrap around or anastomose around, remaining minor fold hinges and earlier foliation. In some places second-phase fold hinges abut the solution surfaces and are truncated.

In some areas of this section, where foliation is still present, the foliation is defined by the parallel alignment of fine-grained actinolite needles. The foliation is locally overprinted by small second-phase folds. The coarser-grained actinolite within the solution surfaces is evidence that actinolite grew during second-phase deformation. Noticeably absent are the relict quartz and albite phenocrysts present in greenschists 299 and 427.

Sample 299 is a micaceous greenschist which is characterized by a well developed compositional layering defined by interlocking white mica and chlorite plates separated by quartz- and albite-rich layers. The mineral segregation is well developed and larger relict albite or quartz phenocrysts are absent. The second-phase foliation is folded by tight 2-3 cm. wavelength folds which have a well developed axial planar solution cleavage. The cleavage is defined by aggregation of insoluble minerals such as sphene, minor epidote, and carbonaceous material along the cleavage planes. The development of the solution cleavage is probably

Second-phase foliation at a high angle to first-phase foliation.

Quartz and albite in the hinge region of a tight second-phase fold.

Early foliation deformed by second-phase deformation



Terminated second-phase fold limb.

Figure 6. Minor second-phase fold hinges in sample 224B truncated against solution surfaces defined by fine sphene aggregates (black). Also, the amount of mineral segregation along second-phase solution-cleavage surfaces, and the degree that the early foliation is transposed is significant.

similar to that described by Gray (1979).

Sample 427 is a pumpellyite, chlorite, quartz, albite greenschist with minor epidote, sphene, and apatite. The rock is dominated by compositional layering defined by pumpellyite and chlorite layers which also contain minor epidote and sphene separated by quartz- and albite-rich layers. Within the pumpellyite-chlorite layers pumpellyite occurs as euhedral and subhedral elongate prisms which are aligned parallel to each other and are intergrown with chlorite and minor sphene and epidote. The foliation wraps around anhedral individual grains of non-oriented pumpellyite which has abnormal bluish-tan birefringence and bluish-green pleochroism. The foliation also wraps around relict plagioclase grains which are now albite, and relict quartz phenocrysts. Relict grains have been partially recrystallized so that they are flattened in the plane of the foliation. Sample 427 has been deformed at a high angle by third-phase folding. The second-phase compositional layering is folded into closely spaced open folds and in some areas of the thin section tighter folds. Pumpellyite growth occurred parallel to phase-three fold axes. The pumpellyite is the euhedral colorless variety and in Figure 7 is shown as prismatic end sections of the euhedral elongate prisms.

Sample 429 is a massive epidote-rich, chlorite-albite-quartz-calcite-sphene greenschist which does not contain actinolite or pumpellyite. The rock is more massive due to the larger amount of epidote than the other samples. Sample 429 only has a weakly developed second-phase foliation defined by parallel-aligned interlocking chlorite which wraps around large relict plagioclase, quartz, and epidote. Epidote, which occurs as 1-2 mm. crystals, may be thoroughly recrystallized relict minerals, possibly plagioclase. These epidotes are disaggregated and deformed. Smaller subhedral and anhedral epidotes are also present. Thin discontinuous trains of sphene and epidote are aligned along a very weakly developed third-phase cleavage. Also small tight folds associated with the third-phase deformation are present but no major recrystallization has occurred. Noticeably absent is pumpellyite.

Garnet-bearing Schist

Sample 210B is a fine-grained garnet-bearing epidote, chlorite, white mica, calcite, albite, quartz, sphene schist. This rock is characterized by compositional layering which is cut by second-phase cleavage. In some areas compositional layering is folded into small tight second-phase folds. Second-phase cleavage cuts compositional layering and calcite has formed along cleavage surfaces. Garnet occurs in sample 210 in both chlorite-white mica-epidote layers and in quartz-albite-calcite layers.

Relations Between Tectonic Fabrics and Metamorphic Recrystallization

Mineral lineations and metamorphic foliation that developed during

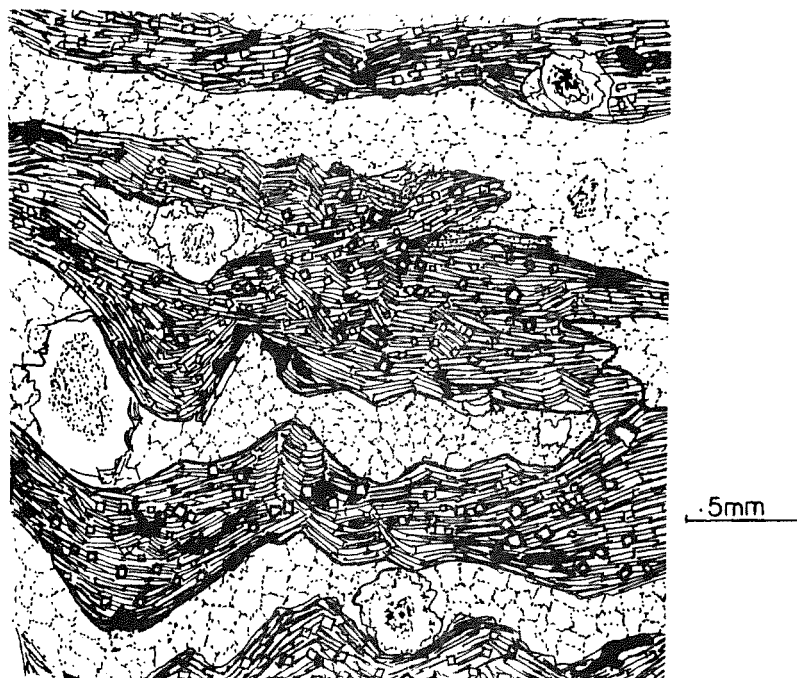


Figure 7. Sample 427 has a well developed second phase foliation defined by parallel aligned pumpellyite prisms and interlocked chlorite. Also shown are relict albite phenocrysts riddled with pumpellyite. Open to locally tight third phase folds deform second phase compositional layering.

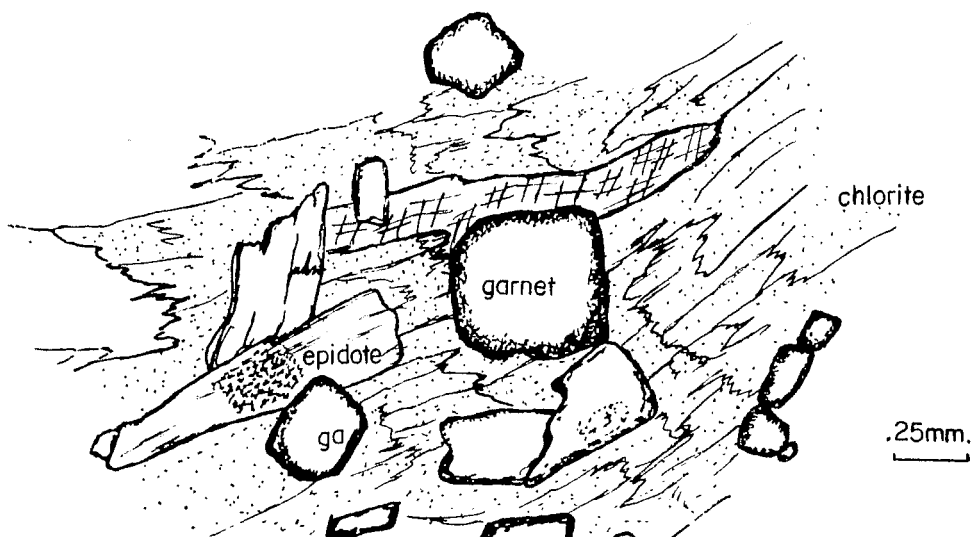


Figure 8. Garnet bearing schist. Also shown are epidote, chlorite, and calcite.

the first phase of folding can be found in samples from the Matarakau Graywacke, and locally in samples from the Kaingaroa Volcanics or the Teraki Formation. The nature of the metamorphism associated with first-phase folding is uncertain.

The second phase of folding, associated with large recumbent folds, was the dominant deformation on Chatham Island. The mineral lineations, minor folds, and metamorphic foliations seen in most schists from the Teraki Formation and the Kaingaroa Volcanics formed in this phase. In poorly bedded samples, and in the less deformed samples from the northeast portion of Chatham Island, foliation is defined by sheared, mechanically crushed, and recrystallized relict volcanic quartz and albite phenocrysts wrapped by interlocked white mica and chlorite plates. In well bedded samples and in samples from the southwest portion of Chatham Island metamorphic foliation is sub-parallel to or at a small to moderate angle to bedding. Pervasive recrystallization, mineral growth, and the formation of the present pumpellyite-actinolite facies mineral assemblages occurred during the second phase of deformation.

The effects of the third phase of folding can be seen only in schists from the Teraki Formation from the southwest portion of Chatham Island. In this phase there was development of crenulations and axial planar cleavages at a high angle to bedding and earlier foliations. Locally, mineral solution occurred in these cleavage planes. Pervasive recrystallization of micas or other silicate minerals does not seem to have occurred.

WHOLE ROCK GEOCHEMISTRY

Analytical Methods

Whole rock analyses were completed at the University of Massachusetts, Amherst, X-ray fluorescence analysis facility. Major elements were done on fused glass discs and irradiated using a chromium target X-ray tube. The fused discs were made by fusing rock samples with lithium tetraborate after the method of Norrish and Chapple (1967); and Norrish and Hutton (1969). Trace elements were analyzed using a pressed powder technique and a gold target X-ray tube. Corrections were made for background, and element interferences.

Introduction

X-ray fluorescence analyses were done on four quartz-albite schists, one black argillaceous schist, two greenschists, and one micaceous greenschist. These were done to explore indications from hand specimen descriptions, modal analyses, and petrographic interpretations (Adams and Robinson, 1977) that the metamorphic rocks were a compositionally similar series of pyroclastic, water-laid, volcanogenic sediments of dacitic and rhyolitic composition interbedded with a chemically more heterogeneous series of mafic volcanogenic sediments. Besides chemical characterization, this study was directed toward

understanding the relationship between bulk chemistry, modal abundance, and composition of metamorphic minerals. Processes which may have altered original volcanic compositions are also discussed.

Major Element Data

Table 3 lists whole rock, oxidized, anhydrous, major element analyses and trace element analyses of Chatham Island metamorphosed volcanogenic sediments. Total iron was measured as Fe_2O_3 . Table 3

shows norm calculations based on the assumption that 90% of the total iron is FeO and 10% is Fe_2O_3 .

In quartz-albite schists SiO_2 varies from 66.04 wt.% to 71.54 wt.%. The black argillaceous schist is more siliceous and contains 74.27 wt.% SiO_2 . In the greenschists SiO_2 varies from 43.60 wt.% to

50.50 wt.%. Samples 170, 206, 139, 298, 350, and 299 are peraluminous with $\text{Al}_2\text{O}_3 > (\text{Na}_2\text{O} + \text{K}_2\text{O} + \text{CaO})$. Greenschist samples 383A and 429 are olivine- and diopside-normative, whereas the quartz-albite schist samples, the black argillaceous schist sample, and micaceous greenschist sample 299 are quartz- and corundum-normative. Figure 9 shows that in quartz-albite schists the major oxides TiO_2 , Al_2O_3 , Fe_2O_3 , MnO , MgO ,

CaO , K_2O , and P_2O_5 all have negative correlation with SiO_2 , while Na_2O

is somewhat more anomalous. Black argillaceous schist sample 350 relates to the trend of the quartz-albite schists, but has significantly less CaO and more K_2O with respect to SiO_2 .

Greenschists have a much more heterogenous major element chemistry than quartz-albite schists. The micaceous greenschist sample is significantly different from the other two greenschists due to higher Al_2O_3 and especially K_2O , and lower FeO , MgO , and CaO .

The chemical distinction between the quartz-albite schists and the greenschists is easily made by comparing the lower SiO_2 and higher CaO , FeO , MgO , MnO , and TiO_2 of greenschists with the high values of SiO_2 ,

and lower values of CaO , FeO , MgO , MnO , TiO_2 of the quartz-albite schists.

Trace Element Data

Trace element data are plotted in Figure 10 as a function of wt.% SiO_2 . Averaged trace element abundances of rhyolites and dacites from the Tertiary to Recent of the South Pacific from Barker (1979) are plotted with Chatham Island quartz-albite schist data for comparison.

Greenschist trace element data varies significantly between the analyzed samples. As expected, Nb and Ce behave similarly whereas Zr is

Table 3. Whole rock major and trace element analyses of Chatham Island metamorphosed volcanogenic sediments. CIPW norm calculation based on the assumption 90% of the total iron measured is FeO.

	quartz-albite schists				argillaceous schist	greenschists		
Number	<u>139</u>	<u>170</u>	<u>206</u>	<u>298</u>	<u>350</u>	<u>383A</u>	<u>299</u>	<u>429</u>
SiO ₂	69.88	66.04	68.07	71.54	74.27	47.15	50.53	43.68
TiO ₂	0.70	0.87	0.69	0.52	0.51	3.57	2.17	2.46
Al ₂ O ₃	14.60	15.81	15.22	14.41	14.25	14.54	20.88	16.60
Fe ₂ O ₃	4.42	5.29	4.48	3.68	3.79	16.68	11.02	18.53
MnO	0.06	0.08	0.07	0.06	0.04	0.22	0.19	1.00
MgO	1.74	2.19	1.79	1.55	1.17	7.06	3.67	6.79
CaO	2.79	3.76	2.98	2.55	0.49	6.09	3.84	9.36
Na ₂ O	3.61	3.41	4.04	4.00	3.58	3.92	2.85	1.52
K ₂ O	1.77	2.74	1.99	1.71	2.50	0.91	3.80	0.08
P ₂ O ₅	0.14	0.17	0.14	0.14	0.12	0.25	0.47	0.39
Total	<u>99.71</u>	<u>100.36</u>	<u>99.47</u>	<u>100.16</u>	<u>100.72</u>	<u>100.39</u>	<u>99.42</u>	<u>100.41</u>
Sr	428	525	518	272	67	166	187	1281
Ba	432	781	527	528	612	13	624	0
Nb	11	12	11	9	10	36	77	2
Zr	219	221	215	171	178	311	196	112
Zn	90	86	70	56	72	170	170	196
Ni	21	22	24	19	16	28	100	82
Cr	71	59	65	41	46	10	294	145
V	78	91	79	70	91	409	246	537
Ce	56	52	54	49	29	51	86	13
quartz	31.72	22.12	25.97	32.49	39.49		1.47	
albite	30.63	29.11	34.35	33.93	30.38	33.68	24.37	13.12
anorthite	12.98	17.64	13.92	11.79	1.66	19.69	16.15	38.86
orthoclase	10.52	16.25	11.82	10.10	14.83	5.44	22.69	0.47
hypersthene	9.54	11.65	9.78	8.30	7.49	0.64	21.59	22.54
diopside						7.73		4.78
olivine						23.29		12.24
corundum	2.01	0.79	1.33	1.69	5.06		6.28	
magnetite	0.64	0.77	0.65	0.54	0.55	2.45	1.61	2.73
ilmenite	1.33	1.65	1.32	0.99	0.97	6.88	4.16	4.75
apatite	<u>0.33</u>	<u>0.40</u>	<u>0.33</u>	<u>0.33</u>	<u>0.28</u>	<u>0.59</u>	<u>1.11</u>	<u>0.95</u>
Total	<u>99.70</u>	<u>100.38</u>	<u>99.47</u>	<u>100.16</u>	<u>100.71</u>	<u>100.39</u>	<u>99.43</u>	<u>100.44</u>

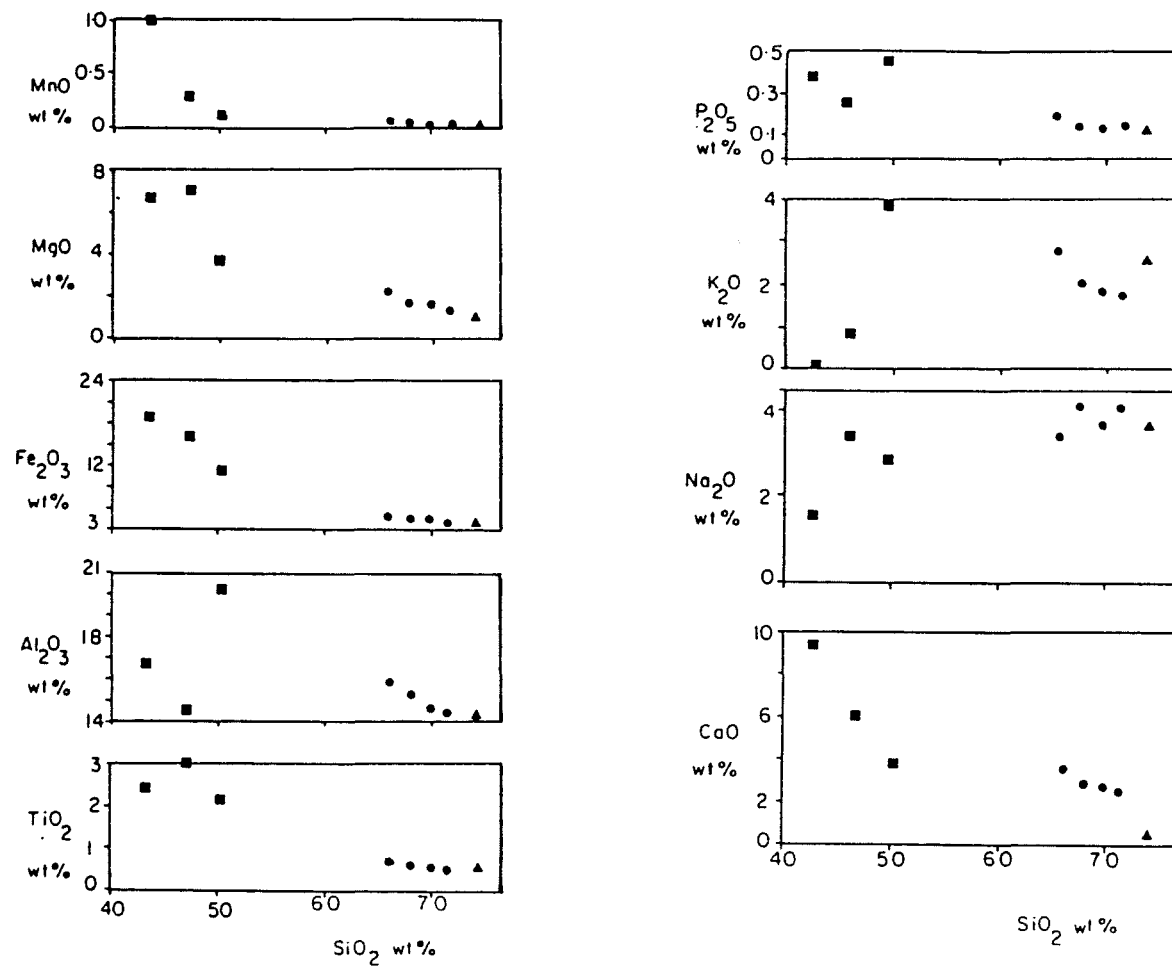


Figure 9. Variation of major elements with respect to SiO_2 for Chatham Island schist samples.

more unusual. V correlates with Fe content of the samples. Cr and Ni are similar to each other but are independent of SiO_2 . Both Ba and Sr have a large range of values.

Discussion

Major element and trace element data indicate that quartz-albite schists are compositionally similar to each other and that the existing variation is systematic and similar to rhyolite or rhyodacite fractionation trends. Figure 11, a plot of the immobile elements Zr/TiO_2 vs. Ce (Winchester and Floyd, 1976) indicates that these samples fall within the dacite field. The variation of Na_2O with SiO_2 can be used (Schumacher, 1983) to test if the quartz-albite schists are derived from weathered volcanogenic material, or from sediments that contained preferential accumulations of plagioclase feldspar. Figure 12 shows the variation of Na_2O vs. SiO_2 for dacites and rhyolites from the Tonga-Kermadec trench enclosed by the dashed line (Ewart et al., 1979) and other averaged Tertiary-Recent South Pacific volcanics are shown by open circles (Barker et al., 1979). Chatham Island quartz-albite schists are very similar in composition to these other volcanics. If preferential weathering of a source area has occurred to provide sediments for these schists, the bulk composition should be shifted toward silica as shown by the double arrows on Figure 12. If a schist were derived from sediments composed of accumulated plagioclase feldspar, the bulk composition would be shifted toward the plagioclase feldspar, as shown by the single arrows on Figure 12. Argillaceous schist sample 350 is slightly shifted toward SiO_2 , indicating it is derived from a weathered source. The overall chemistry of the quartz-albite schists indicates that they are derived from volcanogenic sediments which have a similar source and that they are not significantly contaminated by terrigenous material, although evaluation of this with a small number of samples is very difficult (Leake, 1964).

The greenschists, on the other hand, are more heterogeneous and have compositions that are related to original volcanic compositions but vary due to alteration processes. Variation in major elements and trace elements is a function of the original chemical variation of the volcanic source, subsequent effects of crystal and ash sorting during eruption, transportation, or deposition, mixing of nonvolcanogenic continental detritus, high or low temperature alteration, weathering, and metamorphism (Sparks et al., 1973; Scott, 1977; Humphris and Thompson, 1978; Stephens et al., 1978; Winchester and Floyd, 1978; Schumacher, 1983). The small number of samples makes interpretation problematic but some generalizations can be made. The greenschists, plotted on Figure 11 for Zr/TiO_2 vs. Ce, all fall within the basalt

field, although 429 has a much lower Zr/TiO_2 ratio. The high MnO, and Sr, along with the low SiO_2 of sample 429 suggest it is altered.

Humphris and Thompson (1978) have shown experimentally that both MnO and Sr can be leached from basalts during hydrothermal alteration and

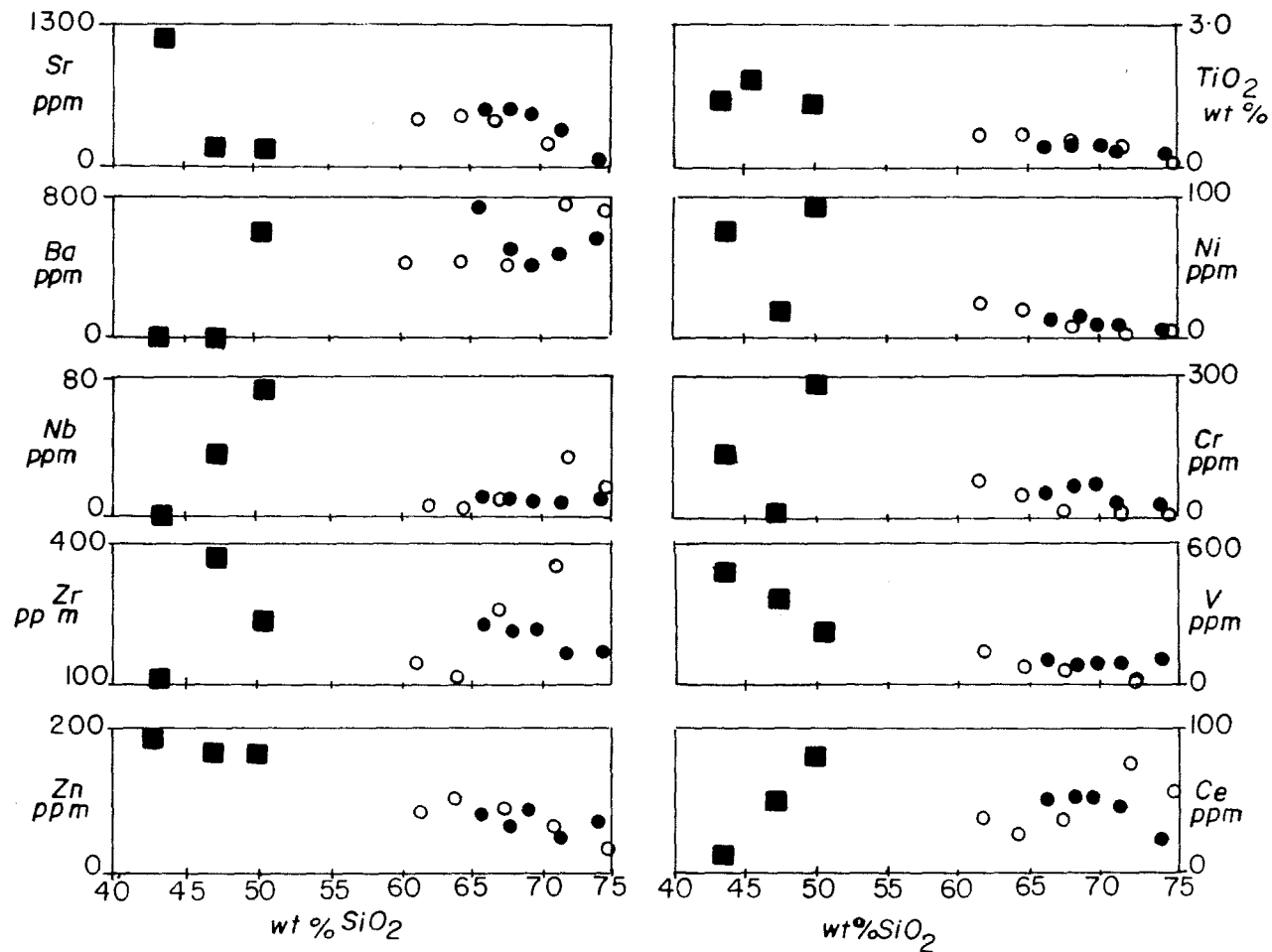


Figure 10. Variation of trace elements with respect to SiO₂. Open circles are averaged Tertiary-Recent dacite and rhyodacite analyses (Barker, 1979) from the Southwest Pacific.

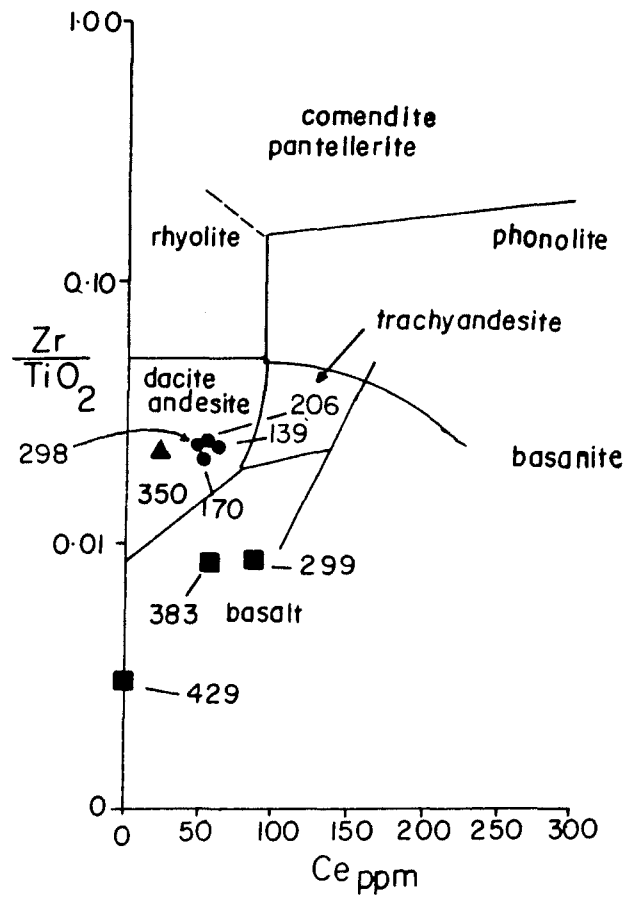


Figure 11. Schist samples plotted in terms of the relatively immobile elements Zr/TiO_2 vs. Ce . From Floyd and Winchester (1978).

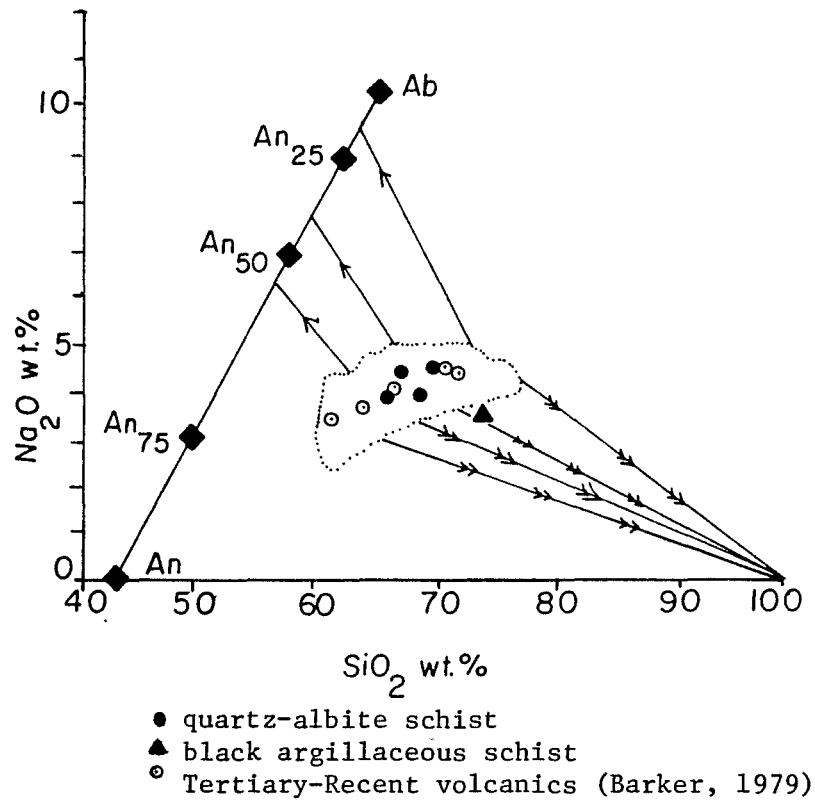


Figure 12. Chatham Island quartz-albite schists and black argillaceous schist plotted in terms of Na_2O vs. SiO_2 (Schumacher, 1983). The dotted area encloses rhyolites and dacites from the Tonga-Kermadec island arc (Ewart et al., 1973) and the open circles are averaged data compiled from Tertiary-Recent volcanics from the southwest Pacific (Barker, 1979). If there were preferential concentration of quartz, the analyses would be outside the enclosed area towards the lower right (double arrows). If there had been preferential sorting and accumulation of plagioclase, the analyses would plot to the left (single arrows). Sample 350 shows evidence of quartz concentration.

redeposited in epidote-rich altered basalts.

The high Al_2O_3 , K_2O , Cr, and Ni and the low MgO, and CaO abundances of sample 299 suggest that this sample is from a weathered protolith. Sample 299 also contains unusually high Nb values and this can be seen in Figure 13 (Nb vs. Zr) which suggests some loss of Zr or gain of Nb. A loss of Zr is not reflected in the Zr/TiO_2 ratios suggesting: 1) the sample contains an unusual abundance of Nb possibly incorporated in rutile and now accumulated in sphene; 2) contamination of the sample during preparation, possibly from the shatter box (Rhodes personal communication, 1984).

Sample 383A does not have any unusual characteristics and the high Zr, and TiO_2 abundances and the low Zr/Nb ratio are similar to ocean island basalts as shown in Figure 13 (Pearce and Norry, 1979; Floyd and Winchester, 1978).

Figure 14 shows whole rock data on an ACF diagram assuming 10% of the iron is Fe_2O_3 . Also plotted are the metamorphic minerals associated with quartz-albite schists or greenschists.

MINERALOGY

Analytical Procedure

Microprobe samples were prepared by polishing and carbon coating standard, uncovered, petrographic thin sections which are ground to .03 mm. All microprobe analyses were done with the three-spectrometer wavelength-dispersive ETEC automated electron microprobe at the University of Massachusetts, Amherst. The microprobe operating conditions were 15Kev accelerating potential, .02 amp beam current, 1×10^{-5} torr chamber vacuum, 2 μm to 7 μm visual fluorescence beam diameter, 15 second peak and background counting time. Intensity data were corrected for detector dead time and background counting rate. X-ray intensity data were converted to weight% oxide with the correction procedure of Bence and Albee (1968) using the empirical α factors of Albee and Ray (1970). Standards used are all well characterized mineral or glass standards.

White Mica

Thin section description. White mica in quartz-albite schists occurs as individual subhedral crystals with mosaic articulation, but more characteristically as plates interlocked with other white mica and/or chlorite. The parallel alignment of white mica defines the foliation. White mica has parallel extinction on perfect 001 cleavage, birefringence = .041, and $2V \sim 30^\circ$. Most white mica has a pale green color indicating that some Fe^{3+} substitutes for Al (Finch et al., 1982). The average grain size is 0.01 mm x 0.06 mm.

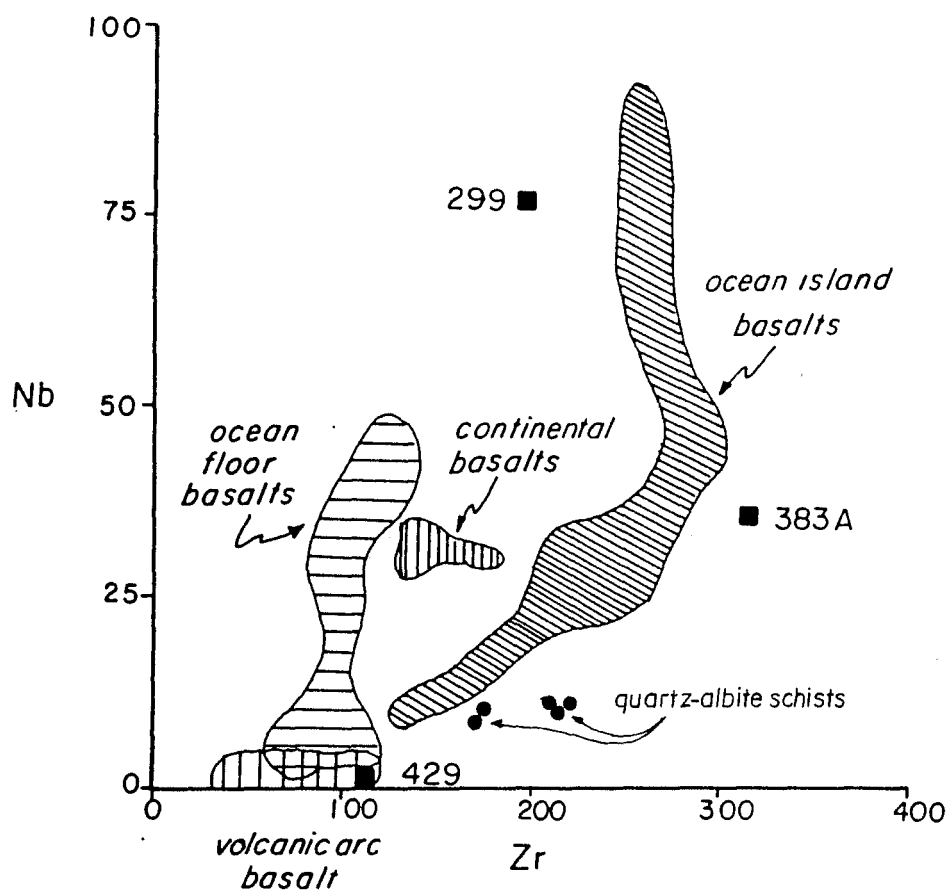


Figure 13. Greenschists and quartz-albite schists plotted in terms of Nb vs. Zr. Discriminant fields are from Pearce and Cann (1973).

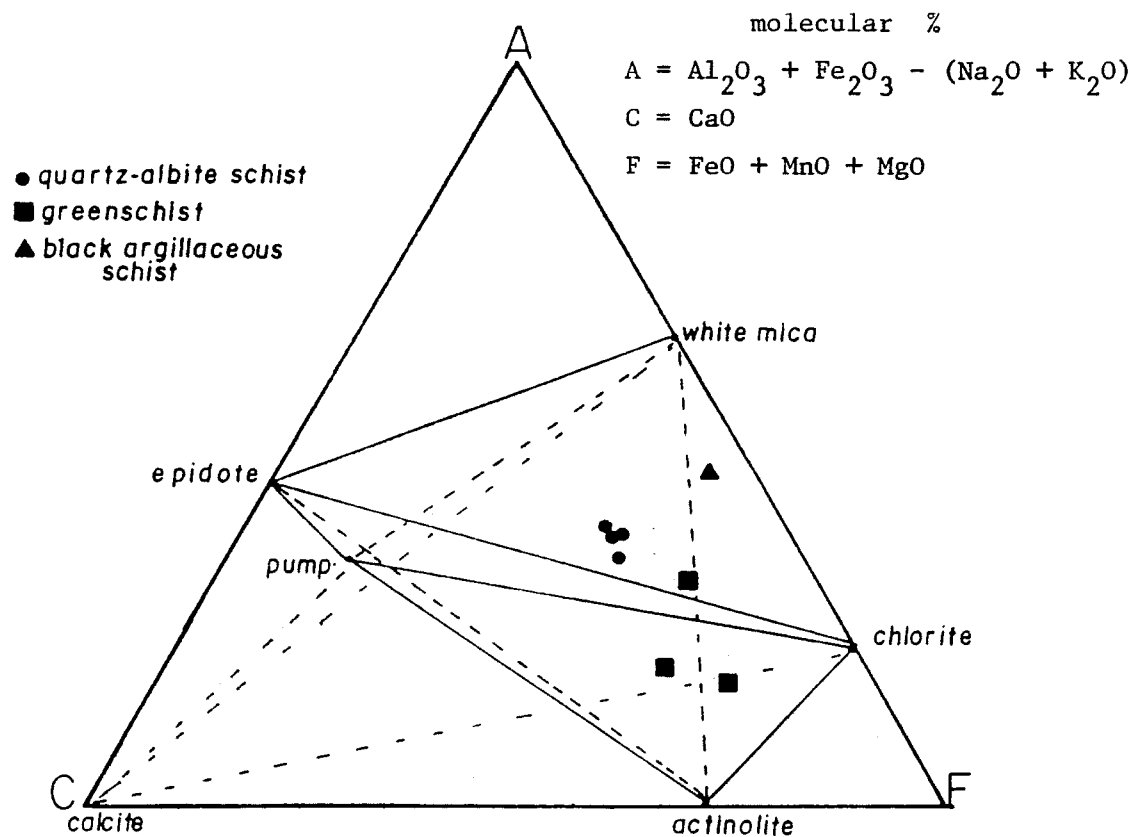


Figure 14. whole rock analyses plotted in terms of molecular percent on an ACF diagram. Also shown are metamorphic minerals in Chatham Island schists.

Chemistry. White mica analyses are listed in Table 4. The first column of structural formulae is recalculated from the microprobe analyses and is based on a normalization of eleven oxygens per half unit cell. This type of normalization assumes all iron is ferrous and the formulae deviate from ideal stoichiometry. The second column shows structural formulae recalculated from electron microprobe analyses normalized on the basis of an ideal dioctahedral mica which has 11 oxygens and six cations in octahedral and tetrahedral positions per half unit cell. In this second normalization Fe^{3+} is produced as needed from Fe^{2+} for charge balance (Robinson et al., 1982). Figure 15 indicates how much Fe^{3+} is added from Fe^{2+} for each analyzed mica. In Figure 15 these normalized microprobe analyses are compared with wet chemical data on white micas from the Shirataki district, Japan, and the Franciscan terrane, California (Ernst et al., 1970).

In volcanic sediments metamorphosed in the pumpellyite-actinolite facies, white mica can differ significantly from ideal dioctahedral muscovite by various substitution mechanisms. These substitutions lead to the following ideal structural formulae:

$\text{KAl}_2\text{Si}_3\text{AlO}_{10}(\text{OH})_2$	muscovite
$\text{KFe}^{3+}\text{AlSi}_3\text{AlO}_{10}(\text{OH})_2$	ferrimuscovite
$\text{K}(\text{Mg}, \text{Fe}^{2+})_{0.5}\text{Al}_{1.5}\text{Si}_{3.5}\text{Al}_{0.5}\text{O}_{10}(\text{OH})_2$	phengite
$\text{K}(\text{Mg}, \text{Fe}^{2+})\text{AlSi}_4\text{O}_{10}(\text{OH})_2$	leucophyllite
$\text{K}(\text{Mg}, \text{Fe}^{2+})\text{Fe}^{3+}\text{Si}_4\text{O}_{10}(\text{OH})_2$	celadonite

Three important exchange reactions are: 1) $\text{Fe}^{2+} + \text{Mg} + \text{Mn (VI)} + \text{Si(IV)} = \text{Al(VI)} + \text{Al(IV)}$. 2) $\text{Fe}^{3+} = \text{Al}$. 3) $\text{Fe}^{2+} = \text{Mg}$. The first reaction relates ideal dioctahedral muscovite $\text{KAl}_2\text{AlSi}_3\text{O}_{10}(\text{OH})_2$ to the ideal

dioctahedral end member leucophyllite, and to the intermediate compositional member phengite $\text{K}(\text{Fe}^{2+}, \text{Mg})_{0.5}\text{Al}_{1.5}\text{Si}_{3.5}\text{Al}_{0.5}\text{O}_{10}(\text{OH})_2$.

The second reaction relates muscovite to ferrimuscovite, leucophyllite to celadonite, and phengite to ferriphengite

$\text{K}(\text{Fe}^{2+}, \text{Mg})_{0.5}\text{Fe}^{3+}_{1.5}\text{Si}_{3.5}\text{Al}_{0.5}\text{O}_{10}(\text{OH})_2$. The third exchange reaction

relates magnesian phengite and ferroan phengite (Kannehara and Banno, 1960; Guidotti and Sassi, 1978; Velde, 1965; Tracy, 1978; Guidotti, 1984). Another potentially important simple substitution relates muscovite to paragonite by the $\text{K}=\text{Na}$ exchange. Other substitutions are possible in white micas (e.g. $\text{Ca Al} = \text{KSi}$, $\text{Cr}^{3+} = \text{Al}$, $\text{B}^{+}(\text{IV})=\text{Al}$, $\text{F}=\text{OH}$), but these either cannot be evaluated with electron microprobe data or are of minor importance in Chatham Island micas.

The extent and controls on the extent of solid solution between these end members is better understood in higher grade rocks

Table 4. Electron microprobe analyses of white micas. Structural formulae for each analysis on the basis of 1) 11 oxygens and 2) A total of 6 cations in the octahedral and tetrahedral sites and 11 oxygens.

Number	44-1	44-2	44-3	44-4	44-5	77-1	77-2	77-3	77-4	77-5
SiO ₂	51.39	51.35	51.30	51.25	51.57	51.19	51.13	51.39	52.61	52.32
TiO ₂	0.03	0.04	0.06	0.05	0.05	0.05	0.03	0.06	0.01	0.08
Al ₂ O ₃	25.81	25.22	25.36	25.22	24.17	25.96	25.50	25.07	26.12	24.86
FeO	3.74	3.83	3.29	3.37	4.12	3.58	3.56	3.65	3.45	4.06
MnO	0.00	0.02	0.06	0.00	0.03	0.03	0.02	0.02	0.04	0.00
MgO	3.16	3.31	3.24	3.26	3.35	3.00	3.06	3.65	2.94	3.40
CaO	0.00	0.00	0.00	0.00	0.00	0.03	0.00	0.03	0.02	0.04
Na ₂ O	0.11	0.11	0.08	0.05	0.09	0.04	0.11	0.03	0.14	0.04
K ₂ O	10.05	10.52	10.18	9.99	9.95	10.76	10.53	10.70	10.30	9.87
Total	94.29	94.40	93.57	93.19	93.33	94.64	93.94	94.60	95.63	94.67
Si	3.472	3.439	3.480	3.453	3.489	3.464	3.502	3.474	3.527	3.494
Al	.528	.561	.520	.547	.511	.536	.498	.526	.473	.506
	4.000	4.000	4.000	4.000	4.000	4.000	4.000	4.000	4.000	4.000
Al	1.527	1.475	1.494	1.451	1.522	1.482	1.521	1.477	1.475	1.424
Ti	.001	.001	.002	.002	.003	.003	.002	.002	.002	.002
Fe ³⁺		.195	.212		.145		.173		.189	
Mg	.318	.315	.334	.331	.328	.326	.332	.329	.341	.338
Fe ²⁺	.211	.014	.217	.003	.187	.041	.193	.018	.236	.045
Mn			.001	.001	.003	.003		.002	.002	
	2.057	2.000	2.047	2.000	2.043	2.000	2.048	1.999	2.056	2.000
Ca							.002	.002		
Na	.014	.014	.014	.014	.009	.009	.007	.007	.012	.012
K	.883	.875	.871	.864	.909	.902	.871	.864	.891	.877
	.897	.889	.885	.878	.918	.911	.878	.871	.903	.889
	.935	.930	.928	.923	.934	.929	.934	.929	.893	.889
XMg*	.601	.957	.605	.887	.633	.881	.632	.948	.589	.878
$\frac{K}{K+Na+Ca}$.984	.984	.984	.984	.990	.990	.993	.993	.987	.987

*XMg = Mg/(Mg+Fe²⁺+Mn)

Table 4. continued.

Number	<u>77-6</u>		<u>77-7</u>		<u>77-8</u>		<u>298-1</u>		<u>298-2</u>		<u>298-3</u>		<u>298-4</u>		<u>298-5</u>		<u>298-6</u>		<u>298-7</u>	
SiO ₂	52.87		52.26		51.59		49.89		52.45		51.90		51.38		51.45		51.37		51.57	
TiO ₂	0.06		0.05		0.07		0.00		0.02		0.01		0.00		0.02		0.00		0.05	
Al ₂ O ₃	25.35		25.32		24.18		25.57		25.56		25.84		25.58		25.57		25.64		25.23	
FeO	3.55		3.78		3.73		3.50		3.56		4.06		3.48		3.33		3.28		3.84	
MnO	0.04		0.04		0.01		0.03		0.00		0.00		0.02		0.02		0.00		0.02	
MgO	3.26		3.01		3.73		3.50		3.28		3.14		3.33		3.33		3.15		3.19	
CaO	0.00		0.05		0.04		0.06		0.04		0.04		0.02		0.03		0.01		0.02	
Na ₂ O	0.08		0.12		0.03		0.06		0.11		0.12		0.07		0.11		0.13		0.11	
K ₂ O	<u>10.22</u>		<u>10.05</u>		<u>10.64</u>		<u>10.86</u>		<u>10.43</u>		<u>10.01</u>		<u>10.74</u>		<u>10.77</u>		<u>10.11</u>		<u>10.03</u>	
Total	95.43		94.68		94.02		93.41		95.45		95.12		94.62		94.63		93.69		94.06	
Si	3.522	3.494	3.517	3.496	3.530	3.519	3.424	3.401	3.489	3.433	3.505	3.441	3.471	3.447	3.483	3.453	3.486	3.462	3.495	3.464
Al	<u>.478</u>	<u>.506</u>	<u>.483</u>	<u>.504</u>	<u>.470</u>	<u>.481</u>	<u>.576</u>	<u>.599</u>	<u>.511</u>	<u>.567</u>	<u>.495</u>	<u>.559</u>	<u>.529</u>	<u>.553</u>	<u>.517</u>	<u>.547</u>	<u>.514</u>	<u>.538</u>	<u>.505</u>	<u>.536</u>
	4.000	4.000	4.000	4.000	4.000	4.000	4.000	4.000	4.000	4.000	4.000	4.000	4.000	4.000	4.000	4.000	4.000	4.000	4.000	4.000
Al	1.521	1.477	1.517	1.484	1.480	1.463	1.494	1.457	1.572	1.483	1.563	1.462	1.508	1.471	1.524	1.475	1.537	1.499	1.510	1.461
Ti	.003	.003	.002	.002	.001	.001			.001	.001	.002	.002			.001	.001			.002	.002
Fe ³⁺		.154		.134		.080		.189		.175		.189		.151		.133		.149		.198
Mg	.324	.321	.302	.300	.324	.323	.344	.342	.326	.321	.316	.310	.335	.333	.338	.335	.319	.317	.323	.320
Fe ²⁺	.198	.042	.213	.078	.213	.132	.201	.010	.198	.020	.230	.037	.197	.044	.188	.053	.186	.036	.218	.018
Mn	.002	.002	.002	.002	.001	.001	.002	.002					.001	.001	.001	.002				
	<u>2.048</u>	<u>1.999</u>	<u>2.036</u>	<u>2.000</u>	<u>2.019</u>	<u>2.000</u>	<u>2.041</u>	<u>2.000</u>	<u>2.097</u>	<u>2.000</u>	<u>2.111</u>	<u>2.000</u>	<u>2.041</u>	<u>2.000</u>	<u>2.052</u>	<u>1.999</u>	<u>2.042</u>	<u>2.001</u>	<u>2.053</u>	<u>1.999</u>
Ca			.004	.004	.003	.003			.003	.003	.003	.003	.001	.001	.002	.002	.001	.001	.001	.001
Na	.010	.010	.016	.016	.004	.004	.007	.007	.014	.014	.016	.016	.009	.009	.014	.014	.017	.017	.014	.014
K	<u>.869</u>	<u>.862</u>	<u>.863</u>	<u>.858</u>	<u>.929</u>	<u>.926</u>	<u>.952</u>	<u>.945</u>	<u>.903</u>	<u>.889</u>	<u>.890</u>	<u>.874</u>	<u>.936</u>	<u>.930</u>	<u>.931</u>	<u>.923</u>	<u>.875</u>	<u>.869</u>	<u>.867</u>	<u>.859</u>
	.879	.872	.883	.878	.936	.933	.959	.952	.917	.903	.909	.893	.946	.940	.947	.939	.893	.887	.882	.874
XMg*	.618	.884	.584	.789	.602	.708	.629	.971	.622	.941	.579	.972	.628	.881	.641	.850	.632	.911	.598	.943
$\frac{K}{K+Na+Ca}$.989	.989	.977	.977	.989	.989	.993	.993	.981	.981	.979	.979	.989	.989	.983	.983	.979	.979	.983	.983

*XMg = Mg / (Mg+Fe²⁺+Mn)

Table 4. continued.

Number	<u>298-8</u>		<u>298-9</u>		<u>298-10</u>		<u>298-11</u>		<u>298-12</u>		<u>298-13</u>		<u>206-1</u>		<u>206-2</u>	
SiO ₂	51.73		51.45		52.65		52.11		51.85		53.23		51.42		50.50	
TiO ₂	0.00		0.05		0.02		0.06		0.08		0.01		0.08		0.08	
Al ₂ O ₃	25.67		25.77		25.63		25.21		24.54		24.52		24.15		24.71	
FeO	3.12		3.38		3.53		3.37		3.61		3.66		3.36		3.41	
MnO	0.03		0.00		0.00		0.00		0.00		0.03		0.00		0.00	
MgO	3.18		2.73		2.81		2.80		2.89		3.42		3.40		3.45	
CaO	0.02		0.05		0.05		0.03		0.05		0.03		0.00		0.00	
Na ₂ O	0.10		0.11		0.17		0.11		0.13		0.11		0.09		0.13	
K ₂ O	<u>11.00</u>		<u>9.68</u>		<u>9.57</u>		<u>9.72</u>		<u>10.44</u>		<u>10.52</u>		<u>10.19</u>		<u>10.93</u>	
Total	94.85		93.22		94.43		93.41		93.59		95.55		92.60		93.21	
Si	3.483	3.477	3.501	3.480	3.529	3.509	3.534	3.519	3.534	3.528	3.582	3.535	3.534	3.517	3.473	3.459
Al	<u>.517</u>	<u>.527</u>	<u>.499</u>	<u>.520</u>	<u>.471</u>	<u>.491</u>	<u>.466</u>	<u>.481</u>	<u>.466</u>	<u>.472</u>	<u>.418</u>	<u>.465</u>	<u>.466</u>	<u>.483</u>	<u>.527</u>	<u>.541</u>
	4.000	4.000	4.000	4.000	4.000	4.000	4.000	4.000	4.000	4.000	4.000	4.000	4.000	4.000	4.000	4.000
Al	1.520	1.504	1.568	1.535	1.554	1.523	1.549	1.525	1.506	1.497	1.528	1.455	1.492	1.466	1.477	1.455
Ti			.002	.002	.001	.001	.003	.003	.004	.004			.004	.004	.004	.004
Fe ³⁺		.040		.130		.123		.099		.036		.100		.097		.108
Mg	.319	.318	.277	.275	.281	.279	.283	.282	.294	.293	.343	.338	.339	.337	.347	.345
Fe ²⁺	.176	.136	.189	.058	.198	.074	.191	.091	.206	.170	.206	.103	.193	.095	.196	.087
Mn	.002	.002									.003	.003				
	<u>2.017</u>	<u>2.000</u>	<u>2.036</u>	<u>2.000</u>	<u>2.034</u>	<u>2.000</u>	<u>2.026</u>	<u>2.000</u>	<u>2.010</u>	<u>2.000</u>	<u>2.080</u>	<u>1.999</u>	<u>2.028</u>	<u>1.999</u>	<u>2.024</u>	<u>1.999</u>
Ca	.001	.001	.004	.004	.004	.004	.002	.002	.004	.004	.002	.002				
Na	.013	.013	.015	.015	.022	.022	.014	.014	.017	.017	.014	.014	.012	.012	.017	.017
K	<u>.945</u>	<u>.942</u>	<u>.833</u>	<u>.828</u>	<u>.818</u>	<u>.813</u>	<u>.841</u>	<u>.837</u>	<u>.908</u>	<u>.906</u>	<u>.904</u>	<u>.892</u>	<u>.894</u>	<u>.890</u>	<u>.960</u>	<u>.956</u>
	.959	.956	.852	.847	.844	.839	.857	.853	.929	.927	.920	.908	.906	.902	.977	.973
XMg*	.697	.739	.594	.826	.586	.790	.597	.756	.588	.632	.621	.761	.637	.780	.639	.799
$\frac{K}{K+Na+Ca}$.985	.985	.977	.977	.969	.969	.981	.981	.977	.977	.983	.983	.987	.987	.982	.982

*XMg = Mg / (Mg+Fe²⁺+Mn)

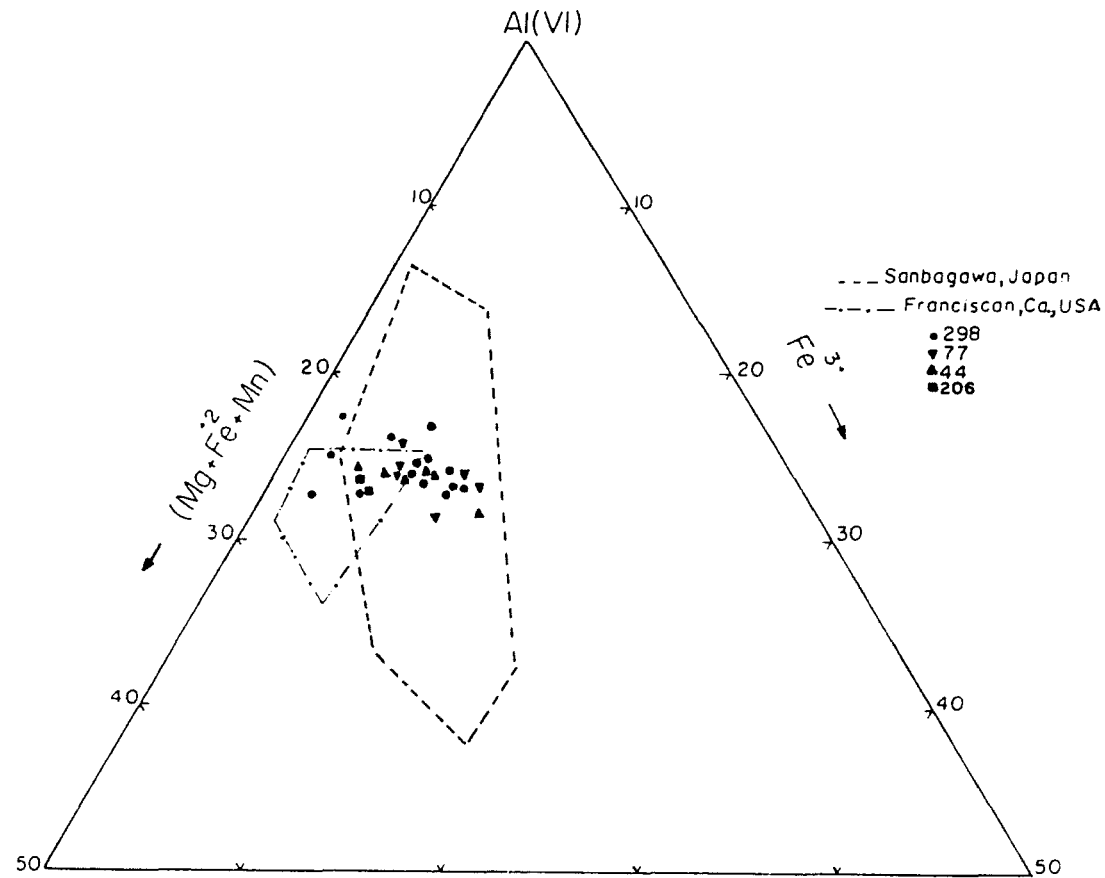


Figure 15. Chatham Island phengite analyses plotted in terms of $Al(VI) - Mg+Fe^{2+}+Mn - Fe^{3+}$. Chatham Island normalized phengite analyses are similar to wet chemical analyses of phengites from Sanbagawa, Japan, and the Franciscan terrane California (Ernst et al., 1970).

for the rocks of pelitic composition (Evans and Guidotti, 1966; Cheney and Guidotti, 1975; Tracy, 1978; Guidotti, 1969, 1970, 1973, 1974, 1978; Guidotti and Sassi, 1977; Thompson, 1974; Thompson and Algor, 1977).

At lower grades, below the garnet isograd, and in high-pressure, low-temperature regimes white mica chemistry is less well understood (Mather, 1970; Ernst, 1963; 1970; Velde, 1965; Butler, 1967; Korikovski, 1973). Immiscibility at low temperature and pressure between celadonite and muscovite may exist but the solvus relations are not well established (Wise and Eugster, 1962; Velde, 1965). Radoslovich (1963) indicated that white mica with Si greater than 3.5 will not have a muscovite structure, but the data of Velde, 1965; and Massonne (1981 in Guidotti, 1984) shows that solution of muscovite towards leucophyllite is almost complete at $P > 10$ kbar. Most chemically analyzed metamorphic white micas do have less than 3.5 atoms of Si per 11 oxygens, but limited data from high pressure terranes show Si greater than 3.5 (Chopin, 1979; Ernst et al., 1970).

There are two other important coupled exchanges, one which relates muscovite to pyrophyllite by the exchange $K (A \text{ site}) + Al (IV) = (A \text{ site}) + Si (IV)$, and the exchange $2Al (VI) = 3(Mg+Mn+Fe) (VI)$ which relates muscovite to biotite. The pyrophyllite substitution maintains dioctahedral stoichiometry whereas the biotite substitution adds a trioctahedral component. Radoslovich, (1963) indicated that the trioctahedral substitution in dioctahedral micas should be small and experiments by Green (1981) at pressures up to 10 kbar showed only very minor trioctahedral substitution. Crystal chemical arguments suggest that no trioctahedral component exists in dioctahedral micas at normal geologic conditions (Bailey, 1984; Geise, 1984). For this reason the discussion and diagrams used here will be based on the normalized perfectly dioctahedral white mica formulae.

White mica analyses from Chatham Island are plotted on a series of diagrams to examine the extent of these exchange reactions. Analyses can be plotted in terms of the endmembers muscovite, leucophyllite-celadonite, and pyrophyllite. Plotting coordinates are determined by setting the equation $X=Y+Z$ where;

X = charge increasing substitution (K or Na in A site).

Z = charge decreasing substitution (tetrahedral Al for tetrahedral Si).

Y = charge decreasing substitution (M^{2+} for Al^{3+} or Fe^{3+} in octahedral site).

The apices of the triangular diagram in Figure 16 are determined by the values $Z=0, Y=0$; $Z=1, Y=0$; and $Z=0, Y=1$. White mica analyses from Chatham samples 44, 77, 298, and 206 are plotted. It's clear from Figure 16 that the white mica in Chatham Island schists is phengite with a significant but minor pyrophyllite component.

Effects of Fe^{3+} substitution on the phengite composition are shown on a triangular reciprocal prism similar to that used for pyroxenes by Robinson (1980). Any square face of the reciprocal prism can be examined by collapsing the components of the opposite side onto the face

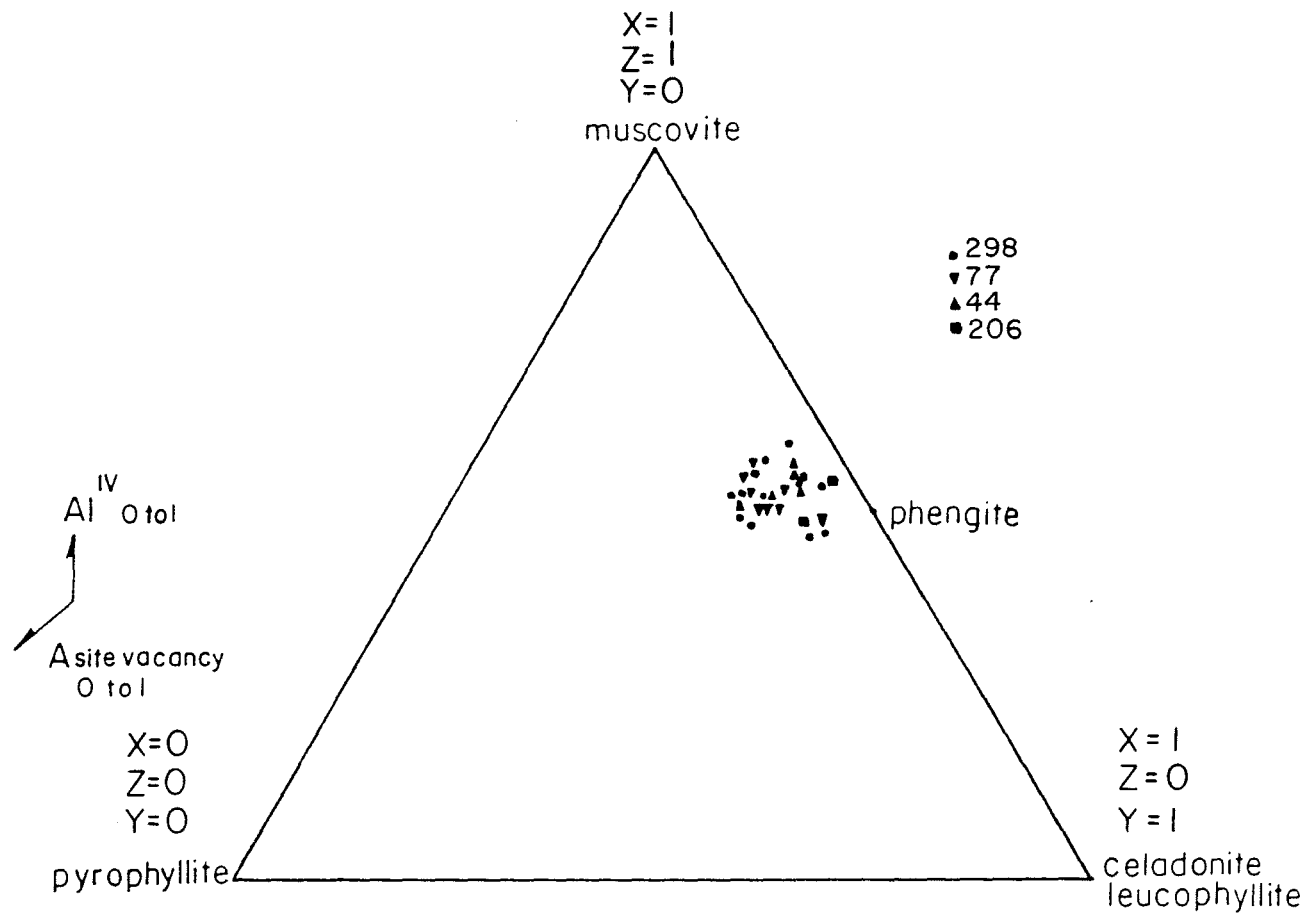


Figure 16. Normalized phengite analyses plotted on a ternary diagram in terms of muscovite component, phengite component, and pyrophyllite component.

examined by collapsing the components of the opposite side onto the face examined, as shown in Figure 17, in which the Fe^{3+} substitution is plotted as a function of $\text{Fe}^{3+}/(\text{Fe}^{3+} + \text{Al})$. The paragonite component in white mica can be examined by considering a portion of the composition space $\text{Al}_2\text{O}_3 - \text{KAlO}_2 - \text{NaAlO}_2 - \text{FeO} + \text{MgO} + \text{MnO}$ as shown in Figure 18. The paragonite substitution is very small and varies from 0.7% to 2.2%.

The compositions of white micas were determined to see if mica chemistry is a function of different bulk rock composition, and to see if there are any composition changes that might reflect a change in metamorphic grade between the southwestern and northeastern exposures of metamorphic rocks on Chatham Island. The analyses (Table 4) and the figures given above indicate that there are only small differences and considerable overlap in white mica chemistry between the samples. Figure 19a illustrates the variation of $\text{Mg}/(\text{Mg} + \text{Fe}^{2+} + \text{Mn})$ vs. total Al. Considerable overlap between analyzed samples is apparent, and the unusually large variation in the Mg ratio suggests the potential for error in the normalization of microprobe data. Figure 19b illustrates the variation of $\text{Fe}^{3+}/(\text{Fe}^{3+} + \text{Al})$ vs. total Al; a small variation in Fe^{3+} is illustrated but with large overlap between samples and no obvious differences that could be related to bulk composition.

One other important point is that the normalized white mica formulae may only indicate a maximum crystal chemically reasonable amount of Fe^{3+} and the "true" amount may be in between this maximum and the all-ferrous white mica analyses. Many wet chemical analyses show phengite with $\text{Mg} > \text{Fe}^{2+}$ by a ratio of 2:1 (Guidotti, 1984) while Chatham Island schist white micas have a higher ratio in nearly all analyses (Figure 19a).

Chlorite

Thin section description. Chlorite is not abundant in quartz-albite schists of Chatham Island. It has abnormal blue interference colors, and positive elongation. Typical grain size ranges from 0.05 - 0.075 mm, up to 0.075 - 0.1 mm. Chlorite typically occurs as small one - and two-grain aggregates within the compositional layering defined by white mica, epidote, pumpellyite, quartz, and albite.

In greenschist samples 224B and 427, and in the garnet-bearing sample 210B there is a greater abundance of chlorite than in quartz-albite schists. In greenschists, chlorites have abnormal brown interference color, negative sign of elongation, and a very faint green color. In samples 224B and 210B some chlorites have abnormal blue, or violet interference colors (see Table 6). The grains with the violet interference colors do not have a preferred sign of elongation.

Chemistry. Chlorite microprobe analyses are listed in Table 5. The microprobe analyses are recalculated on the basis of 14 oxygens per formula unit. The chlorites are listed in order of decreasing $\text{Mg}/(\text{Mg} + \text{Fe}^{2+} + \text{Mn})$.

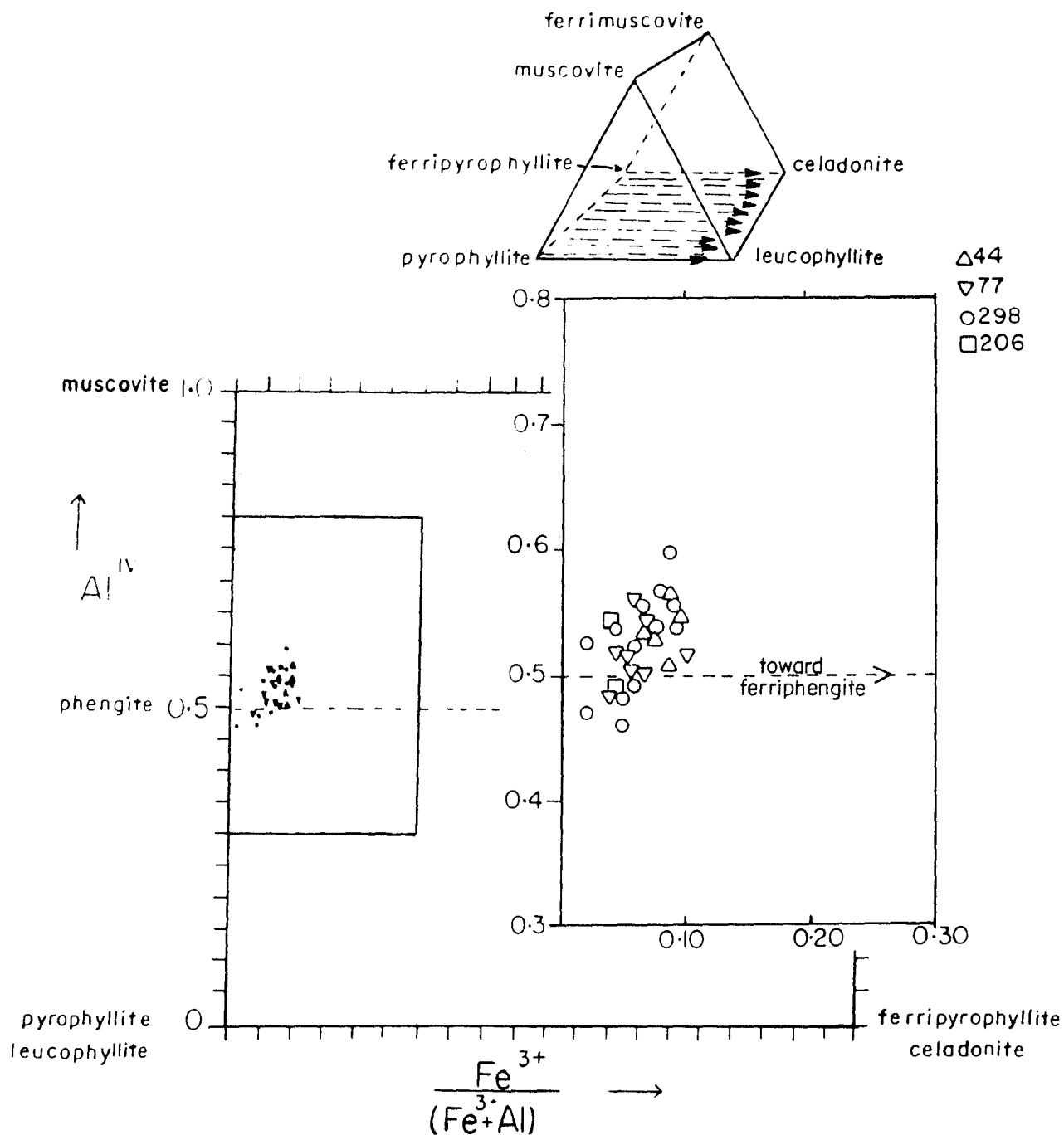


Figure 17. Reciprocal prism indicating the ferriphengite component in Chatham Island white micas.

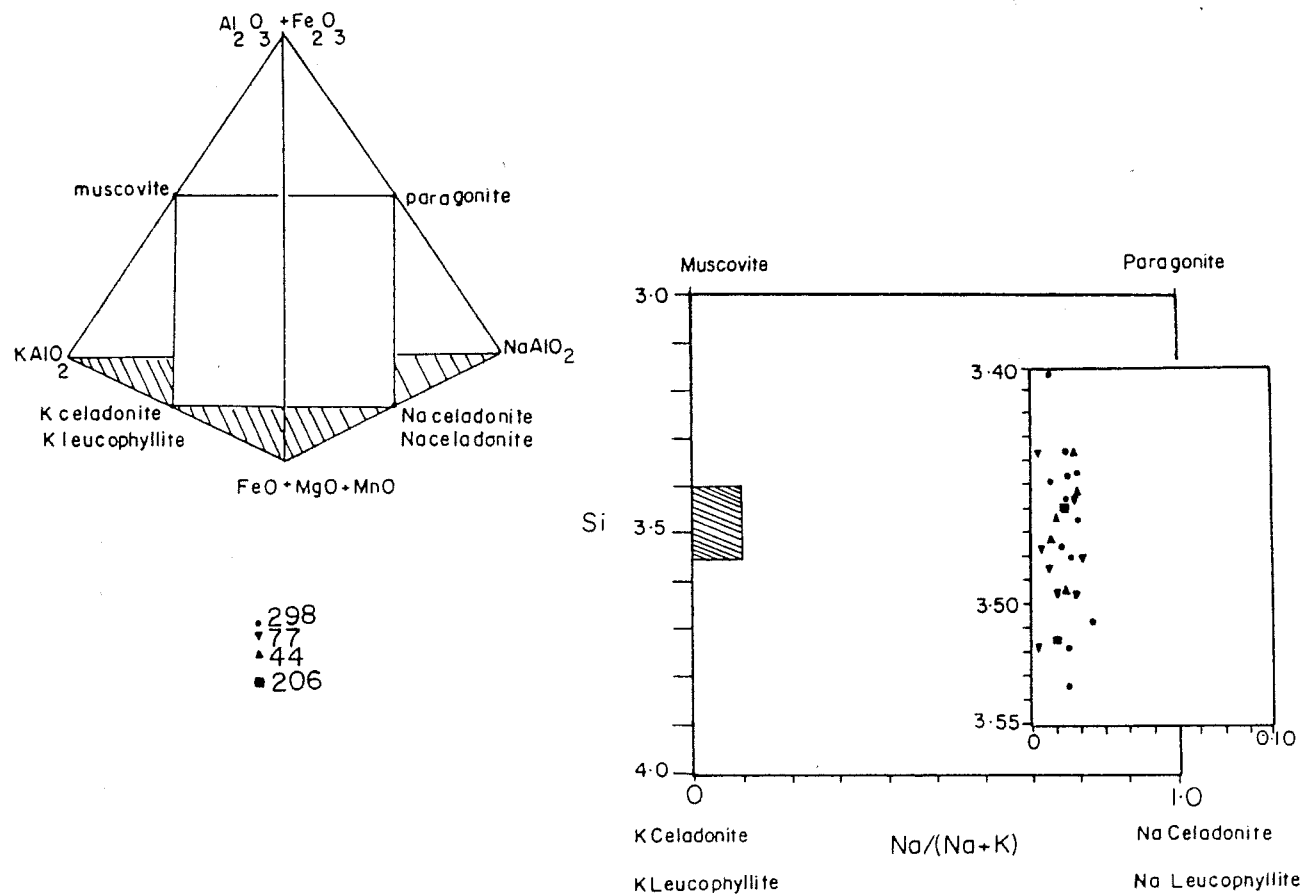


Figure 18. Phengite analyses plotted to illustrate the low paragonite component.

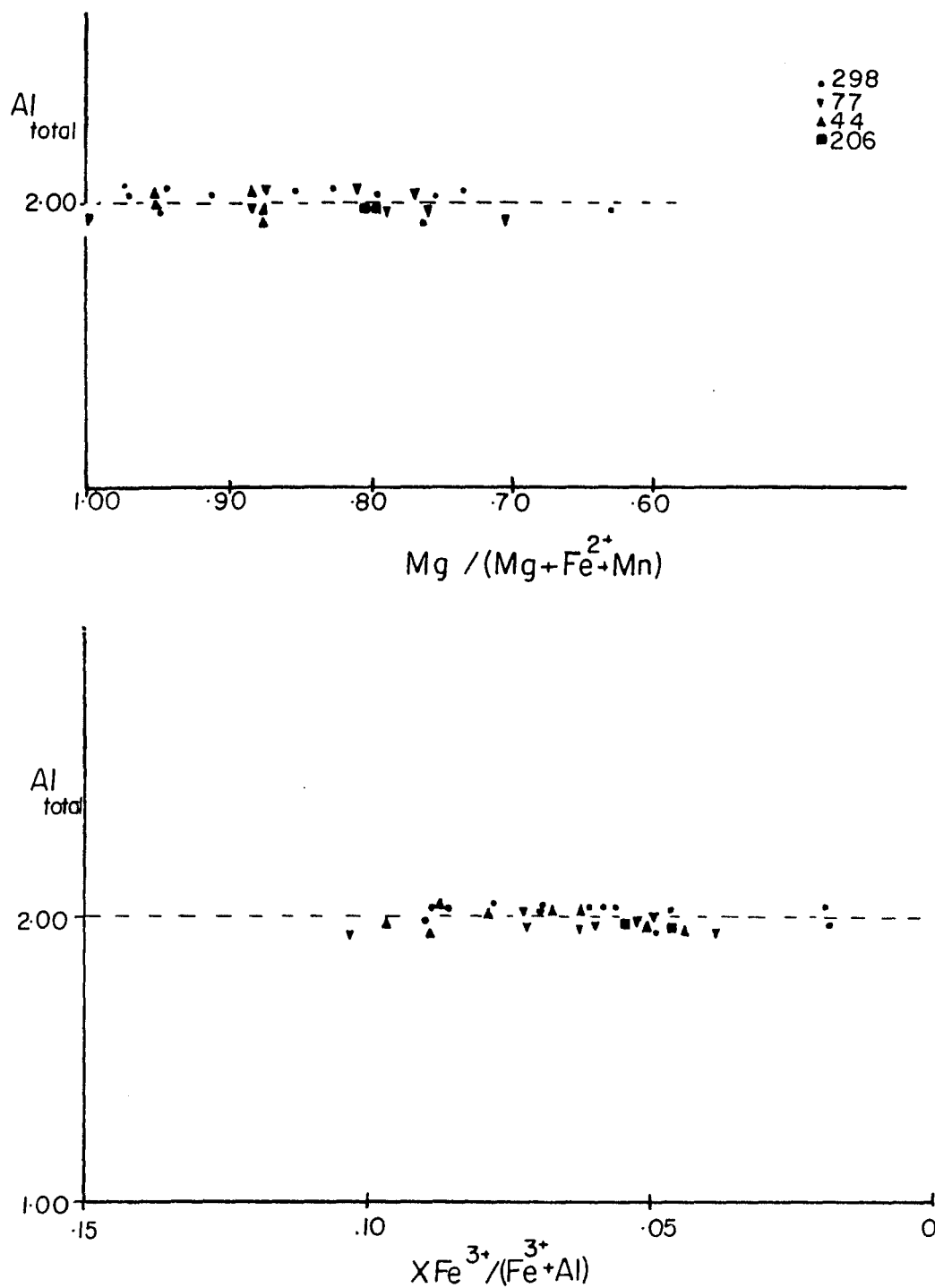


Figure 19. $\text{Mg}/(\text{Mg} + \text{Fe}^{2+} + \text{Mn})$ vs. Al_{total} and $\text{Fe}^{3+}/(\text{Fe}^{3+} + \text{Al})$ vs. Al_{total} for normalized white mica microprobe analyses.

Table 5. Electron microprobe analyses of chlorite. Structural formulae based on 14 oxygens.

Number	<u>427-1</u>	<u>427-2</u>	<u>427-3</u>	<u>427-4</u>	<u>427-5</u>	<u>427-6</u>	<u>224-1</u>	<u>224-2</u>	<u>224-3</u>	<u>224-4</u>	<u>224-5</u>	<u>224-6</u>	<u>224-7</u>	<u>224-8</u>	<u>224-9</u>	<u>224-10</u>
									rim	core						rim
SiO ₂	27.84	26.86	26.45	27.31	27.32	27.69	26.38	26.52	26.84	27.14	26.55	26.82	26.83	26.43	26.27	25.77
TiO ₂	0.03	0.00	0.09	0.04	0.00	0.00	0.05	0.05	0.04	0.02	0.05	0.04	0.04	0.01	0.04	0.08
Al ₂ O ₃	20.49	20.31	18.98	20.05	19.59	20.12	19.87	19.78	19.15	19.74	20.27	19.59	19.78	19.72	19.71	19.93
FeO	25.48	25.91	25.44	26.00	25.90	26.32	26.59	26.62	26.77	26.67	26.71	26.78	26.74	26.87	26.87	27.35
MnO	0.29	0.37	0.33	0.35	0.36	0.39	0.41	0.49	0.42	0.40	0.44	0.47	0.45	0.42	0.43	0.42
MgO	16.59	16.47	16.10	16.19	16.13	15.98	14.77	14.83	14.70	14.51	14.36	14.07	13.97	13.97	14.83	13.62
CaO	0.00	0.00	0.00	0.00	0.00	0.00	0.06	0.06	0.06	0.05	0.07	0.07	0.07	0.03	0.05	0.04
Na ₂ O	0.08	0.00	0.01	0.05	0.09	0.00	0.00	0.00	0.00	0.08	0.00	0.01	0.00	0.00	0.01	0.00
K ₂ O	<u>0.00</u>	<u>0.00</u>	<u>0.00</u>	<u>0.00</u>	<u>0.00</u>	<u>0.00</u>	<u>0.01</u>	<u>0.02</u>	<u>0.02</u>	<u>0.01</u>	<u>0.01</u>	<u>0.02</u>	<u>0.01</u>	<u>0.02</u>	<u>0.01</u>	<u>0.00</u>
Total	90.80	89.92	87.40	89.99	89.40	90.50	88.14	88.37	88.00	88.62	88.46	88.87	87.89	87.47	88.22	87.21
Structural formulae based on 14 oxygens																
Si	2.817	2.761	2.801	2.803	2.824	2.826	2.790	2.794	2.840	2.844	2.790	2.816	2.838	2.815	2.801	2.765
Al	<u>1.183</u>	<u>1.239</u>	<u>1.199</u>	<u>1.197</u>	<u>1.176</u>	<u>1.174</u>	<u>1.210</u>	<u>1.206</u>	<u>1.160</u>	<u>1.156</u>	<u>1.210</u>	<u>1.184</u>	<u>1.162</u>	<u>1.185</u>	<u>1.199</u>	<u>1.235</u>
	4.000	4.000	4.000	4.000	4.000	4.000	4.000	4.000	4.000	4.000	4.000	4.000	4.000	4.000	4.000	4.000
Al	1.262	1.223	1.171	1.230	1.213	1.247	1.219	1.250	1.228	1.282	1.301	1.250	1.304	1.291	1.277	1.286
Ti	.003		.007	.003			.004	.004	.003	.001	.004	.003	.003	.001	.003	.007
Mg	2.504	2.525	2.543	2.479	2.487	2.433	2.329	2.321	2.319	2.266	2.250	2.236	2.203	2.218	2.245	2.178
Fe	2.157	2.228	2.254	2.233	2.241	2.247	2.353	2.352	2.369	2.337	2.348	2.396	2.366	2.394	2.519	2.454
Mn	.025	.032	.030	.031	.032	.034	.036	.044	.038	.035	.039	.042	.040	.038	.039	.038
Ca					.001		.007	.007	.007	.006	.008	.008	.007	.003	.006	.004
Na	.009		.003	.010	.019					.016		.002			.002	
K							.001	.003	.003	.001	.001	.003	.001	.003	.001	
	<u>5.960</u>	<u>6.008</u>	<u>6.008</u>	<u>5.986</u>	<u>5.993</u>	<u>5.961</u>	<u>5.949</u>	<u>5.981</u>	<u>5.967</u>	<u>5.944</u>	<u>5.951</u>	<u>5.940</u>	<u>5.924</u>	<u>5.948</u>	<u>6.092</u>	<u>5.967</u>
XMg*	.534	.528	.527	.523	.522	.516	.494	.492	.491	.488	.485	.478	.478	.477	.467	.466

*XMg = Mg/ (Mg+Fe+Mn)

Table 5. continued.

Number	<u>210-1</u>	<u>210-2</u>	<u>210-3</u>	<u>210-4</u>	<u>210-5</u>	<u>210-6</u>	<u>210-7</u>	<u>210-8</u>	<u>210-9</u>	<u>44-1</u>	<u>44-2</u>	<u>44-3</u>	<u>44-4</u>	<u>44-5</u>	<u>44-6</u>	<u>44-7</u>	<u>44-8</u>
SiO ₂	24.95	24.88	24.99	25.97	25.45	25.83	26.17	26.29	25.54	26.26	26.52	26.68	26.42	26.65	26.46	26.33	26.42
TiO ₂	0.00	0.00	0.00	0.00	0.02	0.00	0.04	0.00	0.01	0.01	0.01	0.00	0.01	0.04	0.03	0.01	0.00
Al ₂ O ₃	19.47	19.46	19.90	19.88	19.83	20.32	20.44	20.64	20.49	19.04	18.97	19.24	19.26	19.48	19.12	19.48	19.04
FeO	27.50	27.05	27.07	27.19	27.07	26.33	27.74	27.10	27.12	27.83	28.73	28.73	28.72	28.65	28.16	29.20	26.67
MnO	0.95	0.83	0.82	0.85	0.94	0.78	0.77	0.88	1.07	0.52	0.44	0.53	0.48	0.50	0.54	0.42	0.49
MgO	15.23	14.84	14.52	14.55	14.47	13.71	14.33	13.59	13.29	13.44	13.69	13.57	13.45	13.44	13.23	13.61	13.34
CaO	0.04	0.07	0.08	0.03	0.03	0.03	0.04	0.06	0.08	0.00	0.00	0.00	0.00	0.00	0.00	0.00	0.00
Na ₂ O	0.02	0.00	0.03	0.00	0.00	0.00	0.00	0.00	0.02	0.01	0.00	0.00	0.00	0.00	0.00	0.00	0.00
K ₂ O	<u>0.00</u>	<u>0.00</u>	<u>0.00</u>	<u>0.00</u>	<u>0.00</u>	<u>0.00</u>	<u>0.00</u>	<u>0.00</u>	<u>0.00</u>	<u>0.00</u>	<u>0.00</u>	<u>0.00</u>	<u>0.01</u>	<u>0.00</u>	<u>0.00</u>	<u>0.00</u>	<u>0.00</u>
Total	88.16	87.13	87.41	88.47	87.81	87.00	89.53	88.56	87.62	87.11	88.36	88.75	88.35	88.76	87.54	89.05	87.96
Structural formulae based on 14 oxygens																	
Si	2.669	2.686	2.686	2.747	2.718	2.766	2.739	2.772	2.733	2.829	2.826	2.828	2.815	2.822	2.839	2.789	2.828
Al	<u>1.331</u>	<u>1.314</u>	<u>1.314</u>	<u>1.253</u>	<u>1.282</u>	<u>1.234</u>	<u>1.261</u>	<u>1.228</u>	<u>1.267</u>	<u>1.171</u>	<u>1.174</u>	<u>1.172</u>	<u>1.185</u>	<u>1.178</u>	<u>1.161</u>	<u>1.211</u>	<u>1.172</u>
	4.000	4.000	4.000	4.000	4.000	4.000	4.000	4.000	4.000	4.000	4.000	4.000	4.000	4.000	4.000	4.000	4.000
Al	1.049	1.162	1.207	1.226	1.214	1.331	1.260	1.337	1.317	1.247	1.208	1.232	1.232	1.268	1.257	1.221	1.230
Ti					.002		.003		.001	.001	.001		.001	.003	.002	.001	
Mg	2.428	2.388	2.326	2.294	2.303	2.188	2.235	2.135	2.120	2.158	2.174	2.144	2.136	2.121	2.116	2.149	2.129
Fe	2.460	2.442	2.433	2.406	2.418	2.358	2.428	2.389	2.427	2.505	2.560	2.547	2.560	2.537	2.527	2.587	2.567
Mn	.086	.076	.076	.076	.085	.071	.068	.078	.097	.047	.040	.047	.043	.045	.049	.038	.044
Ca	.004	.008	.009	.003	.003	.003	.004	.007	.009								
Na	.004		.006					.004		.002							
K													.001				
	<u>6.031</u>	<u>6.076</u>	<u>6.056</u>	<u>6.005</u>	<u>6.025</u>	<u>5.951</u>	<u>5.998</u>	<u>5.946</u>	<u>5.975</u>	<u>5.962</u>	<u>5.983</u>	<u>5.970</u>	<u>5.973</u>	<u>5.974</u>	<u>5.951</u>	<u>5.996</u>	<u>5.970</u>
X _{Mg} [*]	.488	.487	.481	.480	.479	.474	.472	.464	.456	.458	.455	.452	.451	.451	.451	.450	.449
[*] X _{Mg} = Mg/(Mg+Fe+Mn)																	

Table 5. continued.

Number	<u>77-1</u>	<u>77-2</u>	<u>77-3</u>	<u>77-4</u>	<u>77-5</u>	<u>77-6</u>	<u>77-7</u>	<u>77-8</u>	<u>77-9</u>	<u>298-1</u>	<u>298-2</u>	<u>298-3</u>	<u>298-4</u>	<u>298-5</u>	<u>298-6</u>	<u>298-7</u>	<u>298-8</u>	<u>298-9</u>
SiO ₂	26.33	26.00	26.02	26.41	25.56	25.91	25.70	26.63	25.87	26.49	25.77	26.68	26.06	26.14	26.25	26.04	26.52	25.90
TiO ₂	0.05	0.00	0.00	0.04	0.04	0.09	0.00	0.00	0.00	0.03	0.05	0.04	0.03	0.04	0.03	0.07	0.01	0.04
Al ₂ O ₃	18.88	18.00	19.58	19.35	19.42	19.64	18.02	18.40	19.31	19.79	20.41	19.72	20.51	19.66	20.54	19.93	20.64	20.25
FeO	29.20	29.47	29.42	29.13	28.73	29.60	29.97	30.24	30.36	29.40	29.79	30.28	30.30	30.76	30.70	30.45	30.72	31.30
MnO	0.55	0.48	0.56	0.56	0.60	0.54	0.64	0.58	0.48	0.40	0.40	0.35	0.37	0.33	0.29	0.31	0.37	0.36
MgO	12.85	13.15	13.20	12.93	12.79	12.71	12.84	12.86	12.83	12.85	12.05	11.88	11.69	11.79	11.73	11.55	11.61	11.16
CaO	0.04	0.01	0.00	0.00	0.04	0.00	0.00	0.00	0.00	0.00	0.04	0.00	0.00	0.00	0.02	0.00	0.00	0.00
Na ₂ O	0.00	0.00	0.01	0.01	0.00	0.00	0.00	0.00	0.00	0.00	0.00	0.00	0.00	0.00	0.00	0.00	0.00	0.00
K ₂ O	<u>0.00</u>	<u>0.00</u>	<u>0.00</u>	<u>0.00</u>	<u>0.02</u>	<u>0.01</u>	<u>0.00</u>	<u>0.00</u>	<u>0.00</u>	<u>0.00</u>	<u>0.00</u>	<u>0.00</u>	<u>0.00</u>	<u>0.01</u>	<u>0.00</u>	<u>0.00</u>	<u>0.00</u>	<u>0.00</u>
Total	87.90	87.11	88.79	88.43	87.20	88.50	87.17	88.71	88.85	88.96	88.51	88.95	88.96	88.73	89.56	88.35	89.87	89.01
Structural formulae based on 14 oxygens																		
Si	2.831	2.833	2.772	2.818	2.771	2.773	2.811	2.850	2.769	2.808	2.755	2.838	2.774	2.801	2.778	2.795	2.795	2.772
Al	<u>1.169</u>	<u>1.167</u>	<u>1.228</u>	<u>1.182</u>	<u>1.229</u>	<u>1.227</u>	<u>1.189</u>	<u>1.150</u>	<u>1.231</u>	<u>1.192</u>	<u>1.245</u>	<u>1.162</u>	<u>1.226</u>	<u>1.199</u>	<u>1.222</u>	<u>1.205</u>	<u>1.205</u>	<u>1.228</u>
	4.000	4.000	4.000	4.000	4.000	4.000	4.000	4.000	4.000	4.000	4.000	4.000	4.000	4.000	4.000	4.000	4.000	4.000
Al	1.223	1.145	1.231	1.252	1.252	1.250	1.134	1.171	1.205	1.280	1.327	1.310	1.348	1.283	1.340	1.316	1.358	1.326
Ti	.004			.003	.003	.007				.002	.004	.003	.002	.003	.002	.006	.001	.003
Mg	2.144	2.136	2.096	2.057	2.066	2.027	2.093	2.052	2.047	2.030	1.920	1.884	1.855	1.883	1.850	1.848	1.824	1.780
Fe	2.625	2.685	2.621	2.599	2.604	2.649	2.741	2.707	2.718	2.606	2.663	2.694	2.698	2.756	2.717	2.733	2.707	2.801
Mn	.050	.044	.050	.051	.055	.049	.059	.053	.043	.036	.036	.031	.033	.030	.026	.028	.033	.033
Ca	.006	.002			.005						.003				.002			
Na			.002	.002														
K					.002	.001								.001				
	<u>6.052</u>	<u>6.012</u>	<u>6.000</u>	<u>5.964</u>	<u>5.987</u>	<u>5.983</u>	<u>6.027</u>	<u>5.983</u>	<u>6.013</u>	<u>5.954</u>	<u>5.953</u>	<u>5.922</u>	<u>5.936</u>	<u>5.956</u>	<u>5.937</u>	<u>5.931</u>	<u>5.923</u>	<u>5.943</u>
XMg [*]	.445	.439	.439	.437	.437	.428	.428	.426	.426	.434	.418	.409	.404	.403	.403	.401	.400	.386

^{*}XMg = Mg/(Mg+Fe+Mn)

Simple substitutions that are important in Chatham Island chlorites are $\text{Fe}^{2+}=\text{Mg}$, and $\text{Fe}^{2+}=\text{Mn}$. Some formulae in samples 77, 210B, 224B, and 427 have more than 10 cations per 14 oxygens suggesting that Fe^{3+} substitutes for Al. The exchange substitution $\text{Mg}+\text{Fe}+\text{Mn}(\text{VI}) + \text{Si}(\text{IV}) = \text{Al}(\text{VI}) + \text{Al}(\text{IV})$ is the only important coupled substitution.

Variation in the chemistry of chlorite between samples is much more pronounced than variation in the chemistry of white micas. Figure 20 is a plot of total Al vs. $\text{Mg}/(\text{Mg}+\text{Fe}^{\text{t}}+\text{Mn})$ which is used with the following discussion to illustrate chlorite chemistry. Chlorites from quartz-albite schists (298, 77, 44) are more iron rich than chlorites from greenschists (224B, 427) or the garnet-bearing schist (210B). This relationship has been found in other studies of chlorite in pumpellyite-actinolite facies rocks (Kawachi, 1975). The greenschist samples have chlorites with significant differences in $\text{Mg}/(\text{Mg}+\text{Fe}+\text{Mn})$ that correlate with differences in rock chemistry. In a later section of this thesis a prograde continuous reaction for the breakdown of ferric pumpellyite, is proposed, in which chlorite actinolite, and pumpellyite would be expected to become Mg richer with reaction progress. However, in Chatham Island chlorites which coexist with actinolite and pumpellyite, no unambiguous zoning trend was obtained that would be consistent with this reaction, due most probably to the very fine grain size of the chlorite. Table 5 indicates that for sample 224B both iron-rich rims and Mg-rich rim analyses were obtained. Local equilibria with surrounding minerals may also effect the surrounding chlorite chemistry.

In sample 77 the differences in chlorite analyses (Figure 20) are not systematic and seem to reflect local equilibrium of chlorite with different minerals in the thin section e.g. white mica, or actinolite. The low Al chlorites are in equilibrium with actinolite, whereas the more aluminous chlorites are in equilibrium with white mica. These apparently localized equilibria may reflect the more poorly recrystallized nature of this rock compared to others in this study.

Chlorites from Sample 210B contain a significantly larger amount of Mn, a result of the unusual bulk chemistry of the rock. The chlorites in sample 210B are coarser-grained than other samples, so that detection of chemical zoning was easier with the microprobe. The two most iron-rich and aluminous analyses are from the cores of chlorites, while the more Mg-rich analyses are from rims. This difference in chemistry reflects a reaction, in which chlorite plus epidote plus calcite are reacting to form garnet, and which is limited by diffusion of Al and Fe^{2+} out of chlorite. This reaction is discussed in detail below.

In summary, chlorite chemistry is mainly dependent on bulk chemistry of rocks. Quartz-albite schist chlorites are more ferrous than greenschist chlorites, assuming all measured iron is ferrous iron. Local equilibrium with surrounding minerals also has a slight influence on chlorite composition.

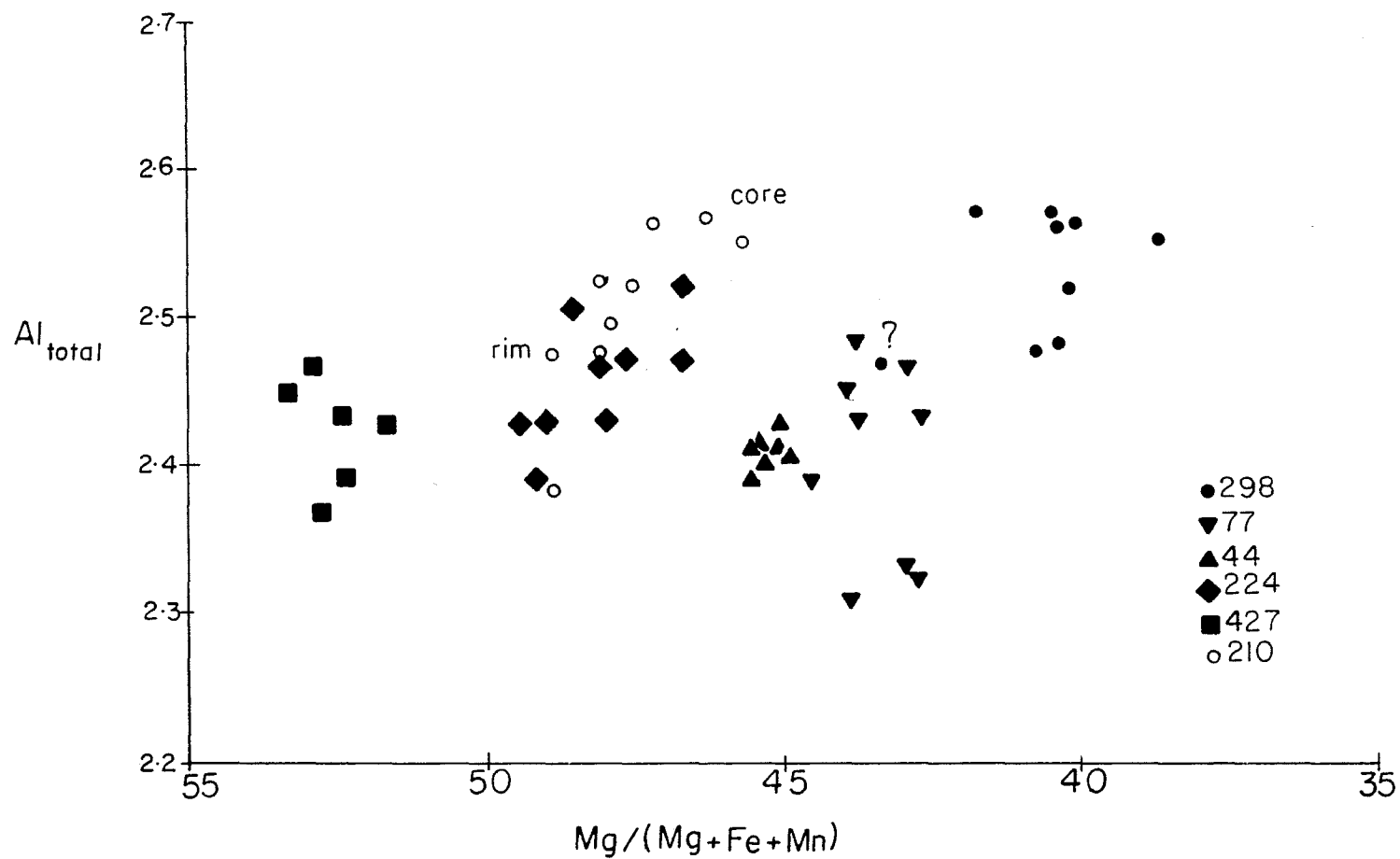


Figure 20. Chlorite analyses in terms of Al. vs. $Mg/(Mg+Fe+Mn)$.

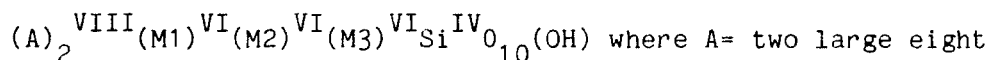
Table 6. Relation between compositional parameters and some optical properties of analyzed chlorites.

Sample number	427	224	210	44	77	298
Mg/ (Mg+Fe+Mn)	.534-.516	.494-.466	.488-.456	.458-.449	.445-.426	.433-.386
Mg/ ((Mg+Fe)	.542-.519	.497-.470	.497-.466	.462-.453	.449-.429	.438-.388
Al per 14 oxygens	2.370-2.462	2.388-2.521	2.380-2.584	2.382-2.446	2.312-2.481	2.472-2.574
sign of elongation	(-)	(-) or (+)	(-) or (+)	(+)	(+)	(+)
abnormal interference color	brown	brown or violet	brown or violet	blue	blue	blue

Epidote-Clinzoisite

Thin section description. Epidote occurs as 0.17 - 0.24 mm diameter anhedral, spongy, embayed, partially disaggregated, yellow green crystals, and as smaller 0.05 - 0.20 mm diameter, anhedral and subhedral crystals. The latter commonly have green-colored cores and colorless rims, with the rim width much greater than the core diameter. The disaggregated variety of epidote is more common in the quartz-albite schist samples 44 and 77 than in the other samples. Epidote in quartz-albite schists occurs in the compositional layers defined by white mica, chlorite, pumpellyite, and sphene. Epidote in greenschists also occurs in smaller spongy aggregates similar to those in quartz-albite schists, but also occurs as individual subhedral crystals with mosaic articulation. In sample 210B epidote within the compositional layers is flattened. The epidote appears to have been elongated during recrystallization associated with the second deformation. It is interesting to note that the colorless rims are wide parallel to the foliation whereas the colorless rims are very thin or nonexistent perpendicular to the foliation. Epidote has negative optic sign, $2V=87-90^\circ$, and birefringence which varies from the cores to the rims.

Chemistry. The structural formula of epidote is



coordinated sites filled primarily by Ca, and (M1), (M2), and (M3) are three unequal octahedrally coordinated sites. Crystal refinement data by Dollase (1971), and Mossbauer spectroscopy studies by Bancroft et al., (1967) indicate that Fe^{3+} is preferentially distributed in the larger and more distorted (M3) site. Minor Fe^{3+} also occurs in (M1), but no Fe^{3+} has been found in (M2). The tetrahedral site is filled primarily with Si and minor Al.

Holdaway (1965), Strens (1965), Hietanen (1974), and Raith (1976) have reported a composition gap in the clinozoisite-epidote series in the greenschist facies. Subsequently in other studies, epidote compositions within the proposed solvus region have been found (Kawachi, 1975; Liou, 1983; Coombs et al., 1976; this study).

Epidote analyses are listed in Table 7. Structural formulae have been recalculated assuming total Fe as Fe^{3+} . The conversion was made by changing molecular proportion FeO into molecular proportion Fe_2O_3 and then calculating a structural formula based on 12.5 oxygens.

Epidote analyses are plotted on a frequency diagram vs. $Fe^{3+}/(Fe^{3+}+Al)$ in Figure 21. The amount of Fe^{3+} which substitutes for Al in epidotes apparently controls the intensity of the characteristic green color of the mineral (Bancroft, 1967). Chatham Island epidotes all have cores that are richer in Fe^{3+} compared with rims. However, inconsistent rim compositions, and the presence of earlier-formed strongly colored epidotes in some samples, suggests that slow diffusion

Table 7. Electron microprobe analyses of epidote. Structural formulae calculated on the basis of 12.5 oxygens assuming all iron measured is Fe_2O_3 .

Number	core					core					core			
	<u>77-1</u>	<u>77-2</u>	<u>77-3</u>	<u>77-4</u>	<u>77-5</u>	<u>224-1</u>	<u>224-2</u>	<u>224-3</u>	<u>224-4</u>	<u>224-5</u>	<u>44-1</u>	<u>44-2</u>	<u>44-3</u>	<u>44-4</u>
SiO_2	37.43	37.72	37.19	37.80	37.34	37.34	37.66	37.63	38.33	38.65	37.17	37.80	37.69	37.96
TiO_2	0.05	0.18	0.03	0.05	0.03	0.09	0.00	0.08	0.10	0.10	0.08	0.00	0.03	0.07
Al_2O_3	21.35	21.29	23.73	24.53	24.76	22.84	23.19	23.96	25.36	25.13	26.02	25.52	25.44	25.48
Fe_2O_3	16.21	15.41	13.54	12.19	12.03	13.78	13.49	12.47	10.82	10.64	11.02	10.48	10.12	9.59
MnO	0.11	0.11	0.26	0.24	0.57	0.16	0.10	0.05	0.01	0.12	0.07	0.06	0.04	0.11
MgO	0.04	0.06	0.06	0.05	0.05	0.08	0.07	0.08	0.07	0.09	0.07	0.06	0.06	0.04
CaO	22.40	22.28	23.18	22.84	22.97	22.95	22.72	23.20	23.79	23.47	23.44	23.11	23.99	23.13
Na_2O	0.00	0.00	0.02	0.00	0.00	0.01	0.00	0.00	0.00	0.00	0.00	0.00	0.00	0.00
K_2O	<u>0.00</u>	<u>0.00</u>	<u>0.00</u>	<u>0.00</u>	<u>0.00</u>	<u>0.00</u>	<u>0.00</u>	<u>0.01</u>	<u>0.01</u>	<u>0.02</u>	<u>0.05</u>	<u>0.02</u>	<u>0.03</u>	<u>0.00</u>
Total	97.59	97.05	98.01	97.70	97.75	97.25	97.23	97.48	98.49	98.22	97.92	97.05	97.40	96.38
Structural formulae based on 12.5 oxygens														
Si	3.016	3.046	2.964	2.999	2.968	3.000	3.016	2.999	3.005	3.033	2.937	3.001	3.003	3.026
Al			0.036	0.001	0.032			0.001			0.063			
	<u>3.016</u>	<u>3.046</u>	<u>3.000</u>	<u>3.000</u>	<u>3.000</u>	<u>3.000</u>	<u>3.016</u>	<u>3.000</u>	<u>3.005</u>	<u>3.033</u>	<u>3.000</u>	<u>3.001</u>	<u>3.003</u>	<u>3.026</u>
Al	<u>2.000</u>	<u>2.000</u>	<u>2.000</u>	<u>2.000</u>	<u>2.000</u>	<u>2.000</u>	<u>2.000</u>	<u>2.000</u>	<u>2.000</u>	<u>2.000</u>	<u>2.000</u>	<u>2.000</u>	<u>2.000</u>	<u>2.000</u>
	<u>2.000</u>	<u>2.000</u>	<u>2.000</u>	<u>2.000</u>	<u>2.000</u>	<u>2.000</u>	<u>2.000</u>	<u>2.000</u>	<u>2.000</u>	<u>2.000</u>	<u>2.000</u>	<u>2.000</u>	<u>2.000</u>	<u>2.000</u>
Al	0.028	0.026	0.193	0.293	0.288	0.162	0.189	0.251	0.343	0.324	0.360	0.388	0.389	0.394
Fe^{3+}	0.983	0.936	0.812	0.728	0.720	0.833	0.813	0.748	0.638	0.628	0.655	0.626	0.607	0.575
Ti	0.003	<u>0.011</u>	<u>0.002</u>	<u>0.003</u>	<u>0.002</u>	<u>0.005</u>	<u>0.000</u>	<u>0.005</u>	<u>0.006</u>	<u>0.006</u>	<u>0.005</u>	<u>0.000</u>	<u>0.002</u>	<u>0.004</u>
	1.014	0.973	1.007	1.024	1.010	1.000	1.002	1.004	0.987	0.958	1.020	1.014	0.998	0.973
Mg	0.008	0.007	0.007	0.006	0.006	0.010	0.008	0.010	0.008	0.011	0.008	0.007	0.007	0.005
Mn	0.007	0.008	0.018	0.016	0.038	0.011	0.007	0.003	0.001	0.008	0.005	0.004	0.003	0.007
Ca	1.934	1.928	1.980	1.942	1.956	1.975	1.950	1.981	1.987	1.973	1.984	1.966	1.984	1.975
Na			0.003			0.001								
K								0.001	0.001	0.002	0.005	0.002	0.003	
	<u>1.949</u>	<u>1.943</u>	<u>2.008</u>	<u>1.964</u>	<u>2.000</u>	<u>1.997</u>	<u>1.965</u>	<u>1.995</u>	<u>1.997</u>	<u>1.994</u>	<u>2.002</u>	<u>1.979</u>	<u>1.997</u>	<u>1.987</u>
XFe^{3+}	.326	.316	.267	.241	.237	.278	.271	.249	.214	.213	.222	.213	.203	.194
$\text{XFe}^{3+} = \text{Fe}^{3+} / (\text{Fe}^{3+} + \text{Al})$														

Table 7. continued.

Number	210-1	210-2	210-3	210-4	210-5	210-6	210-7	210-8	210-9	210-10	427-1	427-2	427-3	427-4	298-1	298-2	298-3	298-4	298-5
	core	core			rim	rim				rim						core			rim
SiO ₂	37.01	36.88	37.58	37.37	37.17	37.13	37.57	37.31	38.14	37.92	37.42	37.38	37.82	37.88	35.34	37.63	37.33	36.75	37.19
TiO ₂	0.02	0.09	0.12	0.11	0.21	0.13	0.12	0.17	0.28	0.33	0.04	0.05	0.06	0.03	0.16	0.09	0.23	0.16	0.19
Al ₂ O ₃	20.59	20.56	22.87	25.59	25.30	25.32	25.92	25.86	27.93	28.32	26.30	26.28	25.87	26.57	25.23	24.96	27.47	26.72	27.00
Fe ₂ O ₃	16.70	16.57	14.05	11.36	11.19	11.15	10.88	10.56	7.50	6.96	10.56	10.40	10.20	9.26	11.80	11.46	9.00	8.63	8.31
MnO	1.33	1.46	0.77	0.43	0.56	0.55	0.54	0.50	0.34	0.38	0.12	0.13	0.09	0.13	0.18	0.17	0.12	0.22	0.12
MgO	0.07	0.05	0.12	0.04	0.28	0.04	0.04	0.07	0.19	0.08	0.07	0.10	0.06	0.09	0.08	0.08	0.14	0.15	0.15
CaO	21.83	21.73	22.33	22.23	22.52	22.35	22.78	22.77	23.48	23.04	24.30	24.09	23.84	23.87	23.35	23.45	23.82	23.66	23.13
Na ₂ O	0.00	0.00	0.00	0.00	0.00	0.00	0.00	0.00	0.00	0.00	0.00	0.02	0.01	0.00	0.00	0.00	0.00	0.00	0.00
K ₂ O	0.00	0.01	0.05	0.04	0.01	0.00	0.04	0.02	0.00	0.02	0.00	0.00	0.00	0.00	0.00	0.04	0.01	0.03	0.03
Total	97.55	97.35	97.89	97.17	97.24	96.67	97.89	97.26	97.86	97.05	98.81	98.45	97.95	97.83	96.14	97.88	98.12	96.32	96.12
Structural formulae based on 12.5 oxygens																			
Si	3.006	3.002	3.003	2.951	2.959	2.970	2.965	2.962	2.975	2.974	2.932	2.936	2.975	2.977	2.875	2.979	2.924	2.935	2.963
Al	3.006	3.002	3.003	0.049	0.041	0.030	0.035	0.038	0.025	0.026	0.068	0.064	0.025	0.023	0.125	0.021	0.076	0.065	0.037
				3.000	3.000	3.000	3.000	3.000	3.000	3.000	3.000	3.000	3.000	3.000	3.000	3.000	3.000	3.000	3.000
Al	1.971	1.973	2.000	2.000	2.000	2.000	2.000	2.000	2.000	2.000	2.000	2.000	2.000	2.000	2.000	2.000	2.000	2.000	2.000
	1.971	1.973	2.000	2.000	2.000	2.000	2.000	2.000	2.000	2.000	2.000	2.000	2.000	2.000	2.000	2.000	2.000	2.000	2.000
Al			0.154	0.332	0.332	0.357	0.376	0.382	0.542	0.591	0.360	0.369	0.377	0.438	0.280	0.308	0.460	0.450	0.498
Fe ³⁺	1.021	1.015	0.845	0.675	0.670	0.671	0.646	0.631	0.440	0.411	0.623	0.615	0.604	0.548	0.718	0.683	0.531	0.519	0.498
Ti	0.001	0.006	0.007	0.007	0.013	0.008	0.007	0.010	0.016	0.019	0.002	0.003	0.004	0.002	0.010	0.005	0.014	0.010	0.011
	1.022	1.021	1.006	1.014	1.015	1.036	1.029	1.023	0.998	1.021	0.985	0.987	0.985	0.988	1.008	0.996	1.005	0.979	1.007
Mg	0.008	0.006	0.014	0.005	0.033	0.005	0.005	0.008	0.022	0.009	0.008	0.012	0.007	0.011	0.010	0.009	0.016	0.018	0.018
Mn	0.091	0.101	0.052	0.029	0.038	0.037	0.036	0.034	0.022	0.025	0.008	0.009	0.006	0.009	0.012	0.011	0.008	0.015	0.008
Ca	1.899	1.895	1.912	1.965	1.921	1.915	1.926	1.937	1.962	1.936	2.040	2.028	2.012	2.010	2.024	1.989	1.999	2.025	1.974
Na													0.003	0.001					
K		0.001	0.005	0.004	0.001		0.004	0.002		0.002						0.004	0.001	0.003	0.003
	1.998	2.003	1.983	2.003	1.993	1.957	1.971	1.981	2.006	1.972	2.056	2.052	2.026	2.030	2.046	2.013	2.024	2.061	2.003
XFe ³⁺ *	.341	.339	.282	.221	.220	.219	.211	.207	.146	.136	.204	.202	.201	.182	.230	.227	.173	.171	.164

* XFe³⁺ = Fe³⁺/(Fe³⁺+Al)

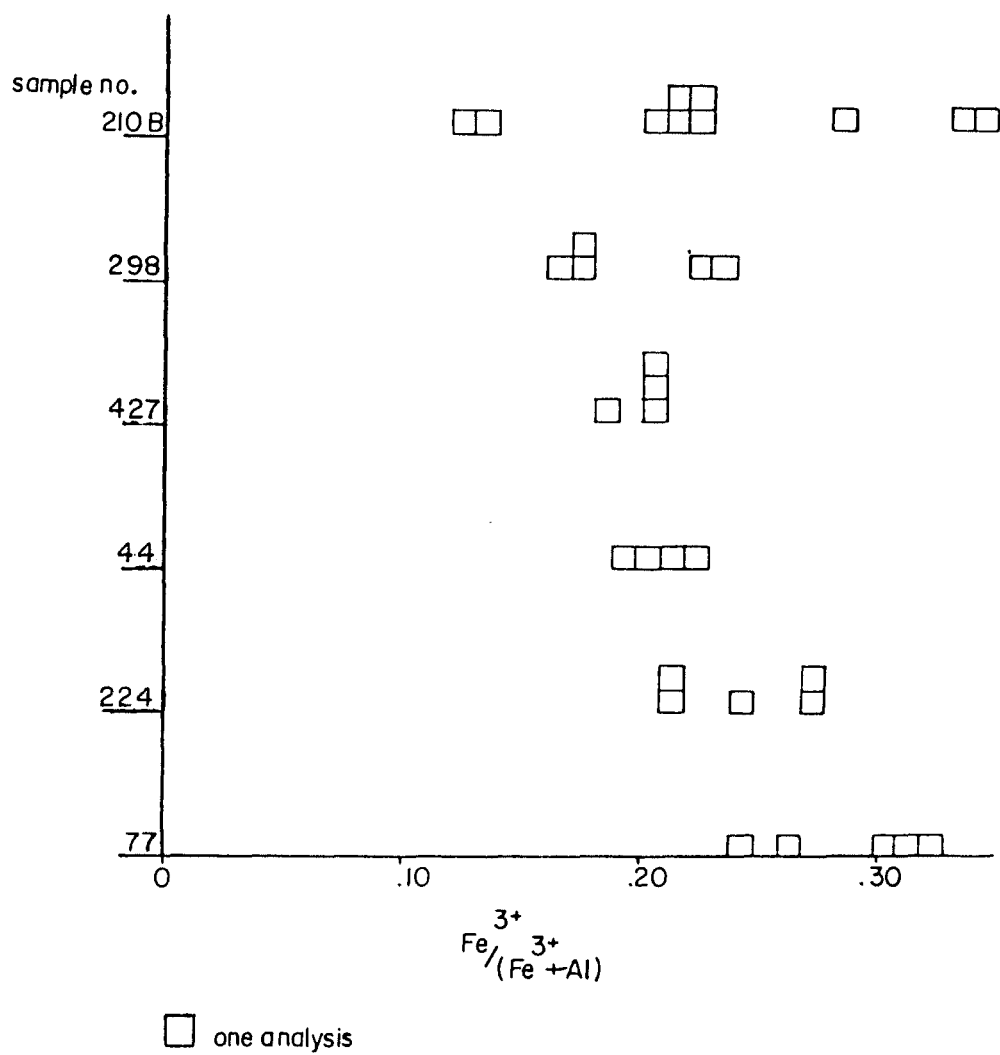


Figure 21. Frequency diagram of epidote analyses .

of Fe^{3+} and Al in epidote effects epidote chemistry. This point may also account for the complicated zoning patterns, the disequilibrium textures observed in samples 210B and 429, the chemistry observed in sample 210B, and the general lack of volume equilibration in epidote from all the samples. The variation of averaged rim compositions in terms of $\text{Fe}^{3+}/(\text{Fe}^{3+}+\text{Al})$ by sample is $210\text{B} < 298 < 427 < 44 < 224\text{B} < 77$.

All Mn measured was assumed to be Mn^{2+} . Sample 210B, the garnet-bearing schist, has the largest substitution of Mn for Ca. Mn ranges in these epidotes from 0.101 in the cores to 0.025 in the rims per 12.5 oxygens, whereas the average Mn in the other samples is only 0.009 per 12.5 oxygens.

Pumpellyite

Thin section description. Pumpellyite occurs in three textural habits in Chatham Island schists. Type 1 pumpellyites are euhedral prismatic crystals with monoclinic forms (Figure 22). End sections perpendicular to the *b*-crystallographic axis have a first order gray interference color and show concentric patterns probably formed during crystal growth (Figure 22a). Type 1 pumpellyite is intergrown with white mica, chlorite, epidote, sphene, and quartz in quartz-albite schists and with chlorite and/or actinolite in greenschists. Type 1 pumpellyite is generally colorless, although some grains have cores that are pleochroic with *Y* = blue-green.

Type 2 pumpellyites illustrated in Figure 22b are anhedral, embayed, and sometimes partially disaggregated crystals. Type 2 pumpellyite is pleochroic with *Y* = blue-green, strong $r \ll v$ dispersion of the optic axes, tan-brown to blue abnormal interference colors, and a variable 2V from 5 to 25 degrees. The abnormal interference color, and the distinct pleochroism are attributed to higher Fe^{3+} content (Seki, 1961). In sample 427 type 2 pumpellyite occurs as anhedral aggregates that appear to be a replacement of earlier minerals, possibly pyroxene, plagioclase, amphibole, or prehnite, and as individual grains which are subhedral to anhedral crystals. The relict grains are wrapped in a matrix of chlorite and euhedral type 1 pumpellyite. Subhedral type 2 pumpellyites also occur within the foliation. In quartz-albite schists type 2 pumpellyite occurs within the white mica chlorite matrix.

Type 3 pumpellyite occurs in the cores of albite grains that are relict plagioclase phenocrysts. The pumpellyites are small anhedral crystals with green pleochroism. This type of pumpellyite grew during diffusion of elements accompanying albitization of plagioclase and resulted because Ca and Al were slower to diffuse out of the grains during low grade metamorphism than for the other elements to diffuse into the plagioclase.

Type 2 and 3 pumpellyites have been discussed in the literature by Kawachi (1975); Coombs et al., (1976); Kuniyoshi and Liou (1976); Trzcienski (1980); and Robinson (1958). No clear descriptions of type 1

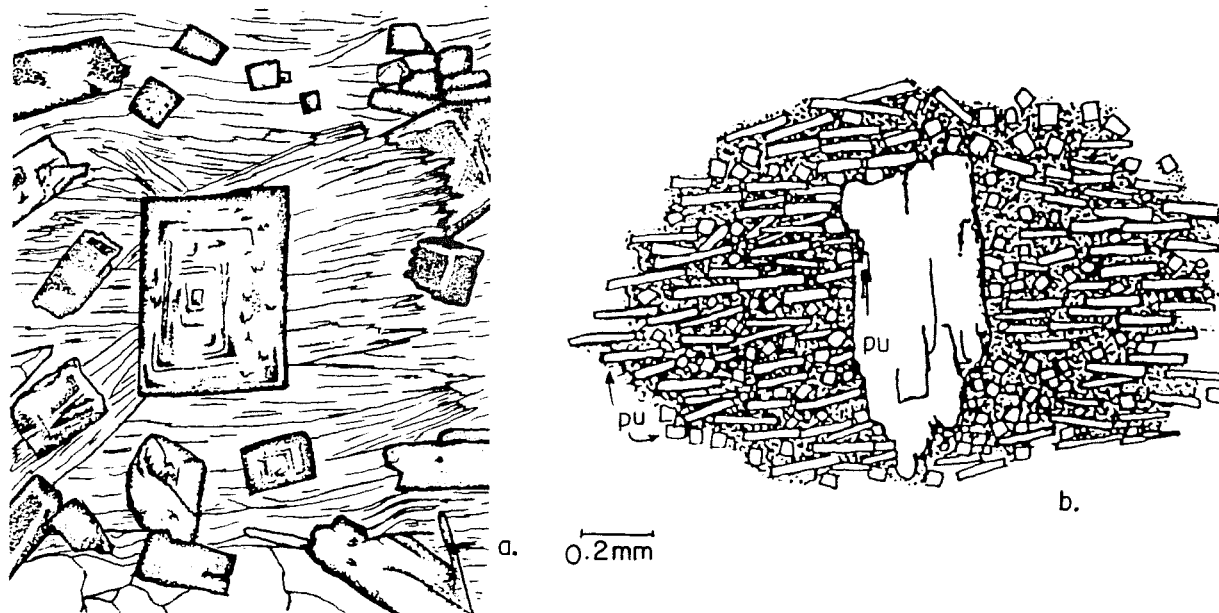


Figure 22a. Euhedral type 1 pumpellyite in a matrix of white mica and minor chlorite from sample 298. 22b. Anhedral type 2 pumpellyite from sample 427 in a matrix of chlorite and type 1 pumpellyite.

pumpellyite were found in the literature.

The unusually well developed crystal faces of type 1 pumpellyite allow optic properties to be related to crystal orientation. Figure 23a is an example of the standard optic orientation of pumpellyite (Coombs, 1953). The optic orientation in Type 1 pumpellyite in samples 77, 298, and 224B is generally similar to pumpellyite shown in this figure. The intermediate vibration direction Y is parallel to the elongated \bar{b} -axis direction of the crystal, indicating pumpellyite can have either positive or negative elongation. In the type 1 pumpellyite grains oriented correctly to show positive elongation, they show this only weakly because of the low 2V, such that the α and β indices in X and Y vibration directions are close to each other. A few pumpellyite crystals lying parallel to the \bar{b} -crystallographic axis were large enough to obtain interference figures yielding the following optical properties: Positive optic sign; small but variable 2V from less than 5° to 20° ; dispersion $r < v$. Optic examination of sections cut parallel to 010 indicates that the extinction angles ZAc and XAa vary between samples. End sections in sample 298 are optically zoned in a complex manner. We examined three regions of the crystal illustrated in Figure 23a and the extinction angles determined from each region are reported. This unusual zoning pattern suggests that pumpellyite may grow as hollow ended crystals or "hopper crystals". Angles determined for samples 224B, and 77 and other crystals in sample 298 are also given in Figure 23a.

Type 1 pumpellyite in sample 427 appears to be very different than type 1 pumpellyite in the other samples studied. Examination of sign of elongation indicates that all type 1 pumpellyite crystals in sample 427 have negative elongation. A logical explanation may be that the 2V has passed through zero and the optic orientation has changed so that the X vibration direction rather than the Y vibration direction is parallel to the long axes of the crystals. This is shown in Figure 23b. Coombs (1953) shows the refractive indices of pumpellyite related to the total iron content as wt.% Fe_2O_3 . At progressively lower total iron content his β and α refractive indices converge, and might intersect at a value slightly below 3 wt.% total iron, beyond the edge of his diagram. The possible switch in optic orientation in Chatham Island pumpellyite from sample 427 is presumably a function of decreased iron content. In end section, the pumpellyite from sample 427 also shows a different orientation of the Z and Y (?) vibration directions with respect to the \bar{c} - and \bar{a} - crystallographic axes as shown in the lower part of Figure 23. Although it is not certain, such a change in ZAc is consistent with the direction of change of ZAc with decreasing Fe content in sample 298, illustrated in the top of Figure 23. The microprobe data discussed further on does not however suggest the exact relationship between the optic orientation and the chemical composition.

Chemistry. The general formula for pumpellyite proposed by Passaglia and Gottardi (1973), and modified by Coombs et al., (1976) is $W_4X_2Y_4Z_6O_{20+x}(OH)_{8-x}$, where is general $W=(Ca, Mn, Fe^{2+})$ $X=(Mg, Fe^{2+})$,

$\text{Mn})_{2-x}(\text{Fe}^{3+}, \text{Al})_x$, $\text{Y}=(\text{Fe}^{3+}, \text{Al})$ and $\text{Z}=(\text{Si}, \text{Al})$. The crystal structure of pumpellyite has been determined by Galli and Alberti (1969), and refined by Allmann and Donnay (1971). Solid solution occurs between Fe^{2+} and Mg, and between Fe^{3+} and Al. Solid solution between the Fe^{2+} and Mg, and between Fe^{3+} and Al. Solid solution between the Fe^{2+} - Fe^{3+} endmember (julgoldite) and the Fe^{3+} -free member exists, but complete solution has not been proven. Trzcinski and Birkett (1981) found up to 2 wt.% V_2O_5 in pumpellyite from the western margin of the Appalachians.

Electron microprobe analyses of pumpellyite are listed in Table 8 and a structural formula for each analysis is recalculated based on 16 cations and 24.5 oxygens per formula unit. Fe^{3+} has been added from Fe^{2+} as needed to balance charges. The analyses have been separated by textural type in order to emphasize the difference in chemistry between type 1 and type 2 pumpellyites. No analyses were obtained of type 3 pumpellyites due to their small grain size.

Figure 24 illustrates the plotting position of pumpellyite composition space on an Al- Fe^{total} -Mg diagram (Coombs et al., 1969). Also shown on the figure are pumpellyite compositions from other occurrences worldwide. Chatham Island pumpellyites, especially textural type 2, are similar in composition to pumpellyites from other intermediate- to high-pressure low-temperature terranes. Figure 25 is an enlargement of part of the compositional space and illustrates the compositional variation of pumpellyite among the samples and within each sample. It is clear from Figure 25 that type 2 pumpellyites are less aluminous than type 1 pumpellyites and must contain more ferric iron. Type 1 pumpellyites form a fairly tight cluster of analyses although there are some important differences. Pumpellyites from sample 427 are less aluminous than all the type 1 pumpellyites from sample 224B. The quartz-albite schist samples form a tighter cluster and there is overlap in the data. Two exceptions are the core analyses from sample 298 (Figure 23) which are more aluminous and much more ferrous than the rim analyses.

Figure 26 is a composite diagram illustrating the differences in $\text{Mg}/(\text{Mg}+\text{Fe}^{2+}+\text{Mn})$ vs. $\text{Fe}^{3+}/(\text{Fe}^{3+}+\text{Al})$ for all pumpellyite microprobe analyses. Distinct differences between type 2 pumpellyite and type 1 pumpellyite are obvious. Type 2 pumpellyites are less aluminous than type 1 pumpellyites and therefore contain more ferric iron. For samples 77, 298, and 224 type 2 pumpellyites are more ferrous than type 1 pumpellyites. This trend is not clearly shown by sample 427. It is important to note that the analyses do not reflect the relative abundance of the type of pumpellyite in each sample, but this is a function of the difficulty in obtaining good analyses of type 2 pumpellyites. Zoning trends in type 1 pumpellyites are complicated. Analyses from the crystal from sample 298 illustrated in Figure 23 suggest that type 1 pumpellyite initially nucleated as iron-rich pumpellyite (analyses 298-9, 298-10) and became Mg richer (298-2), approaching bulk rock composition. This complicated zoning pattern

Figure 23. Two different optic orientation diagrams of pumpellyite.

- 23a. Optic orientation of pumpellyite in samples 298, 77, 44, and 224B is shown on the left. On the right the variation of the optical properties of pumpellyite in a zoned crystal from sample 298. The optical properties vary from core to rim as illustrated by areas "A", "B", and "C". Microprobe data from core and rim areas are listed below:

	Mg/(Mg+Fe ²⁺ +Mn)
core area A	.366
rim area C	.734

Additional data from samples 224B and 77:

	Z \wedge c	X \wedge a
224B	7	14
	6	11
	8	15
	2	9
77	15	20
	12	17
	2	8

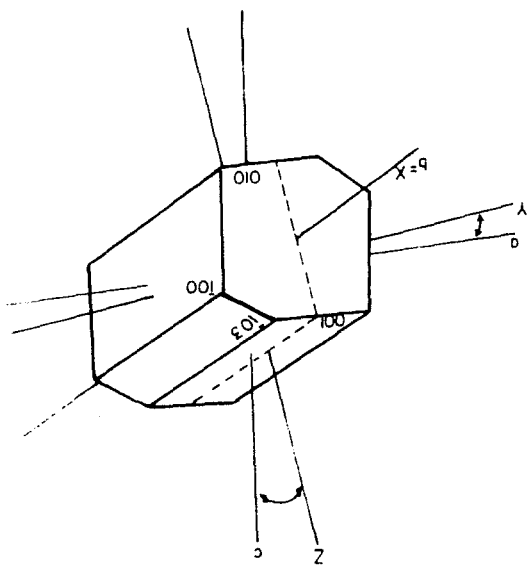
- 23b. The probable optic orientation of pumpellyite from sample 427. The change in optical properties is probably a result of the low total iron content of pumpellyite in this sample. Note that the optic plane has changed orientation and that Z vibrates in the obtuse angle β as opposed to the acute angle β as in the other samples studied.

Additional measurements from sample 427:

Z \wedge c	Y \wedge a
11	3

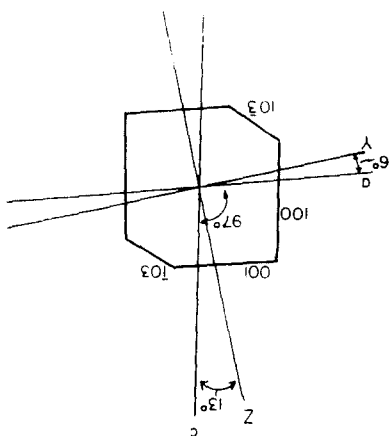
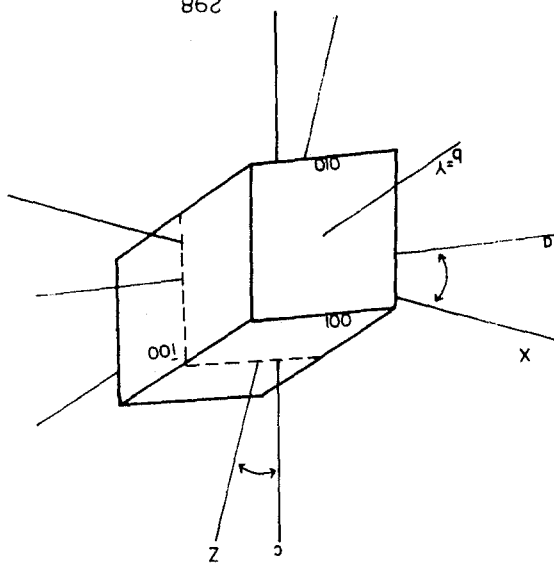
b.

427

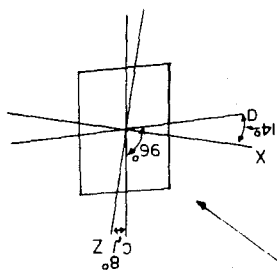


D.

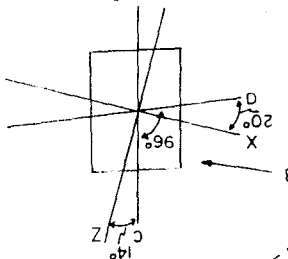
298



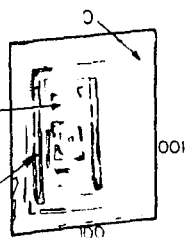
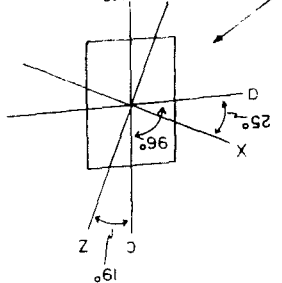
C



B



A



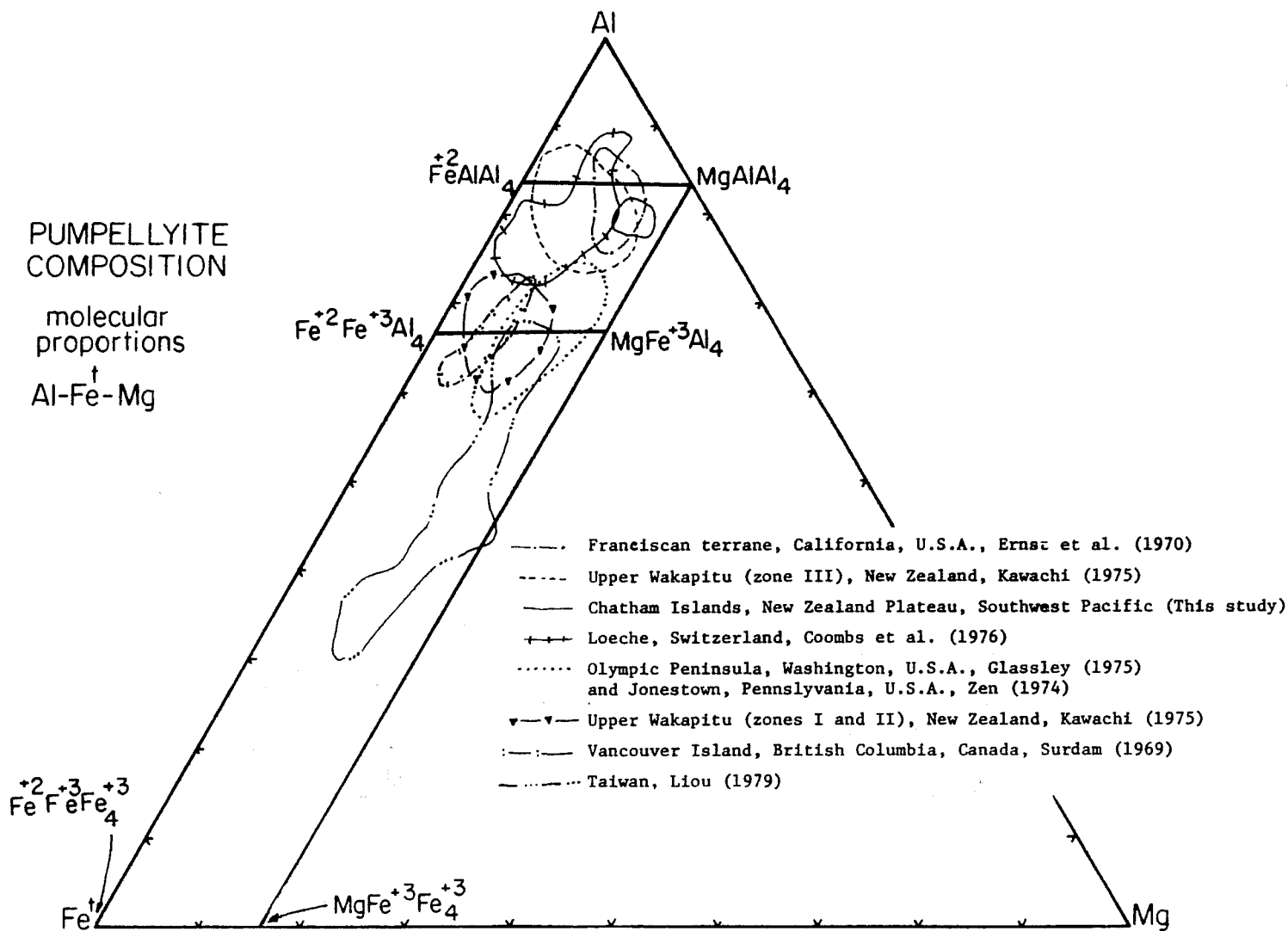


Figure 24. Pumpellyite composition space in terms of molecular proportion Al-Fe-Mg (Coombs et al. 1976). Pumpellyite composition from other metamorphic terranes are also shown.

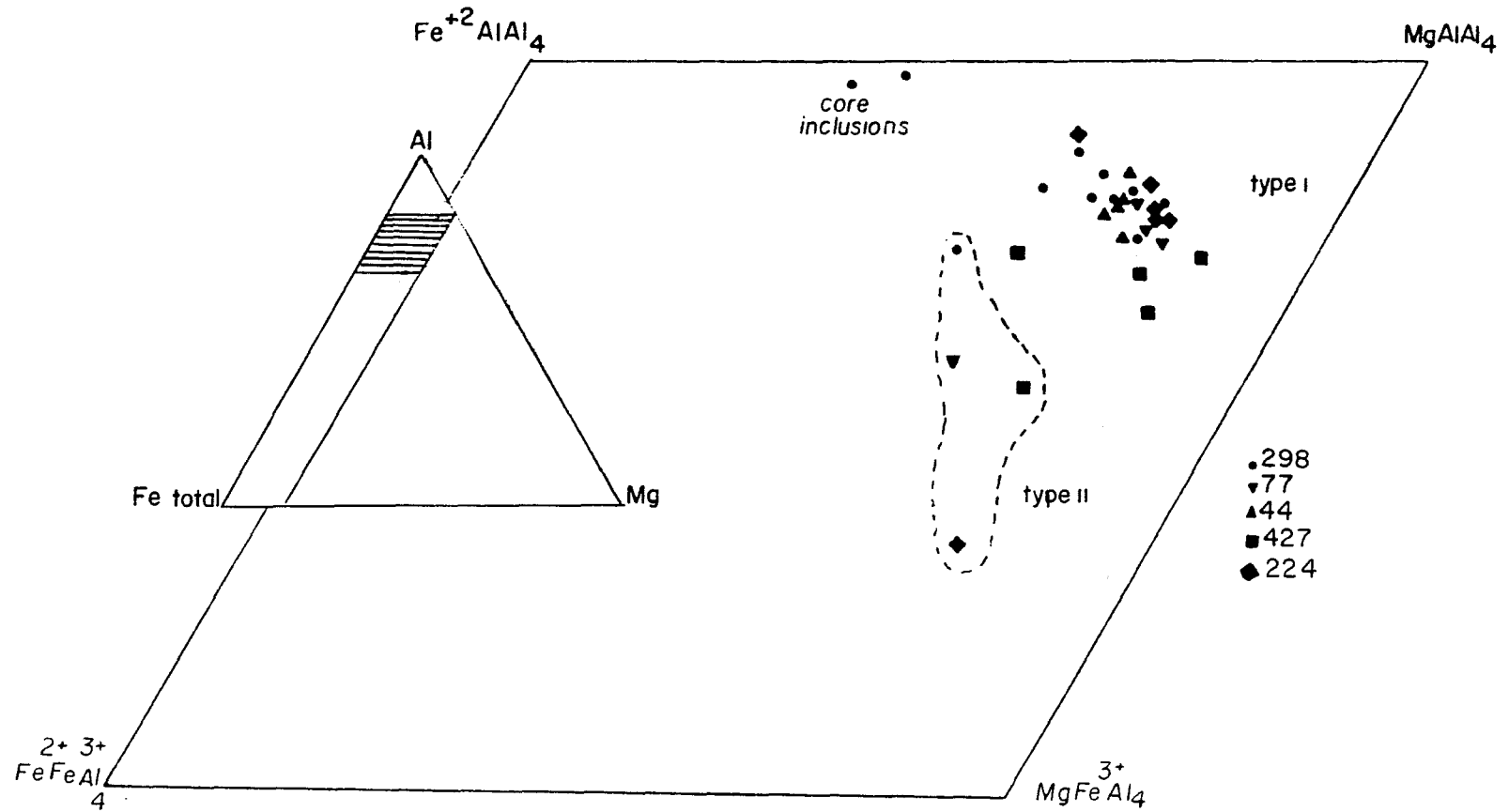


Figure 25. Pumpellyite analyses from Chatham Island schist plotted in terms of Al-Fe_{total}-Mg. (Coombs et al., 1976).

Table 8. Electron microprobe analyses of pumpellyite. Structural formulae calculated on the basis of 16 cations and 24.5 oxygens.

Type	<u>224-1</u>	<u>224-2</u>	<u>224-3</u>	<u>224-4</u>	<u>224-5</u>	<u>224-6</u>	<u>427-1</u>	<u>427-2</u>	<u>427-3</u>	<u>427-4</u>	<u>427-5</u>	<u>427-6</u>	<u>427-7</u>
	1	1	1	1	?	2	1	1	1	1	1	1	2
SiO ₂	36.66	36.84	37.72	36.94	36.77	36.88	37.26	37.95	37.80	37.17	37.19	36.71	36.25
TiO ₂	0.07	0.06	0.15	0.01	0.10	0.02	0.16	0.04	0.01	0.10	0.14	0.08	0.01
Al ₂ O ₃	25.06	24.73	25.20	24.81	25.15	23.75	24.77	24.25	25.42	24.85	24.19	24.66	23.75
Fe ₂ O ₃	1.81	1.55	0.85	1.58	1.18	4.26	.09	1.94	1.72	2.37	1.77	2.26	4.36
FeO	1.29	1.27	2.28	1.70	2.20	2.29	2.80	1.21	1.85	0.98	2.02	2.28	1.07
MnO	0.14	0.16	0.35	0.15	0.21	0.19	0.46	0.40	0.40	0.50	0.59	0.26	0.46
MgO	3.28	3.38	3.46	3.27	2.81	3.09	3.69	3.42	3.58	3.08	3.56	2.80	3.10
CaO	22.86	22.87	22.52	22.76	22.87	23.15	22.64	23.07	22.61	23.30	21.61	22.36	22.44
Na ₂ O	0.00	0.00	0.03	0.00	0.00	0.00	0.05	0.15	0.02	0.06	0.13	0.10	0.10
K ₂ O	<u>0.00</u>	<u>0.00</u>	<u>0.00</u>	<u>0.00</u>	<u>0.00</u>	<u>0.00</u>	<u>0.00</u>	<u>0.00</u>	<u>0.00</u>	<u>0.00</u>	<u>0.00</u>	<u>0.00</u>	<u>0.00</u>
Total	91.17	91.26	92.56	91.22	91.29	93.15	91.92	92.43 [#]	93.41	92.41 ^{##}	91.20 ⁺	91.51	91.54

[#] also .27 Cr₂O₃ ^{##} also .22 Cr₂O₃ + also .28 Cr₂O₃

● analyst R. Tracy (unpublished)

Structural formulae based on 24.5 oxygens and 16 cations													
Si	5.974	6.000	6.053	6.020	5.998	6.086	5.998	6.091	6.015	5.982	6.056	6.024	5.991
Al	<u>.026</u>	<u>.026</u>	<u>.026</u>	<u>.026</u>	<u>.026</u>	<u>.026</u>	<u>.026</u>	<u>.026</u>	<u>.026</u>	<u>.026</u>	<u>.026</u>	<u>.026</u>	<u>.026</u>
	6.000	6.000	6.053	6.020	6.000	6.086	6.000	6.091	6.015	6.000	6.056	6.024	6.000
Al	<u>4.000</u>	<u>4.000</u>	<u>4.000</u>	<u>4.000</u>	<u>4.000</u>	<u>4.000</u>	<u>4.000</u>	<u>4.000</u>	<u>4.000</u>	<u>4.000</u>	<u>4.000</u>	<u>4.000</u>	<u>4.000</u>
	4.000	4.000	4.000	4.000	4.000	4.000	4.000	4.000	4.000	4.000	4.000	4.000	4.000
Al	.787	.747	.765	.765	.833	.288	.699	.587	.767	.697	.642	.711	.500
Fe ³⁺	.221	.240	.103	.193	.145	.536	.081	.235	.206	.289	.216	.226	.546
Ti	.009	.007	.018	.001	.012	.002	.019	.005	.001	.012	.017	.010	.001
Cr								.034		.028	.036		
Mg	.796	.821	.827	.794	.683	.771	.885	.818	.849	.739	.864	.687	.763
Fe ²⁺	.177	.173	.287	.226	.300	.320	.316	.162	.177	.132	.225	.366	.148
Mn	<u>.010</u>	<u>.012</u>	<u>.012</u>	<u>.021</u>	<u>.026</u>	<u>.027</u>	<u>.016</u>	<u>.047</u>	<u>.006</u>	<u>.019</u>	<u>.042</u>	<u>.032</u>	<u>.042</u>
	2.000	2.000	2.000	1.997	2.000	1.944	2.000	1.896	2.000	1.964	2.000	2.000	2.000
Fe ²⁺							.019		.069		.050	.001	.001
Mn	.009	.010	.048		.003		.063		.054		.082	.036	.032
Ca	3.991	3.991	3.871	3.974	3.997	3.992	3.905	3.967	3.855	4.018	3.770	3.953	3.974
Na			.019				.016	.047	.006	.019	.042	.032	.032
	<u>4.000</u>	<u>4.001</u>	<u>3.938</u>	<u>3.980</u>	<u>4.000</u>	<u>3.992</u>	<u>4.003</u>	<u>4.014</u>	<u>3.984</u>	<u>4.037</u>	<u>3.944</u>	<u>4.022</u>	<u>4.007</u>
XMg [*] **	.656	.654	.654	.643	.590	.466	.649	.644	.627	.602	.601	.521	.498
XFe ³⁺	.044	.048	.021	.039	.029	.112	.017	.049	.041	.044	.044	.055	.108
XMg [▲]	.802	.808	.711	.762	.675	.690	.690	.790	.739	.787	.819	.630	.800
Al	.801	.794	.794	.796	.810	.725	.783	.791	.785	.774	.774	.789	.750
Mg	.132	.137	.138	.133	.114	.130	.147	.141	.140	.144	.144	.113	.127
Fe	.066	.069	.068	.071	.075	.145	.069	.068	.063	.082	.082	.099	.116

* XMg = Mg / (Mg + Fe²⁺ + Mn)

** XFe³⁺ = Fe³⁺ / (Fe³⁺ + Al)

▲ XMg = Mg / (Mg + Fe²⁺ + Mn)

Table 8 continued.

Number	298-1	298-2	298-3	298-4	298-5	298-6	298-7	298-8	298-9	298-10	298-11	77-1	77-2	77-3	77-4	77-5
Type	<u>1</u>	<u>1</u>	<u>1</u>	<u>1</u>	<u>1</u>	<u>1</u>	<u>1</u>	<u>1</u>	<u>1</u>	<u>1</u>	<u>2</u>	<u>1</u>	<u>1</u>	<u>1</u>	<u>1</u>	<u>2</u>
SiO ₂	38.10	37.90	37.61	37.34	37.26	37.42	37.84	37.11	37.39	37.33	36.94	37.34	37.05	36.93	36.55	37.56
TiO ₂	0.13	0.08	0.06	0.07	0.08	0.04	0.09	0.03	0.00	0.04	0.04	0.10	0.06	0.13	0.06	0.04
Al ₂ O ₃	25.90	25.71	25.38	24.25	24.75	25.29	25.81	24.80	26.50	26.44	25.08	24.13	25.34	24.84	24.20	24.42
Fe ₂ O ₃	0.56	1.56	1.07	1.54	0.56	0.44	1.37	1.45	0.40	0.36	1.85	1.92	2.86	1.85	3.11	4.53
FeO	2.55	1.57	2.37	1.90	2.76	3.07	2.38	2.21	4.01	4.89	3.34	1.40	0.76	2.10	0.85	1.29
MnO	0.31	0.65	0.44	0.79	0.50	0.36	0.43	0.52	0.25	0.25	0.24	0.40	0.47	0.53	0.55	0.24
MgO	3.22	3.45	3.00	3.23	2.91	2.81	2.98	2.94	1.84	1.55	2.54	3.33	3.24	3.19	3.11	2.98
CaO	23.04	22.93	22.88	22.51	22.40	22.64	23.08	22.69	23.17	23.14	22.42	22.87	23.32	22.32	22.99	22.94
Na ₂ O	0.00	0.00	0.00	0.00	0.00	0.00	0.00	0.00	0.00	0.00	0.00	0.07	0.00	0.00	0.00	0.00
K ₂ O	<u>0.00</u>	<u>0.03</u>	<u>0.05</u>	<u>0.02</u>	<u>0.05</u>	<u>0.00</u>	<u>0.03</u>	<u>0.00</u>	<u>0.00</u>	<u>0.00</u>	<u>0.01</u>	<u>0.00</u>	<u>0.00</u>	<u>0.00</u>	<u>0.01</u>	<u>0.04</u>
Total	93.81	93.88	92.86	91.65	91.27	92.07	94.01	91.75	93.56	94.00	92.46	91.58	93.10	91.89	91.43	93.04
Structural formulae based on 24.5 oxygens and 16 cations																
Si	6.033	6.001	6.036	6.072	6.080	6.057	5.999	6.032	5.979	5.977	5.988	6.071	5.930	5.995	5.972	6.003
Al	<u>6.033</u>	<u>6.001</u>	<u>6.036</u>	<u>6.072</u>	<u>6.080</u>	<u>6.057</u>	<u>6.000</u>	<u>6.032</u>	<u>6.021</u>	<u>6.023</u>	<u>6.012</u>	<u>6.071</u>	<u>6.070</u>	<u>6.005</u>	<u>6.028</u>	<u>6.003</u>
Al	<u>4.000</u>	<u>4.000</u>	<u>4.000</u>	<u>4.000</u>	<u>4.000</u>	<u>4.000</u>	<u>4.000</u>	<u>4.000</u>	<u>4.000</u>	<u>4.000</u>	<u>4.000</u>	<u>4.000</u>	<u>4.000</u>	<u>4.000</u>	<u>4.000</u>	<u>4.000</u>
Al	<u>4.000</u>	<u>4.000</u>	<u>4.000</u>	<u>4.000</u>	<u>4.000</u>	<u>4.000</u>	<u>4.000</u>	<u>4.000</u>	<u>4.000</u>	<u>4.000</u>	<u>4.000</u>	<u>4.000</u>	<u>4.000</u>	<u>4.000</u>	<u>4.000</u>	<u>4.000</u>
Al	.834	.798	.794	.655	.760	.824	.822	.751	.973	.966	.779	.621	.711	.747	.632	.599
Fe ³⁺	.067	.186	.129	.189	.069	.053	.164	.177	.048	.046	.226	.235	.344	.266	.383	.394
Ti	.016	.010	.007	.008	.010	.005	.011	.004		.005	.005	.012	.007	.016	.007	.005
Mg	.760	.814	.716	.783	.708	.677	.705	.712	.439	.370	.537	.806	.772	.771	.757	.709
Fe ²⁺	.323	.192	.319	.258	.377	.409	.298	.300	.536	.608	.453	.190	.102	.240	.116	.293
Mn	<u>2.000</u>	<u>2.000</u>	<u>2.000</u>	<u>2.000</u>	<u>1.993</u>	<u>2.000</u>	<u>2.000</u>	<u>2.000</u>	<u>1.996</u>	<u>2.000</u>	<u>2.000</u>	<u>1.925</u>	<u>1.999</u>	<u>2.000</u>	<u>1.971</u>	<u>2.000</u>
Fe ²⁺	.015	.016					.018				.077			.073		.029
Mn	.042	.087	.025	.001		.017	.058	.016	.034	.029	.027			.045		.033
Ca	3.909	3.890	3.929	3.922	3.916	3.926	3.920	3.952	3.970	3.970	3.894	3.982	3.999	3.882	4.025	3.927
Na												.022				
K		.006	.010	.004	.010		.006				.002					.008
	<u>3.966</u>	<u>3.999</u>	<u>3.964</u>	<u>3.927</u>	<u>3.926</u>	<u>3.943</u>	<u>4.002</u>	<u>3.968</u>	<u>4.004</u>	<u>3.999</u>	<u>4.000</u>	<u>4.004</u>	<u>3.999</u>	<u>4.003</u>	<u>4.025</u>	<u>3.997</u>
XMg [*]	.630	.628	.585	.585	.578	.570	.567	.564	.415	.349	.465	.624	.603	.569	.568	.486
XFe ^{3+***}	.014	.037	.026	.039	.014	.010	.033	.036	.009	.009	.045	.048	.067	.045	.076	.079
XMg [#]	.667	.734	.654	.681	.614	.596	.653	.657	.435	.366	.491	.763	.824	.683	.798	.666
Al	.806	.799	.801	.791	.805	.810	.802	.800	.830	.826	.788	.789	.797	.787	.788	.759
Mg	.127	.135	.120	.133	.120	.113	.118	.120	.073	.064	.101	.138	.129	.128	.128	.117
Fe	.065	.063	.079	.076	.075	.077	.080	.080	.097	.110	.111	.073	.074	.085	.084	.114

* XMg = Mg / (Mg + Fe²⁺ + Mn)** XFe³⁺ = Fe³⁺ / (Fe³⁺ + Al)# XMg = Mg / (Mg + Fe²⁺ + Mn)

Table 8 continued.

Number	<u>44-1</u>	44-2	<u>44-3</u>	<u>44-4</u>
Type	<u>1</u>	<u>1</u>	<u>1</u>	<u>1</u>
SiO ₂	37.05	37.42	37.79	37.31
TiO ₂	0.09	0.13	0.13	0.08
Al ₂ O ₃	25.23	24.96	25.21	24.79
Fe ₂ O ₃	2.00	1.43	1.09	1.76
FeO	1.71	2.02	2.13	1.79
MnO	0.27	0.50	0.46	0.37
MgO	3.14	3.35	3.09	3.07
CaO	22.94	22.45	23.21	23.11
Na ₂ O		0.01		0.01
K ₂ O		<u>0.05</u>		
Total	92.43	92.32	93.11	92.29
Structural formulae based on 24.5 oxygens and 16 cations				
Si	5.971	6.033	6.043	6.026
Al	<u>.029</u>			
	6.000	6.033	6.043	6.026
Al	<u>4.000</u>	<u>4.000</u>	<u>4.000</u>	<u>4.000</u>
	4.000	4.000	4.000	4.000
Al	.763	.742	.751	.718
Fe ³⁺	.243	.173	.131	.213
Ti	.010	.016	.016	.010
Mg	.754	.805	.736	.739
Fe ²⁺	.230	.264	.284	.242
Mn			<u>.072</u>	<u>.051</u>
	2.000	2.000	1.990	1.973
Fe ²⁺		.008		
Mn	.037	.068		
Ca	3.961	3.878	3.976	3.999
Na		.003		.003
K		<u>.010</u>		
	3.998	3.967	3.976	4.002
XMg [*]	.614	.610	.607	.593
XFe ^{3+*}	.048	.035	.027	.043
XMg [#]	.738	.703	.674	.716
Al	.796	.791	.805	.798
Mg	.125	.134	.125	.125
Fe	.078	.074	.070	.077

* XMg = Mg / (Mg + Fe²⁺ + Mn)** XFe³⁺ = Fe³⁺ / (Fe³⁺ + Al)# Mg = Mg / (Mg + Fe²⁺ + Mn)

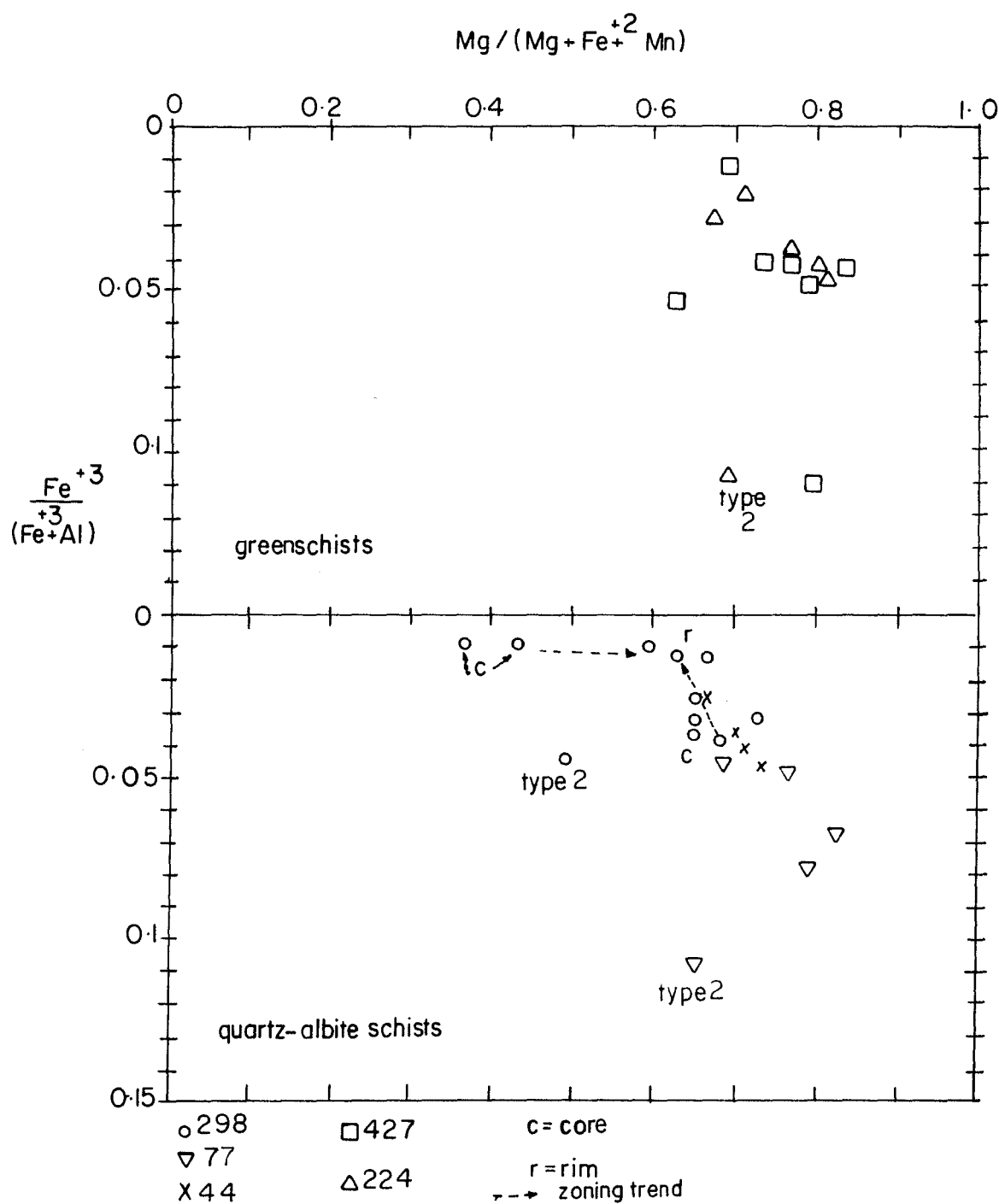


Figure 26. Normalized microprobe analyses of pumpellyite in terms of $\text{Mg} / (\text{Mg} + \text{Fe}^{2+} + \text{Mn})$ vs. $\text{Fe}^{3+} / (\text{Fe}^{3+} + \text{Al})$. The top diagram illustrates greenschist analyses while the lower diagram illustrates quartz-albite schist analyses.

suggests that this pumpellyite may have grown as hollow-ended crystals as previously described. The zoning trend indicated by microprobe analyses 298-4 and 298-5 in another crystal could also be explained by pumpellyite growing as hollow-ended crystals.

The presence of two types of pumpellyite within a single thin section is a disequilibrium feature. The more strongly colored ferric pumpellyites are interpreted to be incompletely recrystallized earlier-formed crystals, while the colorless subhedral and euhedral variety were presumably in equilibrium with the matrix mineral assemblage. This disequilibrium feature, along with the lack of volume equilibration of all pumpellyite, is similar to the textural and chemical relations found in epidotes.

Actinolite-Hornblende

Thin section description. Only two samples analyzed by microprobe, 77 and 224B contain actinolite. In sample 77 actinolite typically appears as individual prisms, needles, and prismatic end sections within the poorly developed second-phase foliation. The average grain size of the actinolite is .06 mm.x .175 mm. Actinolite also occurs in sample 77 as intergrown aggregates. In sample 224B actinolite is interlocked with other actinolite or with chlorite, and defines the foliation. Some of the actinolite-chlorite foliation is clearly first phase and is folded by tight second-phase folds. In other areas of the thin section actinolite is aligned parallel to second-phase axial plane foliation. Some of this actinolite is coarser-grained than the actinolite in the first-phase foliation.

The actinolite has well developed amphibole cleavage and is biaxial negative with a 2V of about 80 degrees. Actinolite is colorless, extinction angle ZAc of about 11 degrees, and has positive elongation.

One grain of relict detrital actinolitic hornblende was analyzed by electron microprobe. This grain is light-greenish brown to brown with a ZAc of about 9 degrees. The crystal is partially disaggregated and has a very thin actinolite rim around it.

Chemistry. All amphibole analyses (Table 9) have been recalculated on an anhydrous basis assuming 23 oxygens per half unit cell. An attempt to determine the minimum and maximum crystal chemically reasonable amounts of Fe^{3+} has been done by normalization methods of Robinson et al. (1982). In some cases when microprobe analyses were normalized to 23 oxygens and all iron was assumed to be ferrous a reasonable structural formula could be written and this is the minimum Fe^{3+} determination. Each analysis was then normalized by the following cation assignments: 1) 15 cations and 23 oxygens; 2) 13 cations excluding Na, Ca, and K; 3) 15 cations excluding Na and K (excludes Ca from the A site); 4) 15 cations excluding K (excludes Na from the A site). If a reasonable formula could be written from one of these

Table 9. Electron microprobe analyses of amphibole. See text for discussion about cation assignment.

Number	<u>44-1</u>	<u>224-1</u>	<u>224-2</u>	<u>224-3</u>	<u>224-4</u>	<u>77-1</u>	<u>77-2</u>	<u>77-3</u>	<u>77-4</u>								
SiO ₂	50.31	54.58	53.50	51.68	51.66	54.48	54.60	54.30	53.30								
TiO ₂	0.79	0.10	0.05	0.08	0.07	0.06	0.11	0.08	0.06								
Al ₂ O ₃	4.94	0.75	1.30	2.45	2.67	0.50	0.62	0.67	0.70								
FeO	12.44	14.34	14.61	15.11	15.47	15.43	16.06	16.70	17.16								
MnO	0.23	0.27	0.31	0.38	0.33	0.35	0.33	0.36	0.30								
MgO	15.48	14.68	14.26	13.52	13.28	14.61	13.76	13.44	12.96								
CaO	12.08	12.61	12.47	12.18	12.07	11.81	12.74	12.54	12.36								
Na ₂ O	0.01	0.30	0.46	0.70	0.89	0.10	0.03	0.07	0.16								
K ₂ O	<u>0.37</u>	<u>0.03</u>	<u>0.05</u>	<u>0.11</u>	<u>0.12</u>	<u>0.03</u>	<u>0.04</u>	<u>0.04</u>	<u>0.04</u>								
Total	96.65	97.66	97.01	96.21	96.56	97.37	98.29	98.20	97.04								
Structural formulae based on 23 oxygens. Cation assignment																	
discussed in text																	
Si	7.301	7.917	7.915	7.840	7.831	7.682	7.657	7.664	7.643	7.947	7.939	7.929	7.926	7.918	7.906	7.909	7.889
Al	<u>0.699</u> 8.000	<u>0.083</u> 8.000	<u>0.085</u> 8.000	<u>0.160</u> 8.000	<u>0.169</u> 8.000	<u>0.318</u> 8.000	<u>0.343</u> 8.000	<u>0.336</u> 8.000	<u>0.357</u> 8.000	<u>0.053</u> 8.000	<u>0.061</u> 8.000	<u>0.071</u> 8.000	<u>0.074</u> 8.000	<u>0.082</u> 8.000	<u>0.094</u> 8.000	<u>0.091</u> 8.000	<u>0.111</u> 8.000
Al	0.146	0.045	0.043	0.065	0.056	0.111	0.085	0.131	0.110	0.033	0.025	0.035	0.032	0.033	0.021	0.031	0.011
Ti	0.086	0.011	0.011	0.006	0.006	0.009	0.009	0.008	0.008	0.007	0.007	0.012	0.012	0.009	0.009	0.007	0.007
Fe ³⁺	0.315		0.011		0.050		0.150		0.127		0.044		0.019		0.067		0.111
Mg	<u>1.453</u> 2.000	<u>1.944</u> 2.000	<u>1.935</u> 2.000	<u>1.929</u> 2.000	<u>1.888</u> 2.000	<u>1.880</u> 2.000	<u>1.756</u> 2.000	<u>1.861</u> 2.000	<u>1.755</u> 2.000	<u>1.960</u> 2.000	<u>1.924</u> 2.000	<u>1.953</u> 2.000	<u>1.937</u> 2.000	<u>1.958</u> 2.000	<u>1.903</u> 2.000	<u>1.962</u> 2.000	<u>1.871</u> 2.000
Mg	1.896	1.230	1.238	1.186	1.223	1.116	1.230	1.076	1.174	1.216	1.249	1.025	1.040	0.963	1.014	0.904	0.988
Fe ²⁺	1.104	1.740	1.729	1.791	1.739	1.878	1.722	1.919	1.787	1.784	1.751	1.950	1.930	2.036	1.966	2.090	1.974
Mn		<u>0.030</u>	<u>0.033</u>	<u>0.023</u>	<u>0.038</u>	<u>0.006</u>	<u>0.048</u>	<u>0.005</u>	<u>0.039</u>			<u>0.025</u>	<u>0.030</u>	<u>0.001</u>	<u>0.020</u>	<u>0.006</u>	<u>0.038</u>
	3.000	3.000	3.000	3.000	3.000	3.000	3.000	3.000	3.000	3.000	3.000	3.000	3.000	3.000	3.000	3.000	3.000
Fe ²⁺	0.091									0.098	0.085						
Mn	0.028	0.003		0.015		0.042		0.034		0.043	0.043	0.016	0.011	0.043	0.024	0.032	
Ca	1.878	1.960	1.960	1.958	1.956	1.940	1.934	1.919	1.914	1.846	1.844	1.982	1.981	1.959	1.956	1.965	1.960
Na	<u>0.003</u> 2.000	<u>0.037</u> 2.000	<u>0.040</u> 2.000	<u>0.027</u> 2.000	<u>0.044</u> 2.000	<u>0.018</u> 2.000	<u>0.066</u> 2.000	<u>0.047</u> 2.000	<u>0.086</u> 2.000	<u>0.013</u> 2.000	<u>0.028</u> 2.000	<u>0.002</u> 2.000	<u>0.008</u> 2.000		<u>0.020</u> 2.000	<u>0.003</u> 2.000	<u>0.040</u> 2.000
Na		0.047	0.044	0.104	0.087	0.184	0.135	0.209	0.169	0.015		0.006		0.020		0.043	0.006
K	<u>0.068</u> 0.068	<u>0.006</u> 0.053	<u>0.006</u> 0.050	<u>0.009</u> 0.113	<u>0.009</u> 0.096	<u>0.021</u> 0.205	<u>0.021</u> 0.156	<u>0.023</u> 0.232	<u>0.023</u> 0.192	<u>0.006</u> 0.021	<u>0.006</u> 0.006	<u>0.007</u> 0.013	<u>0.007</u> 0.007	<u>0.007</u> 0.027	<u>0.007</u> 0.007	<u>0.008</u> 0.051	<u>0.008</u> 0.014
XMg [*]	.732	.642	.643	.630	.636	.609	.628	.600	.616	.622	.628	.599	.602	.584	.592	.574	.586
XFe ^{**}	.271		.079		.182		.259		.213		.338		.152		.368		.476

$$* \text{ XMg} = \frac{\text{Mg}}{\text{Mg} + \text{Mn} + \text{Fe}^{2+}}$$

$$** \text{ XFe} = \frac{\text{Fe}^{3+}}{\text{Al} + \text{Fe}^{3+}}$$

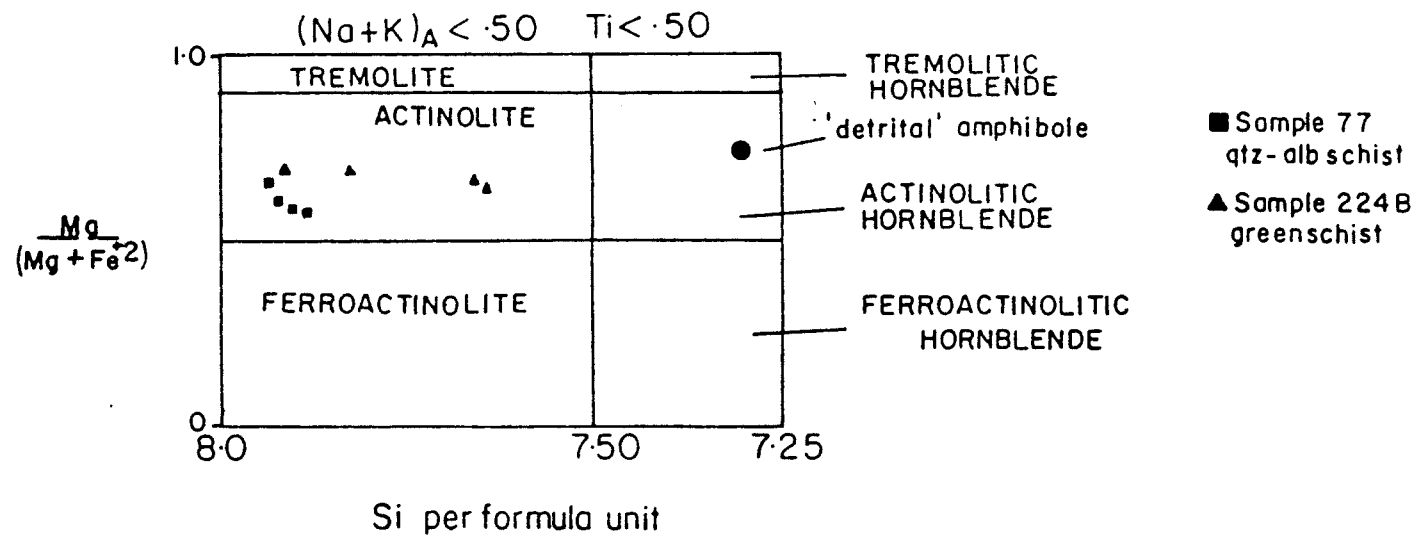


Figure 27. Actinolite analyses plotted in terms of $\text{Mg}/(\text{Mg} + \text{Fe}^{2+})$ and Si per formulae unit. From Leake (1978).

normalizations the formula is listed in Table 9. For microprobe analyses 77-1, 77-2, 77-3, and 44-1 15 cations excluding K resulted in the most reasonable structural formula. For analyses 77-4, and all analyses from sample 224B, 13 cations excluding Na, Ca, and K resulted in the most reasonable formula. For samples 77 and 224B the maximum amount of ferric iron determined is small. For sample 77, $\text{Fe}^{2+}/(\text{Fe}^{2+}+\text{Fe}^{3+}) = .947$ to $.990$. For sample 224B, $\text{Fe}^{2+}/(\text{Fe}^{2+}+\text{Fe}^{3+}) = .920$ to $.994$, and for sample 44, $\text{Fe}^{2+}/(\text{Fe}^{2+}+\text{Fe}^{3+}) = .791$. Table 9 has the analyses listed in terms of decreasing $\text{Mg}/(\text{Mg}+\text{Fe}^{2+}+\text{Mn})$ and this corresponds to core vs. rim analyses. Amphiboles in metamorphosed volcanogenic sediments are capable of many substitutions depending on metamorphic grade, metamorphic facies, and bulk composition (Laird et al., 1980; Robinson et al., 1982). In this study I was particularly interested in the glaucophane substitution $2\text{Ca}(\text{M4}) + 2\text{Mg}(\text{VI}) = 2\text{Na}(\text{M4}) + 2\text{Al}(\text{VI})$. Microprobe analyses reveal that the amount of substitution toward other amphiboles including glaucophane is small. In sample 77 the variation is mostly just in Mg/Fe ratio. In sample 224B (Figure 27) rim compositions have a modest amount of Al and Na compared with the cores. Figure 27 (Leake 1978) illustrates the different Si and Al content of the detrital amphibole in sample 44, but the analysis in Table 9 shows very low Na that may be due to analytical error.

Garnet

Thin section description. Garnet occurs as subhedral to anhedral crystals that are from 0.01mm up to 0.125 mm in diameter. Some garnets have well developed euhedral cross sections. Smaller garnets tend to be more anhedral and have rounded grain boundaries. Some of the largest garnets are more anhedral and appear cracked, while one is even fragmented. Garnet is colorless in thin section, and both isotropic and anisotropic varieties occur. Concentric isotropic and anisotropic banding is visible in some garnets. Garnet occurs within the compositional layering defined by white mica, epidote, chlorite, calcite, quartz, and sphene, but also as discrete grains within quartz-albite-calcite layers. Almost every observed garnet has inclusions, most commonly of epidote.

Chemistry. Selected garnet microprobe analyses are presented in Table 10. The microprobe analyses are recalculated on the basis of 8 cations and 12 oxygens per structural formula. Fe^{3+} was calculated to balance the 12 oxygen anion charge. For all but the core analysis the amount of Fe^{3+} determined is small. The analyses are separated into three groups corresponding to core, interior, and rim analyses. The core analysis has a much higher Mn content than the interiors or rims (48% spessartine at the core as opposed to 34.5-36% spessartine at the rims. Also, cores have more calculated ferric iron). Figure 28 illustrates core, interior, and rim analyses and has been constructed to show the variation from core to rims. The distinction between rims and interiors was a visual estimate of where the microprobe beam hit the grain. The overlap in analyses indicates error in the visual estimate due to the fine grain size. In general the interiors and rims are also

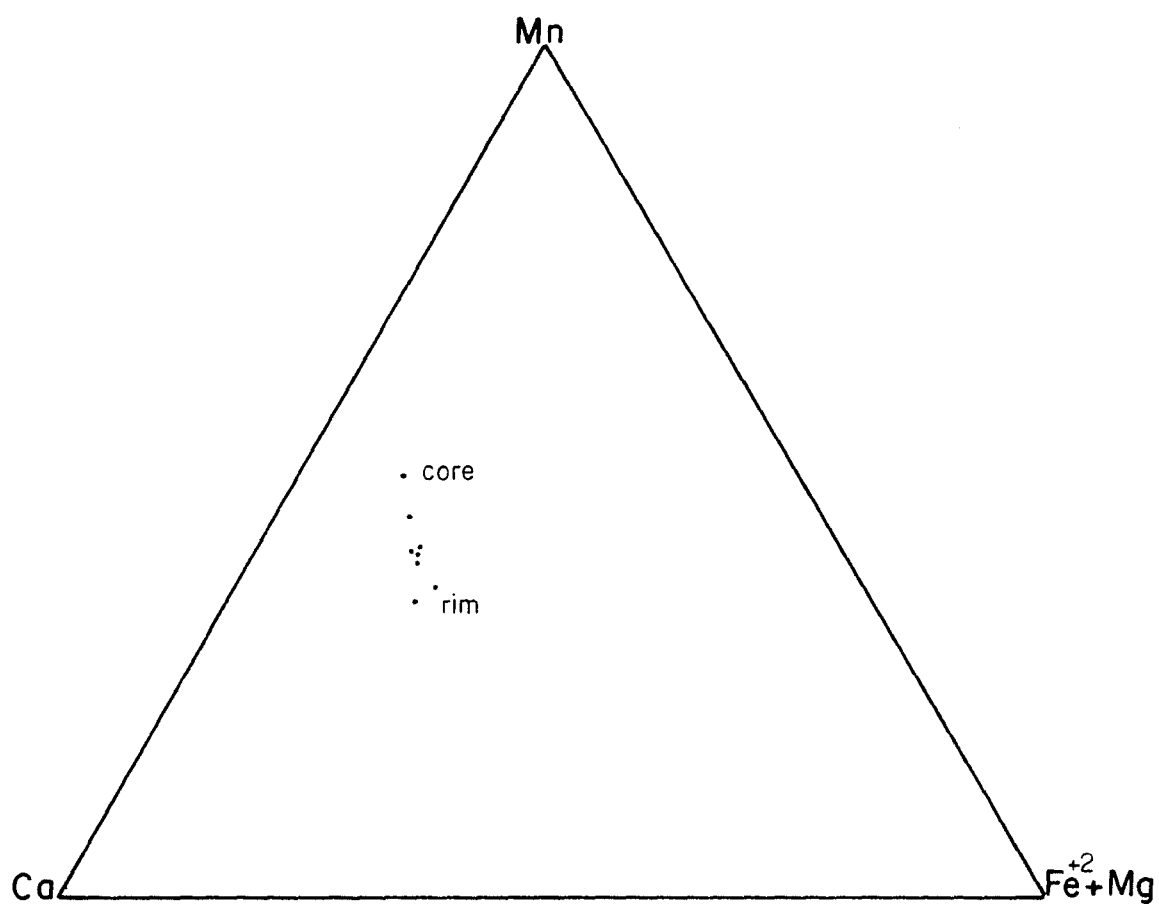


Figure 28. Garnet analyses from sample 210 in terms of Mn- Ca - Fe²⁺+Mg.

enriched in almandine component (11.3% almandine in the core analysis compared with 12.9% to 19.6% almandine component in the interiors and rims).

Albite

Thin section description. Albite occurs in two distinct habits in all samples. Type 1 albite occurs as pseudomorphs as much as 2 mm in diameter of original more calcic plagioclase. This type of albite has sutured grain boundaries, and a cloudy appearance due to the presence of hundreds of individual and aggregate grains of pumpellyite and/or epidote. Type 2 albite occurs as smaller crystals with mosaic articulation. Albite is identified in thin section by its low relief compared with quartz, positive optic sign, and $2V=80$ to 87 degrees. It occurs as both twinned and untwinned crystals and is colorless.

Type 1 albite has been described in metamorphic rocks by Coombs et al. (1970); Kuniyoshi and Liou (1976); and Coombs et al. (1976); and in rocks altered and metasomatized by Na-rich fluids by Amstutz (1968); and Bamba (1974).

Chemistry. Table 11 lists selected microprobe analyses of albite. The analyses are recalculated on the basis of 8 oxygens in the structural formula. The microprobe analyses show almost no deviation from ideal albite. No detectable composition gaps, or compositional zoning are recorded. Figure 29 is a plot of albite compositions on a portion of the feldspar plane.

Sphene

Thin section description. Sphene occurs as high relief crystals 0.01mm to 0.5 mm in diameter, that are colorless to reddish brown, and have mosaic articulation. Sphene also occurs as aggregates which have rounded grain boundaries, and always surround ilmenite. Sphene has a biaxial positive optic sign, birefringence equal to 0.15, and dispersion $r > v$. Some of the sphene has lamellar twins.

Chemistry. Sphene analyses are listed in Table 12. Sphene analyses from Chatham Island schists are similar in composition to sphene analyses from other pumpellyite-actinolite facies rocks (Coombs et al., 1976; Kawachi, 1975). Figure 30 is a plot of sphene analyses from quartz-albite schists and greenschist along with sphene analyses from pumpellyite-actinolite schists from Loeche, Switzerland. Sphenes in greenschists are significantly more aluminous than sphenes in quartz-albite schists. Comparison of the protoliths of quartz-albite schists with those of greenschists suggests a reason for this composition difference. Greenschists were mafic tuffs that probably contained significant calcic plagioclase whereas quartz-albite schists were more felsic tuffs that typically contain andesine-oligoclase (Barker et al., 1979). Breakdown of calcic plagioclase during low grade metamorphism to

Table 11. Electron microprobe analyses of albite. Structural formulae based on 8 oxygens.

Number	<u>44</u>	<u>77</u>	<u>77</u>	<u>77</u>	<u>298</u>	<u>224</u>	<u>427</u>	<u>427</u>	<u>210</u>
SiO ₂	68.73	68.93	68.83	68.83	69.55	69.19	68.63	69.49	69.27
Al ₂ O ₃	20.25	20.19	19.10	20.04	19.56	20.20	20.04	19.82	19.76
CaO	0.04	0.16	0.11	0.03	0.02	0.00	0.19	0.02	0.09
Na ₂ O	11.83	11.78	11.86	11.79	11.98	11.89	11.86	11.76	11.82
K ₂ O	<u>0.00</u>	<u>0.04</u>	<u>0.01</u>	<u>0.01</u>	<u>0.02</u>	<u>0.00</u>	<u>0.01</u>	<u>0.05</u>	<u>0.04</u>
Total	100.85	101.10	99.91	101.70	101.13	101.28	100.63	101.14	100.98
Si	2.976	2.978	3.008	2.984	3.002	2.982	2.979	2.997	2.995
Al	<u>1.033</u>	<u>1.028</u>	<u>.984</u>	<u>1.024</u>	<u>.995</u>	<u>1.026</u>	<u>1.025</u>	<u>1.007</u>	<u>1.007</u>
	4.009	4.006	3.992	4.008	3.997	4.008	4.004	4.004	4.002
Ca	.002	.007	.005	.001	.001		.009	.001	.004
Na	.993	.987	1.005	.991	1.003	.994	.990	.983	.991
K	<u>.002</u>	<u>.002</u>	<u>.001</u>	<u>.001</u>	<u>.001</u>		<u>.001</u>	<u>.003</u>	<u>.002</u>
	.995	.996	1.011	.993	1.005	.994	1.000	.987	.997
Ab	.998	.991	.994	.998	.998	1.000	.990	.996	.994
An	.002	.007	.005	.001	.001		.009	.001	.004
Or		.002	.001	.001	.001		.001	.003	.002

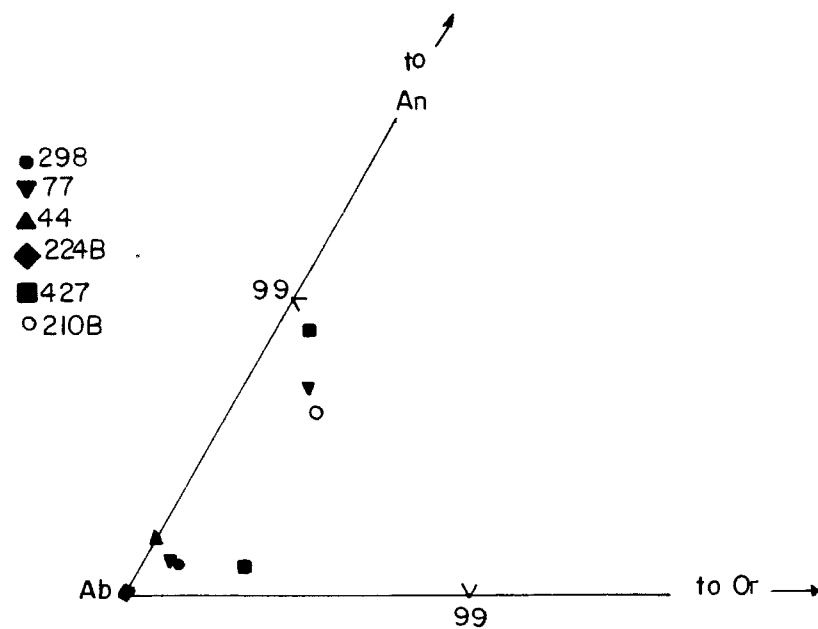


Figure 29. Albite analyses from Chatham Island schists on a portion of the feldspar plane.

Table 12. Electron microprobe analyses of sphene. Structural formulae based on 5 oxygens.

Number	<u>44-1</u>	<u>44-2</u>	<u>77-1</u>	<u>77-2</u>	<u>298-1</u>	<u>298-2</u>	<u>298-3</u>	<u>224B-1</u>	<u>427-1</u>
SiO ₂	29.15	28.65	29.62	29.84	30.67	30.47	30.78	31.36	29.64
TiO ₂	36.50	37.75	37.24	37.70	38.39	38.88	38.13	33.82	34.76
Al ₂ O ₃	2.37	2.15	1.00	1.13	1.42	1.44	1.55	5.24	4.61
FeO	1.16	1.12	1.43	0.95	0.38	0.51	0.48	0.90	1.00
MnO	0.03	0.04	0.13	0.07	0.08	0.06	0.06	0.03	0.02
MgO	0.06	0.05	0.12	0.07	0.12	0.15	0.11	0.04	0.16
CaO	29.21	29.00	29.73	28.33	28.80	28.83	28.37	29.21	28.24
Na ₂ O	<u>0.00</u>	<u>0.00</u>	<u>0.00</u>	<u>0.00</u>	<u>0.00</u>	<u>0.01</u>	<u>0.00</u>	<u>0.00</u>	<u>0.00</u>
Total	98.48	98.76	99.27	98.09	99.86	99.84	100.34	100.60	98.43
Structural formulae based on 5 oxygens									
Si	.976	.955	.989	.986	.993	.988	1.001	1.012	.981
Al	<u>.024</u>	<u>.045</u>	<u>.011</u>	<u>.014</u>	<u>.007</u>	<u>.012</u>			<u>.019</u>
	1.000	1.000	1.000	1.000	1.000	1.000	1.001	1.012	1.000
Al	.069	.039	.032	.030	.047	.043	.059	.199	.161
Ti	.919	.946	.935	.937	.935	.949	.932	.820	.865
Fe	.032	.031	.036	.024	.009	.012	.012	.024	.028
Mg	.003	.002	.006	.003	.006	.007	.005	.002	.008
Mn	<u>.001</u>	<u>.001</u>	<u>.003</u>	<u>.001</u>	<u>.002</u>	<u>.001</u>	<u>.001</u>	<u>.001</u>	<u>.001</u>
	1.024	1.019	1.012	.995	.999	1.012	1.009	1.046	1.063
Ca	1.032	1.036	.992	1.004	1.000	.985	.989	1.010	1.001
Na						<u>.002</u>			
	<u>1.032</u>	<u>1.036</u>	<u>.992</u>	<u>1.004</u>	<u>1.000</u>	<u>.987</u>	<u>.989</u>	<u>1.010</u>	<u>1.001</u>

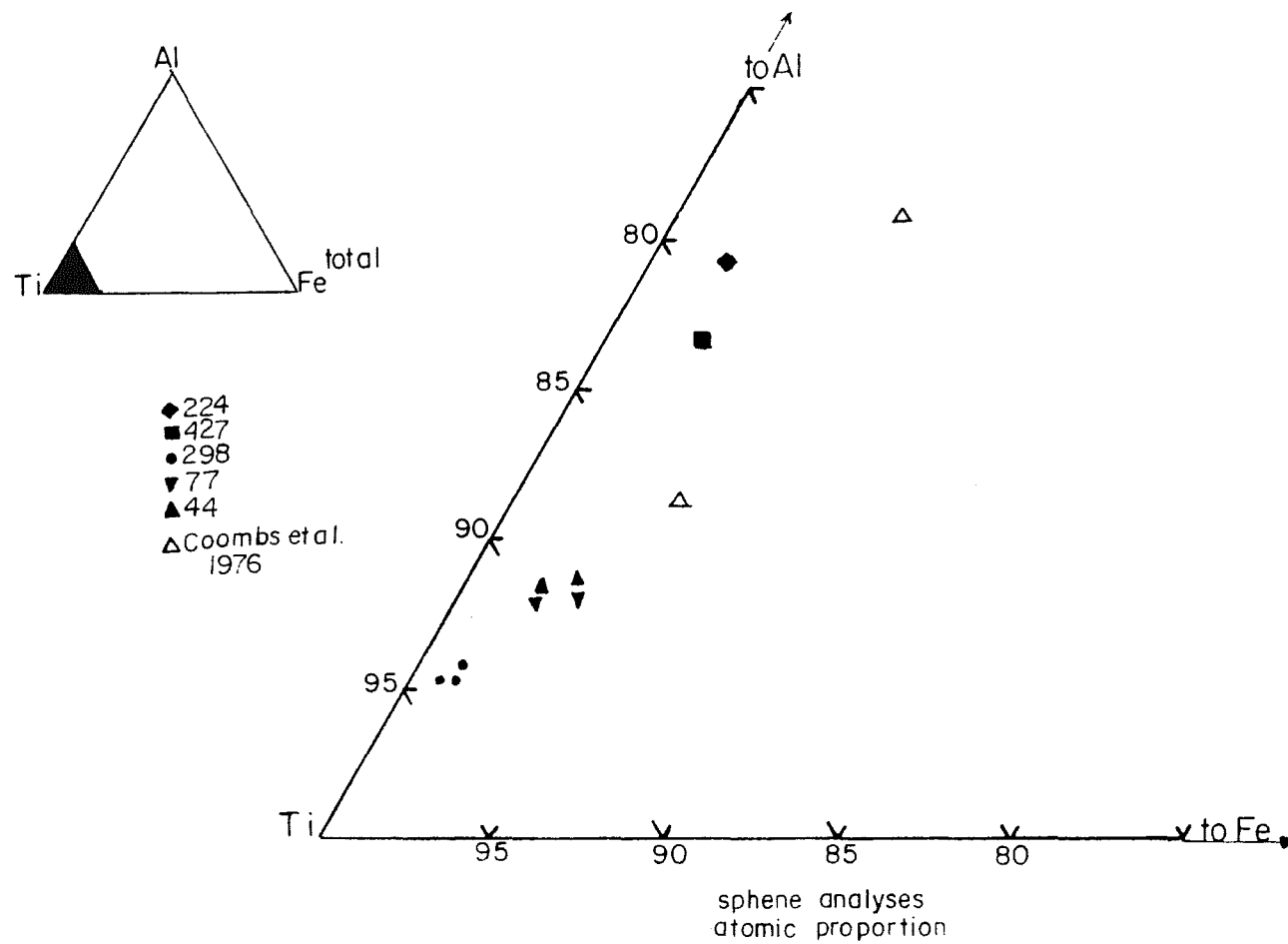


Figure 30. Sphene analyses from Chatham Island schists plotted in terms of Al-Ti-Fe_{total}.

form albite in rocks with higher normative anorthite will produce more aluminous sphene and smaller amounts of albite, whereas in more albitic bulk compositions there will be less Al from the smaller anorthite component to go into aluminous sphene. Sphene can deviate from the ideal sphene formulae by the substitutions $TiO = (AlOH)$ (Hollocher, 1981), $TiO = AlF$, and $Al + (OH, F, \text{ or } Cl) = Ti + O$ (Shearer, 1984).

Calcite

Thin section description. Calcite occurs in greenschists as a minor phase. It occurs as subhedral and anhedral crystals with mosaic and sutured articulation, and in some cases is interstitial. In the garnet-bearing schist 210B calcite is much more abundant and is subhedral to euhedral.

Chemistry. Averaged microprobe analyses of calcite from greenschists 427, and 224B are listed in Table 13. Greenschist carbonate analyses varied little and are not listed individually in the table. The calcite in sample 210B contains more Mn, Mg, and Fe, 1.5 to 2.4 mole % rhodochrosite component, 0.7 to 1.5 mole % magnesite, and 0.4 to 0.9 mole % siderite.

Quartz

Quartz occurs in all the thin sections. Grain diameter of quartz differs among the thin sections but is in the range 0.25 to 0.5 mm. In quartz-albite schist samples 44 and 77 there is an abundance of larger-sized relict quartz phenocrysts which are flattened in the plane of the foliation by mechanical crushing and recrystallization. In hand specimen these sheared quartz grains have a blue color indicating they may be relict volcanic quartz phenocrysts. These quartz grains are anhedral and have sutured articulation. Commonly recrystallized finer-grained metamorphic quartz forms along grain margins. Samples 298 and 427 also contain relict quartz phenocrysts, whereas in sample 224B if they were ever present they have presumably recrystallized completely. In general the metamorphic quartz is finer-grained than the relict quartz phenocrysts and it has mosaic articulation. In sample 298 quartz crystals have sutured grain boundaries and are more anhedral than the other samples and this is probably a result of the third-phase of deformation. In sample 224B quartz is found in the hinge region of minor second phase folds.

Minor Minerals

Apatite and zircon were found in all thin sections analyzed.

Apatite is identified by low birefringence, high relief, and negative elongation, and has a dusty appearance due to small black unidentified inclusions.

Zircon occurs as euhedral and subhedral crystals. Zircon in euhedral grains has square cross sectional forms, gives positive

Table 13. Electron microprobe analyses of calcite, Structural formulae based on 1 cation.

	n=11	n=9									
Number	<u>224B</u>	<u>427</u>	<u>210-1</u>	<u>210-2</u>	<u>210-3</u>	<u>210-4</u>	<u>210-5</u>	<u>210-6</u>	<u>210-7</u>	<u>210-8</u>	<u>210-9</u>
CaO	58.50	58.68	55.13	56.40	55.10	55.95	55.05	56.18	55.79	55.88	56.55
MnO	0.48	0.22	1.66	1.53	1.61	1.46	1.43	1.27	1.09	1.09	1.34
FeO	0.36	0.30	0.66	0.60	0.59	0.55	0.64	0.40	0.27	0.29	0.50
MgO	<u>0.27</u>	<u>0.26</u>	<u>0.04</u>	<u>0.39</u>	<u>0.40</u>	<u>0.32</u>	<u>0.37</u>	<u>0.34</u>	<u>0.24</u>	<u>0.27</u>	<u>0.41</u>
Total	59.61	59.47	57.48	58.20	55.10	55.95	57.49	56.18	55.79	55.88	56.55
Structural formulae based on 1 cation											
Mg	.004	.005	.008	.009	.009	.007	.009	.008	.015	.007	.018
Fe	.006	.005	.009	.007	.008	.007	.009	.005	.007	.004	.006
Mn	.008	.004	.024	.022	.022	.020	.019	.018	.016	.015	.009
Ca	<u>.982</u>	<u>.986</u>	<u>.959</u>	<u>.962</u>	<u>.960</u>	<u>.965</u>	<u>.963</u>	<u>.969</u>	<u>.980</u>	<u>.974</u>	<u>.967</u>
	1.000	1.000	1.000	1.000	1.000	1.000	1.000	1.000	1.000	1.000	1.000
X _{Mn} *	.008	.004	.024	.022	.022	.020	.019	.018	.016	.015	.009

X_{Mn} = Mn / (Mn+Mg+Fe+Ca)

n=number of analyses

uniaxial figures, and is gray to colorless.

Chalcopyrite was identified in sample 224B. It is very fine-grained and anhedral. Hematite rims on interstitial grains are interpreted to be due to weathering.

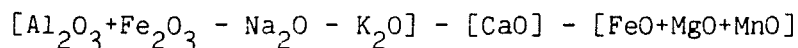
Pyrite was identified in sample 210B. It is very fine-grained and interstitial.

Ilmenite occurs as relict, highly altered, anhedral grains that are always surrounded by sphene.

PHASE RELATIONS

Introduction

The major components needed to describe the chemical relations of phases in metamorphosed volcanogenic sediments from the Chatham Islands are SiO_2 , TiO_2 , Al_2O_3 , Fe_2O_3 , FeO , MnO , MgO , CaO , Na_2O , K_2O , H_2O , and CO_2 . Graphical analysis of the phase relations is complicated because of the large number of components and the chemical variability of the minerals. Combining chemically similar components is an established practice in petrology as is the technique of projecting from components or phases made of these components (Goldschmidt, 1912; Eskola, 1915; Thompson, 1957; Robinson and Jaffe, 1966; Osberg, 1971; Stout, 1975; Harte and Graham, 1975; Laird, 1980; Spear, 1982). Each projection in this thesis provides information about the phase relations in a subset of the chemical system. This is necessary for determination of mineral reactions and for petrogenetic interpretations. Quartz, albite, and sphene are present in all thin sections, and all phase diagrams may be considered as projections from these phases.



Selected microprobe analyses from quartz-albite schists and greenschists are plotted on the ACF diagram in Figure 31. The analyses have been chosen to illustrate the variability of mineral compositions among the samples. Also core-rim data from actinolite are plotted to indicate the compositional variability of individual actinolite crystals. Immediately obvious from the figure is the fact that the analyzed samples contain either the three-phase assemblage epidote-chlorite-pumpellyite or the four-phase assemblage epidote-chlorite-pumpellyite-actinolite. Also important is the increase in Al in actinolite from core to rim, the slight variation of aluminum in chlorite, and the slight variation in pumpellyite composition. The aluminum variation in chlorite is systematic. Sample 298, with the three-phase assemblage lacking actinolite, has chlorite with the most aluminum. Sample 224B and sample 77, with the actinolite-bearing assemblages, have chlorites with less aluminum.

The ACF diagram cannot be used for showing the important

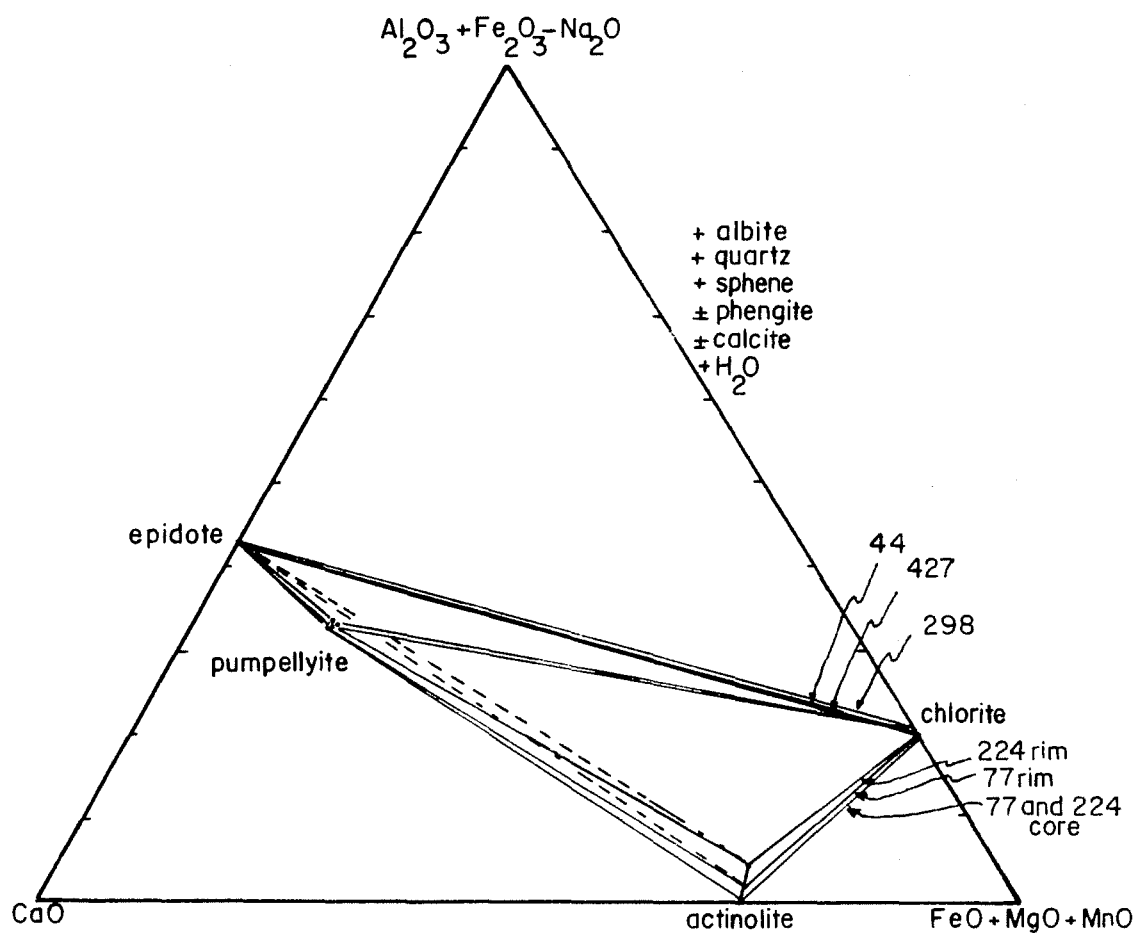


Figure 31. ACF diagram illustrating phase relations for Chatham Island quartz-albite schists and greenschists. Both core and rim analyses from actinolite are illustrated to indicate the increase in Al during crystal growth. Tie lines between epidote and actinolite are left dashed and possible interpretations are discussed in the text.

fractionations of Fe^{3+} and Al, or of Mg and Fe^{2+} . The crossing tie lines of coexisting epidote and actinolite are left dashed and the following possible interpretations of the four-phase assemblages are considered: 1) According to the original metamorphic facies concept of Eskola (1915), crossing tie lines should indicate disequilibrium or equilibrium at the boundary between two different metamorphic facies. 2) Greenwood (1975) suggested that the crossing tie lines can result from the "n-dimensional" tie line problem, where simplification of the chemical system for two-dimensional representation causes neglect of a component or components that are stabilizing important phases. 3) Rumble (1977) and Spear (1982) found that crossing tie lines may be the result of internal control of H_2O with different values of $\mu\text{H}_2\text{O}$ in different samples under the same P and T conditions. This in effect would be different metamorphic facies where the difference would be mainly in $\mu\text{H}_2\text{O}$.

Textural evidence suggests that the more aluminous pumpellyites are stable and are not reacting significantly in the ACF system to produce a change in metamorphic facies. Thus alternative one is not likely. In order to evaluate the remaining alternatives, two projections are used, the epidote projection and the chlorite projection.

Epidote Projection

A geometric approach to evaluate alternative 2 is to change the old set of components into a new set by projecting from phases within the assemblages onto planes or lines related to the ACF diagram. In Figure 32 a projection is made from epidote onto the basal plane of the tetrahedron $[\text{Al} + \text{Fe}^{3+} - (\text{Na} + \text{K})] - [\text{Ca}] - [\text{Fe}^{2+} + \text{Mn}] - [\text{Mg}]$, in order to show the $(\text{Fe}^{2+} + \text{Mn})$ vs. Mg fractionation between the minerals. Figures 33 and 34 illustrate all the chlorite-actinolite-pumpellyite analyses from schist samples. Individual analyses are plotted to show the variation within each sample and a best fit tie line has been drawn between the coexisting phases. Figure 35 is a summary diagram which illustrates the phase relations. These figures illustrate the following points: 1) In general quartz-albite schists have assemblages that are more ferrous than greenschists. 2) The fractionation of Mg and Fe^{2+} between coexisting chlorite and amphibole is such that actinolite is more magnesian than chlorite in both actinolite assemblages. 3) The pumpellyite has a higher Mg/Fe^{2+} ratio than either chlorite or actinolite, although this is dependent on the fact that normalized microprobe data are used. 4) There is considerable overlap in the compositions of type 1 pumpellyites from the different rock compositions. 5) The summary diagram illustrates that pumpellyite-chlorite tie lines of actinolite-free assemblages cut across the tie lines of actinolite-bearing assemblages. The two actinolite-bearing assemblages themselves also show mutually crossing tie lines. Two possible explanations for these crossing tie lines are offered: a) the projection from epidote is "invalid" (Greenwood, 1975) in the sense that epidote composition is too varied between the samples or, b) that the assemblages did not form under the same conditions.

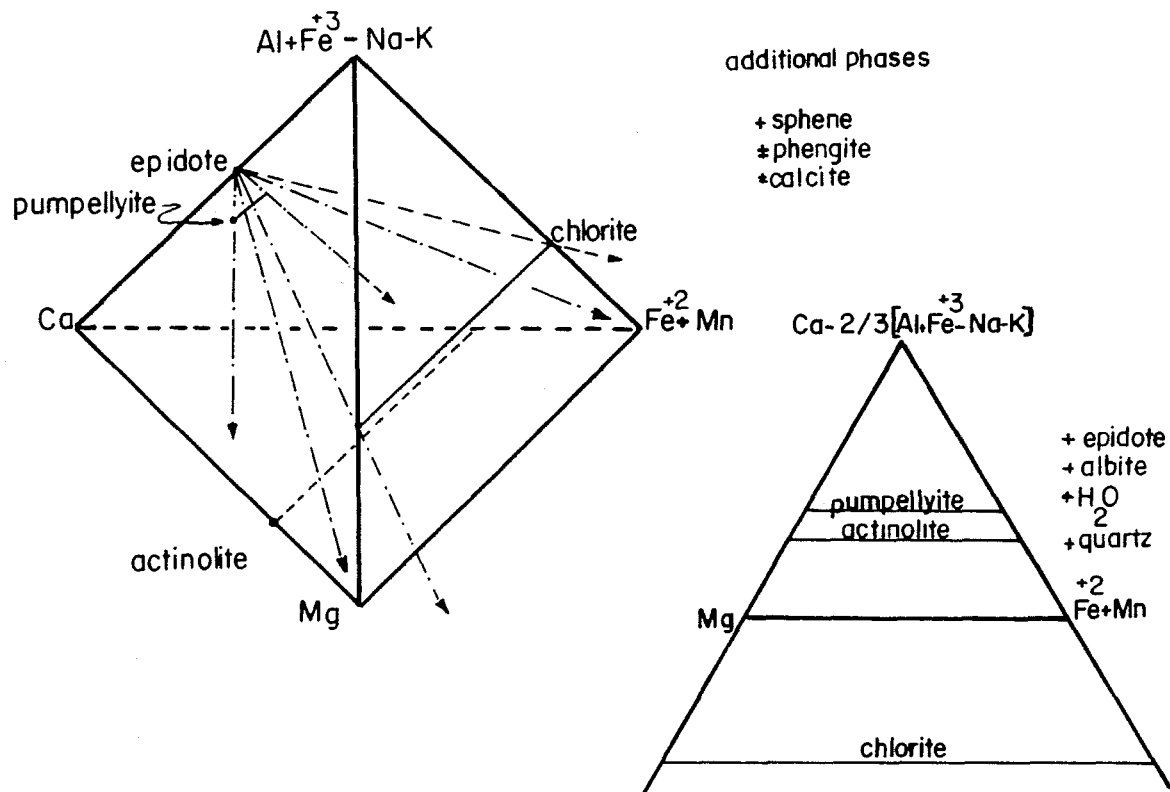


Figure 32. Geometry of the epidote projection. This projection is onto the basal plane of the [Ca] - [Mg] - [Fe²⁺+Mn] - (Al+Fe³⁺-Na-K) tetrahedron.

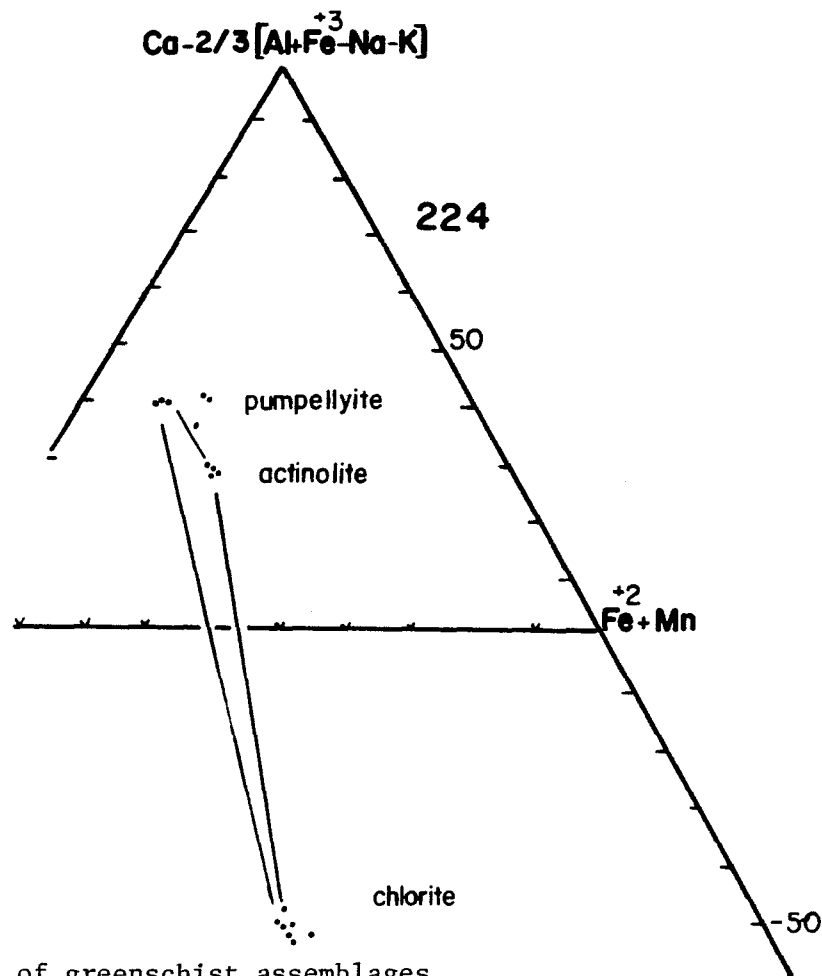
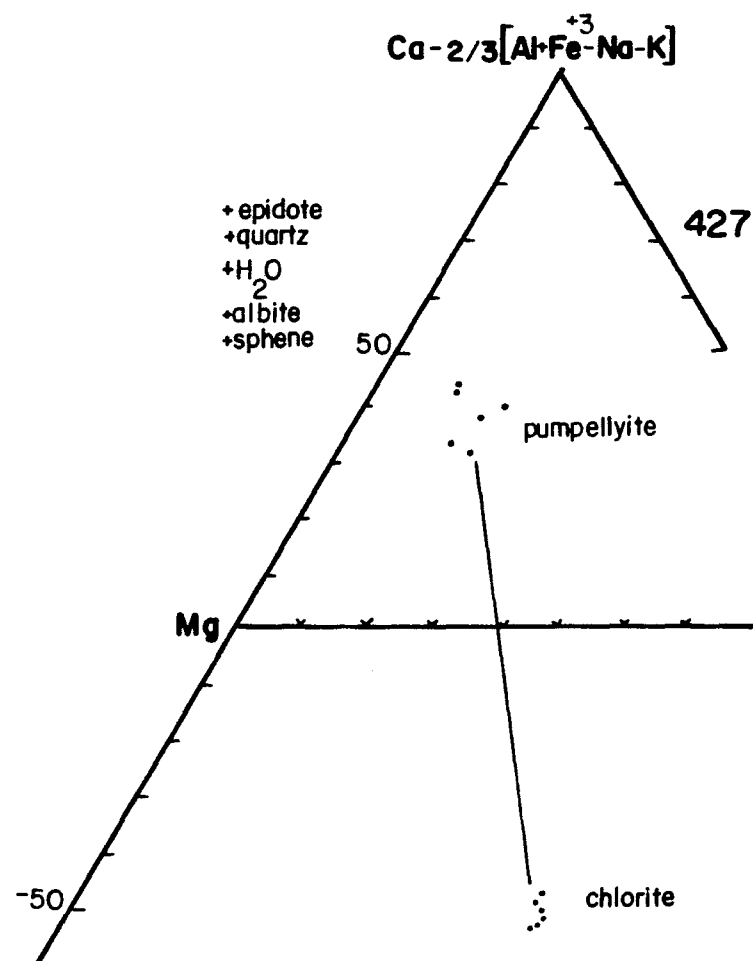


Figure 33. Projected microprobe analyses of greenschist assemblages from epidote illustrating phase relations for the assemblages chlorite-pumpellyite, and chlorite-pumpellyite-actinolite.

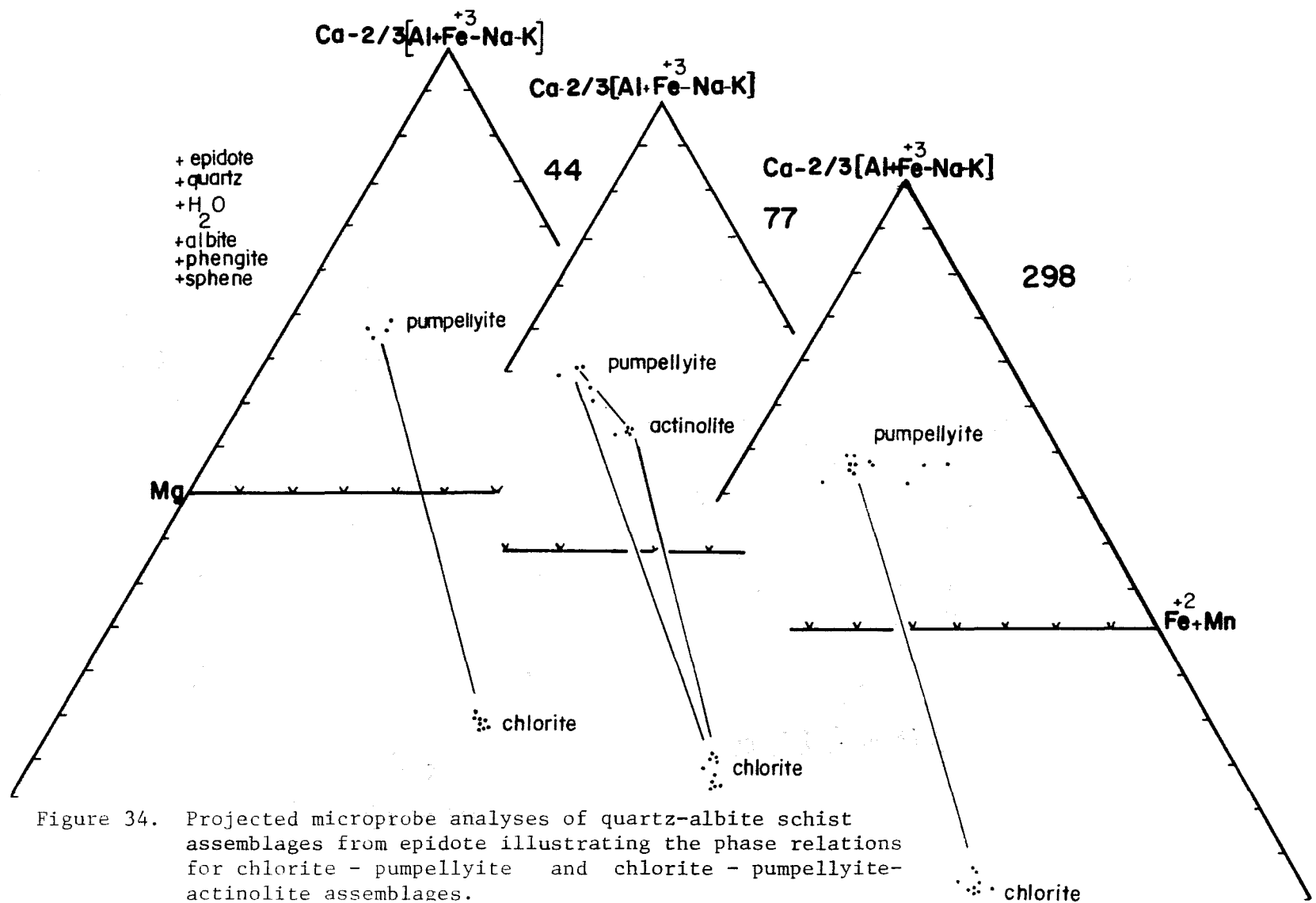


Figure 34. Projected microprobe analyses of quartz-albite schist assemblages from epidote illustrating the phase relations for chlorite - pumpellyite and chlorite - pumpellyite-actinolite assemblages.

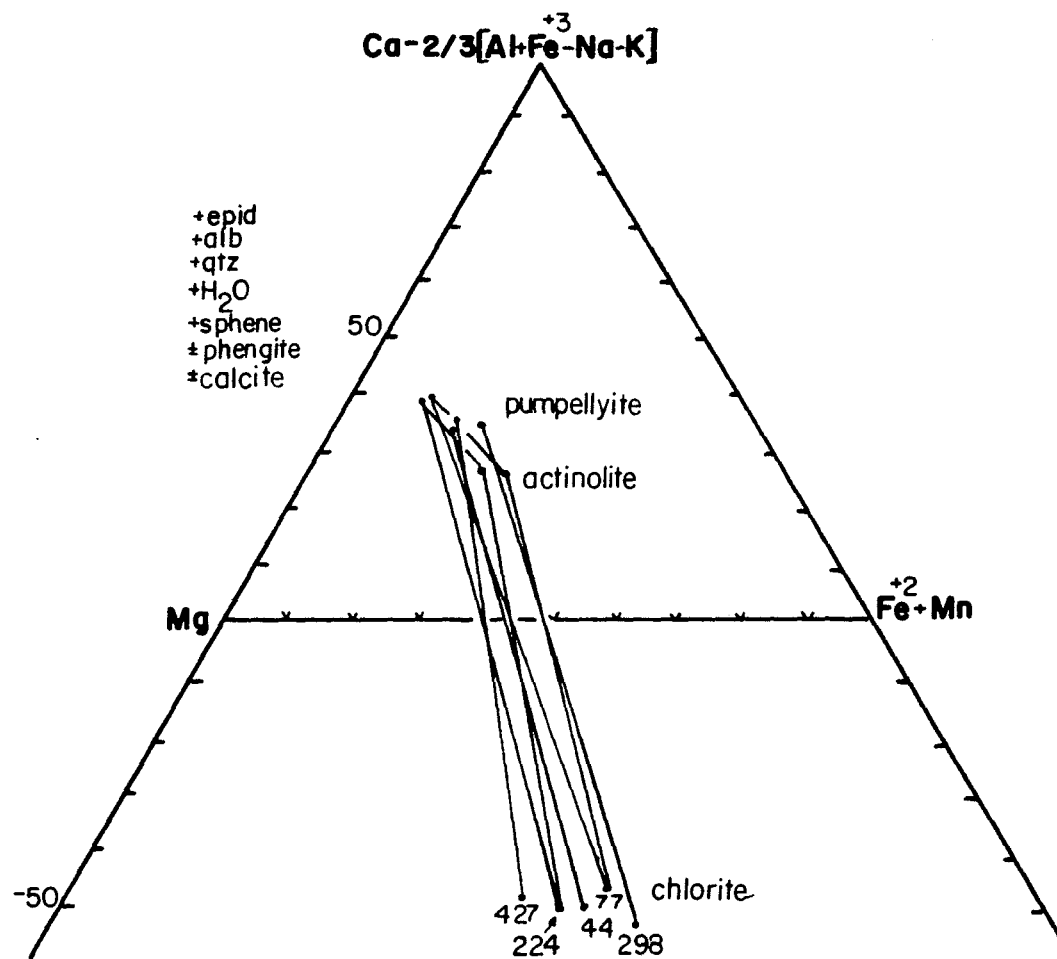


Figure 35. Epidote projection of averaged phase relations from Chatham Island schists.

Chlorite Projection

A projection from constant chlorite composition, similar to Chatham Island chlorite composition, $(\text{Fe}, \text{Mg})_{4.8}\text{Al}_{2.4}\text{Si}_{2.8}\text{O}_{10}(\text{OH})_8$, onto the $\text{Al}_2\text{O}_3 - \text{Fe}_2\text{O}_3 - \text{CaO}$ face of the tetrahedron seen in Figure 36 illustrates the effects that Fe_2O_3 has on the phase relations. Figure 37 is a more practical version of Figure 36, a modification resulting from the transformation of the equilateral triangle of Figure 36 into a right triangle, with the Fe_2O_3 dimension greatly expanded. Figure 37 clearly shows that epidote in actinolite-bearing assemblages contains more ferric iron than epidote in actinolite-free assemblages. This would account for the crossing tie-lines in both the ACF diagram and the epidote projection.

The above analysis of phase relations indicates that the Chatham Island schists consist of the ACF assemblage epidote-chlorite-pumpellyite, of which samples 298, 44, and 427 are examples, or the assemblage pumpellyite-chlorite-actinolite in samples 77 and 224B where epidote is stabilized as an additional phase by the additional component Fe_2O_3 .

Element Partitioning

In this section some of the relative partitioning of various elements between coexisting phases in the different samples is discussed. Element partitioning data can be used for comparison with other pumpellyite-actinolite facies localities and in a general way as a test for equilibrium among the samples considered here. Because all of the minerals are chemically zoned, I have chosen averaged and selected rim analyses for Table 14 which summarizes the data chosen, and for Figures 38, 39 which illustrate the distribution of the elements.

Mg-Fe Partitioning. $(\text{Mg}/\text{Fe}^t)_{\text{act}} / (\text{Mg}/\text{Fe}^t)_{\text{chl}}$ where $(\text{Mg}/\text{Fe}^t) = (\text{XMg}/\text{XFe})$ and $\text{XMg} = \text{Mg}/(\text{Mg} + \text{Fe}^t)$ and $\text{XFe} = (1 - \text{XMg})$, has been used by Kawachi (1975), Coombs et al. (1976) and Moore (1984) to compare relative fractionation of magnesium and iron between coexisting chlorite and actinolite. Much of the variation in $(\text{Mg}/\text{Fe})_{\text{act}} / (\text{Mg}/\text{Fe})_{\text{chl}}$ in low-grade rocks is thought to be caused by the non-ideal mixing in amphibole sites at low temperature; due in part to the occupancy of the M4 site by calcium (Spear, 1982). During progressive metamorphism the fractionation of Fe and Mg between coexisting chlorite and actinolite should decrease (Laird, 1981).

Of the analysed samples from Chatham Island only samples 224B and 77 have actinolite. For averaged compositions the distribution

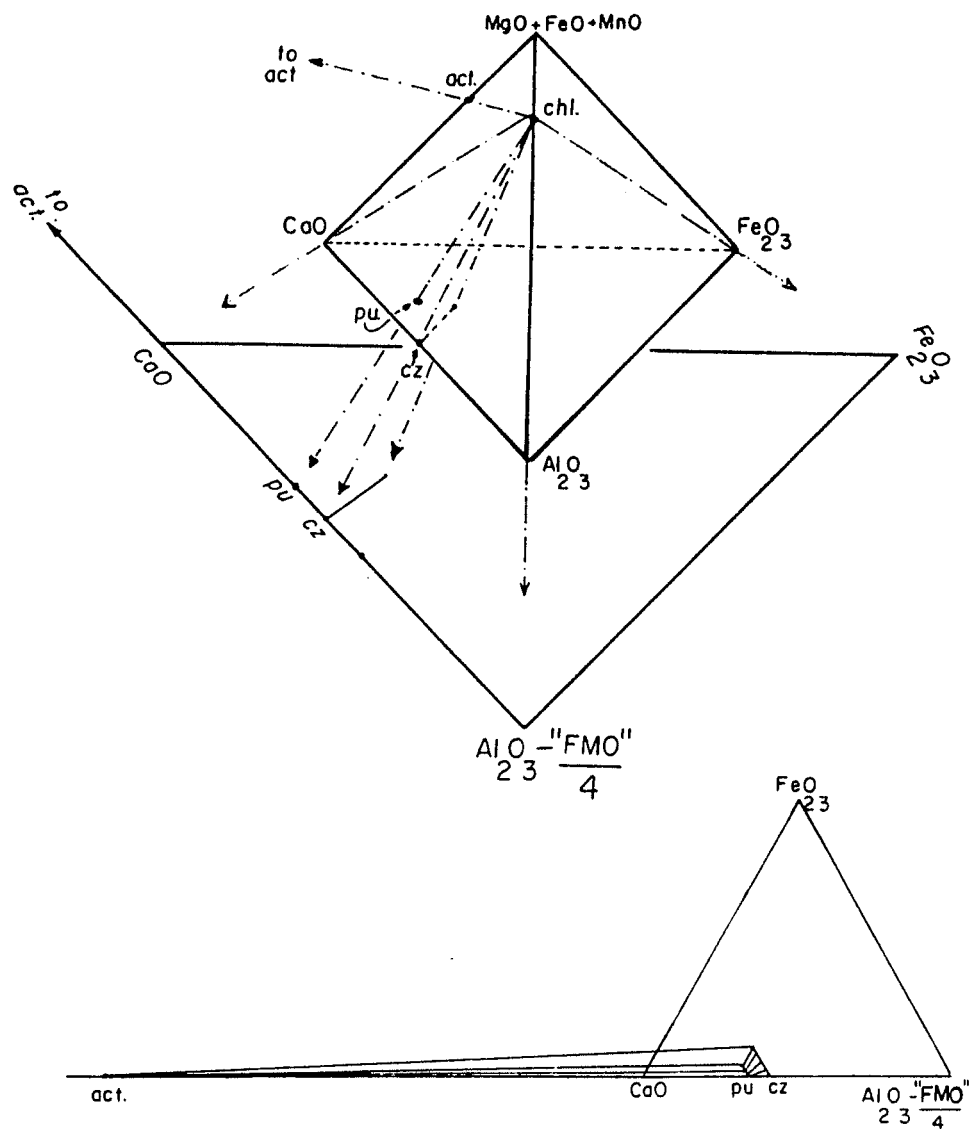


Figure 36. Geometry of the chlorite projection. This projection is from chlorite onto the Fe_2O_3 - Al_2O_3 - CaO plane.

Table 14. $(\text{Mg}/\text{Fe}^{\text{t}})_{\text{act}} / (\text{Mg}/\text{Fe}^{\text{t}})_{\text{chl}}$ and $(\text{Mn}/\text{Mg})_{\text{pump}} / (\text{Mn}/\text{Mg})_{\text{chl}}$.

	XMg	XFe	K _D [*]
sample 224B			
average actinolite	.625	.375	1.76
average chlorite	.486	.514	
rim actinolite	.609	.391	1.71
rim chlorite	.477	.523	
sample 77			
rim actinolite	.578	.422	1.78
rim chlorite	.435	.565	
$^*K_D = \frac{(X_{Mg}^{act})(X_{Fe}^{chl})}{(X_{Mg}^{chl})(X_{Fe}^{act})}$			
	XMn	XMg	K _D ^{**}
sample 298			
pumpellyite	.084	.916	5.30
chlorite	.017	.983	
sample 77			
pumpellyite	.073	.927	3.35
chlorite	.023	.977	
sample 44			
pumpellyite	.075	.925	3.93
chlorite	.020	.980	
sample 224B			
pumpellyite	.043	.957	2.81
chlorite	.016	.984	
sample 427			
pumpellyite	.069	.931	6.10
chlorite	.012	.988	
$^{**}K_D = \frac{(X_{Mn}^{pump})(X_{Mg}^{chl})}{(X_{Mn}^{chl})(X_{Mg}^{pump})}$			

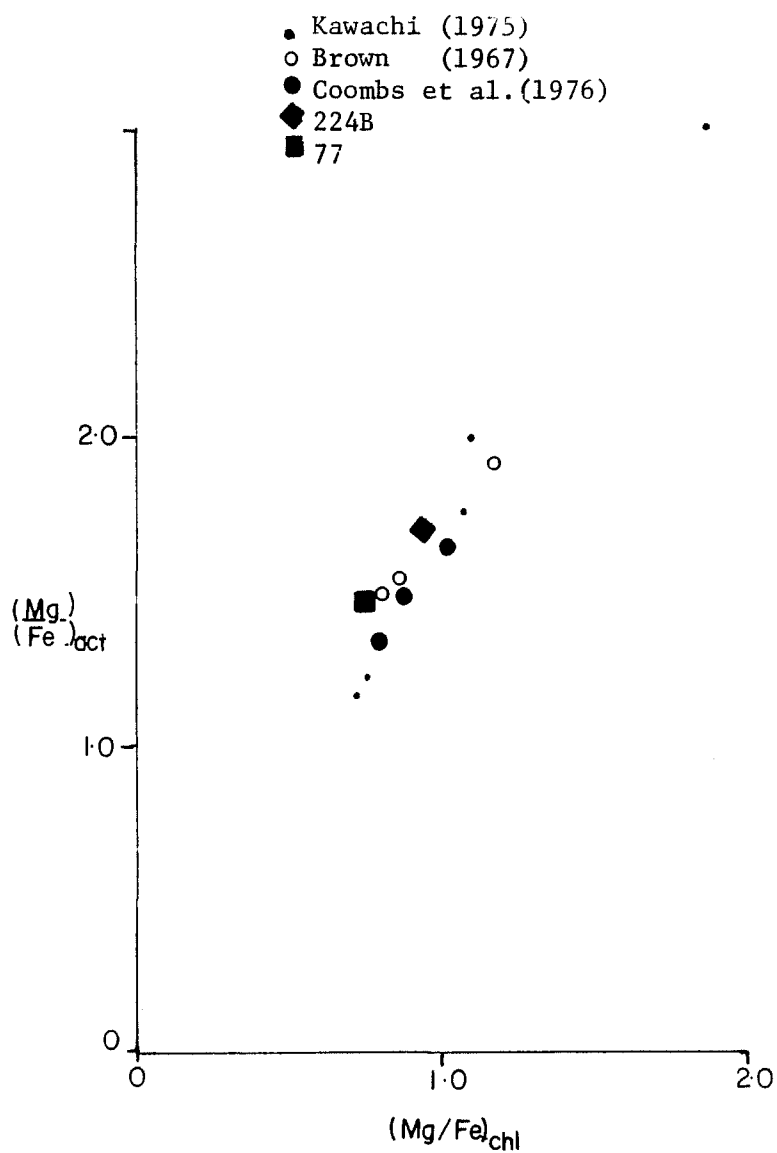


Figure 38. $(Mg/Fe^t)_{act} / (Mg/Fe^t)_{chl}$. Chatham Island data is compared with the data of Brown (1967), Kawachi (1975), and Coombs et al., (1976).

coefficient K_D , calculated from the sample 224B is 1.76 and from sample 77 is 1.78. If only rim chlorite and actinolite data are used, sample 224B gives 1.72, and sample 77 gives 1.75. These values are similar and suggest that the samples are approximately in equilibrium. The values are also similar to those obtained by Kawachi (1975) ($K_D=1.70$) and Coombs et al., (1976) ($K_D=1.72$). Coombs et al. (1976) estimated that the temperature of metamorphism for pumpellyite-actinolite facies schists at Loeche, Switzerland is 270-340°C. This may also be a realistic temperature range for Chatham Island schists.

Mn-Mg Partitioning. Maruyama and Liou (1985) have used manganese and magnesium data from Nakajima et al. (1977), Nakajima (1982), Aiba (1982) and Maruyama and Liou (1985) to distinguish rocks metamorphosed at lower pumpellyite actinolite facies from those metamorphosed at upper pumpellyite-actinolite facies. In particular the $(\text{Mn/Mg})_{\text{pump}} /$

$(\text{Mn/Mg})_{\text{chl}}$ has been shown to vary from 0.9 to 6 in lower pumpellyite-actinolite facies schists and from 7 to 10 in upper pumpellyite-actinolite facies schists, where $(\text{Mn/Mg}) = \text{XMn}/\text{XMg}$ and $\text{XMn} = \text{Mn}/(\text{Mn}+\text{Mg})$ and $\text{XMg} = 1-\text{XMn}$. Chatham Island data range from 2.06 to 6.16 for $(\text{Mn/Mg})_{\text{pump}} / (\text{Mn/Mg})_{\text{chl}}$. It should be pointed out that Mn is a trace

component (>2 wt.%) and is subject to at least 10% error. Assuming that the analyses are correct, this study suggests that Chatham Island schists were metamorphosed under lower pumpellyite-actinolite facies conditions.

MINERAL REACTIONS WITH PUMPELLYITE

In quartz-albite schists and greenschists, the mineral assemblage chlorite-pumpellyite-epidote-actinolite mimics the reaction in the model system $\text{CaO-MgO-Al}_2\text{O}_3 - \text{SiO}_2 - \text{H}_2\text{O}$ where assemblages of the pumpellyite-actinolite facies become greenschist facies assemblages, usually denoted by the disappearance of pumpellyite. In the model system the discontinuous pumpellyite destroying dehydration reaction is:

pumpellyite + chlorite + quartz = tremolite + clinozoisite (or zoisite) + H_2O (Hashimoto, 1972; Kawachi, 1975; Coombs et al., 1976; Nakajima et al., 1977). Real reactions differ from the model system mainly because of the Mg-Fe^{2+} , Fe^{3+} -Al, and FeMgSi-Al_2 exchanges in the minerals that produce continuous reactions in which various substitutions stabilize various product assemblages.

Evidence for such a reaction includes: 1) differences in modal abundances of epidote in actinolite-bearing rocks as opposed to actinolite-free rocks, 2) the zoning of epidote, and 3) the microprobe analyses. This evidence all indicates that in rocks with high Fe_2O_3 , Fe^{3+} -richer pumpellyite was being destroyed and reacting with chlorite to form actinolite, more aluminous epidote, and a more aluminous stable

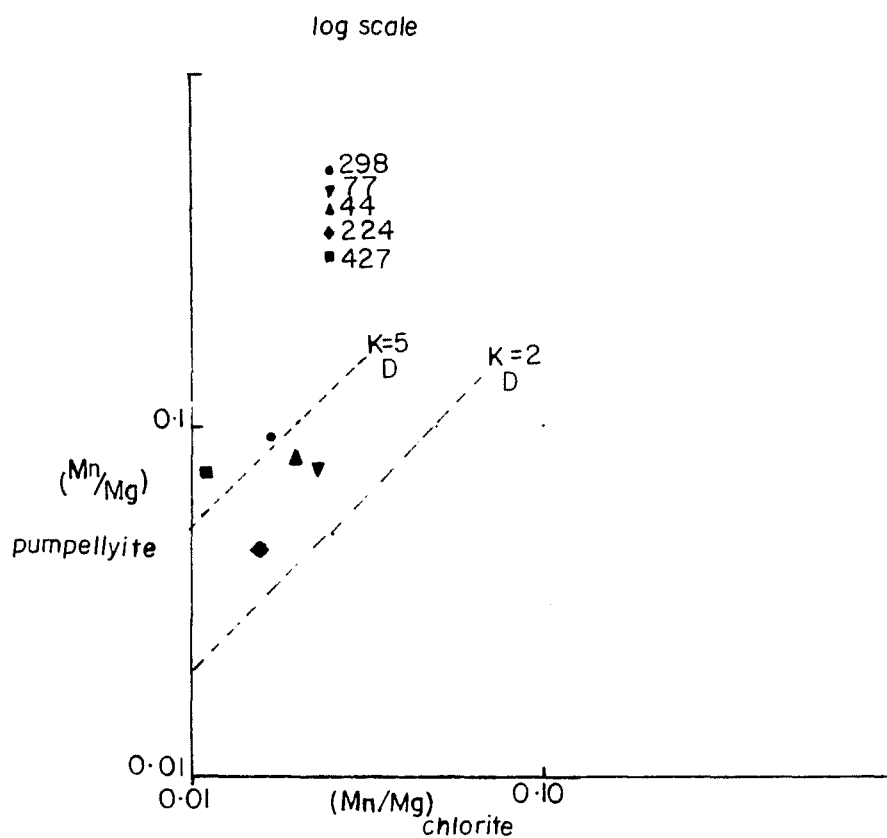


Figure 39. $(Mn/Mg)_{pump} / (Mn/Mg)_{chl}$ for Chatham Island schists. Partitioning suggests that Chatham Island schists are low temperature intermediate to high pressure facies series of the pumpellyite-actinolite facies.

pumpellyite. In the real system this is a continuous reaction of the form:

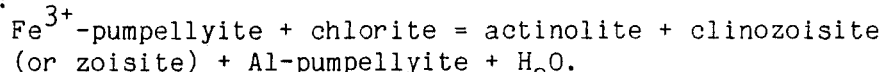


Figure 40 illustrates how this reaction takes place and effects two bulk compositions A and B. The above reaction proceeds to the right with increasing temperature because this side gives off H_2O . Bulk composition A, the more ferric bulk composition, is reached by the reaction first, and as Fe^{3+} -pumpellyite is destroyed, actinolite is produced along with a greater quantity of more aluminous epidote and the remaining pumpellyite becomes more aluminous. Figure 41 illustrates this reaction using data from sample 224B. This figure assumes that core epidote and core actinolite compositions coexisted with type 2 ferric pumpellyite. As the reaction proceeded, type 1 pumpellyite was produced, epidote became more aluminous, and actinolite became more aluminous and slightly more ferric. This reaction could continue until all ferric pumpellyite is destroyed.

Figure 42 is an epidote projection onto the basal plane of the $[\text{Al}+\text{Fe}^{3+}-\text{Na}-\text{K}] - [\text{Ca}] - [\text{Fe}^{2+}+\text{Mn}] - [\text{Mg}]$ tetrahedron. This diagram can be used to illustrate how the three-phase field chlorite-pumpellyite-actinolite might change as a result of the continuous prograde dehydration reaction between chlorite and pumpellyite. In chlorite-rich bulk compositions the chlorite-pumpellyite-actinolite field becomes progressively more magnesian until all pumpellyite is destroyed. In pumpellyite-rich bulk compositions the three phase field becomes progressively more magnesian until all chlorite is consumed. Comparison of actinolite-bearing assemblages 77 and 224B in Figure 35 indicates that the reaction in sample 224B has progressed farther than in sample 77, implying that sample 224B was metamorphosed at a slightly higher grade than sample 77.

Unlike sample 224B, sample 77 was not nearly so well recrystallized during the second phase deformation. Chlorite analyses reflect local domains of chemical equilibrium with white mica, epidote, and pumpellyite, or chlorite, actinolite, and pumpellyite as shown in Figure 43. This essentially means that localized bulk compositions might react independently due to low intergranular diffusion rates.

Experimental investigations by Nitsch (1971) using natural iron-bearing assemblages reversed the equilibrium: pumpellyite + chlorite + quartz = actinolite + clinozoisite + H_2O at 340 degrees centigrade at 4

kilobars, and 370 degrees centigrade at 7kbar. The lower pressure reaction may not occur in nature because prehnite + pumpellyite + albite may be stable. Schiffman and Liou (1980) found that in the CMASH system pure Mg-Al pumpellyite breaks down to grossular garnet by the reaction; Mg-Al pumpellyite = clinozoisite + grossular + chlorite + quartz + H_2O . This reaction was reversed between 350° and 375°C at pressures ranging from 5 to 8 kilobars. The assemblage produced is not a common natural assemblage but this reaction may nevertheless represent the

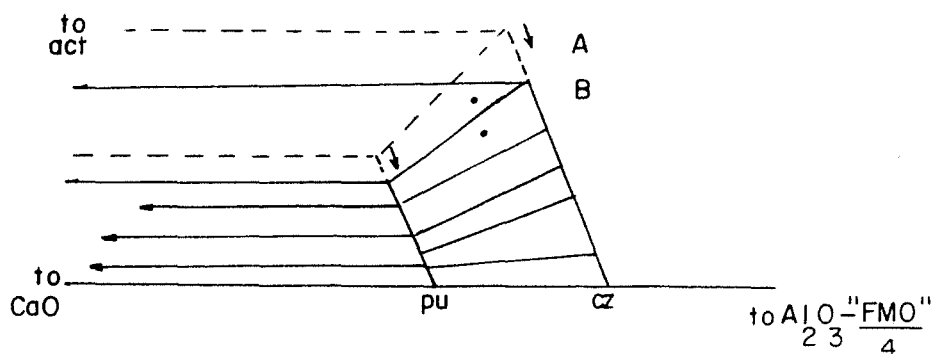


Figure 40. Modified chlorite projection illustrating the reaction which destroys ferric pumpellyite to produce actinolite more aluminous epidote, and more aluminous pumpellyite.

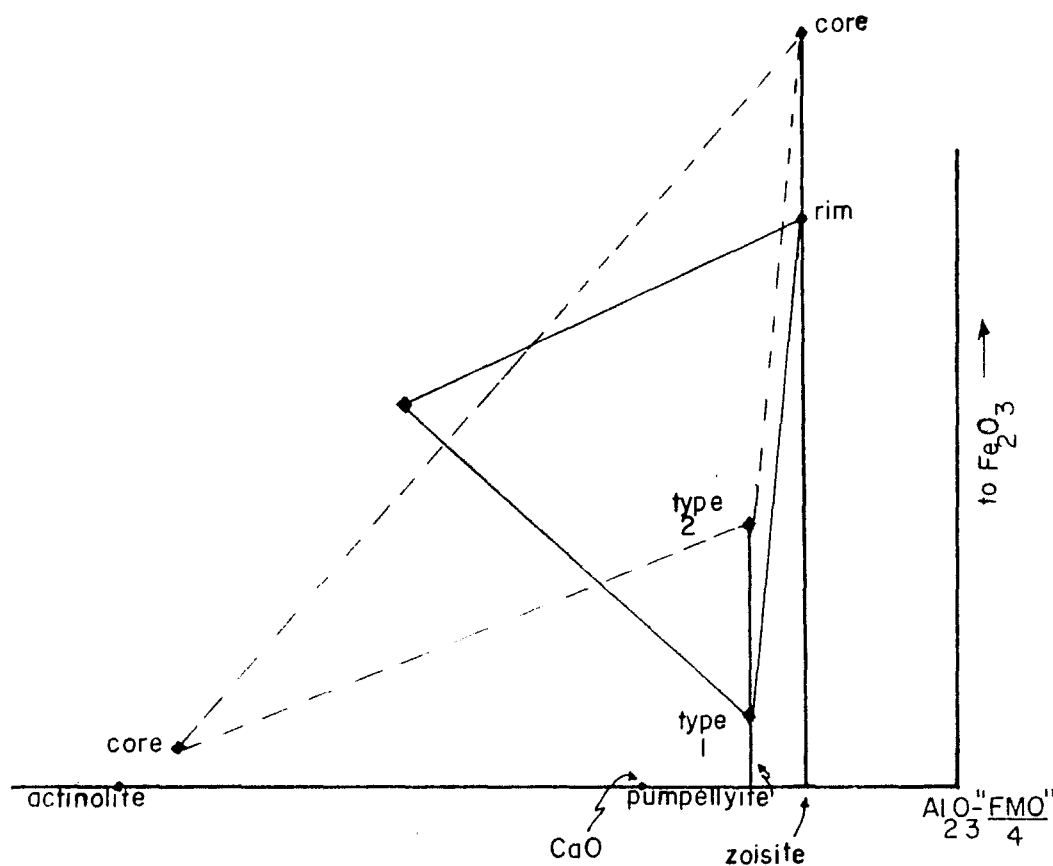


Figure 41. Chlorite projection utilizing data from sample 224 to illustrate ferric pumpellyite consumption and the production of actinolite. Type 2 ferric pumpellyite is assumed to have coexisted with core epidote and actinolite compositions.

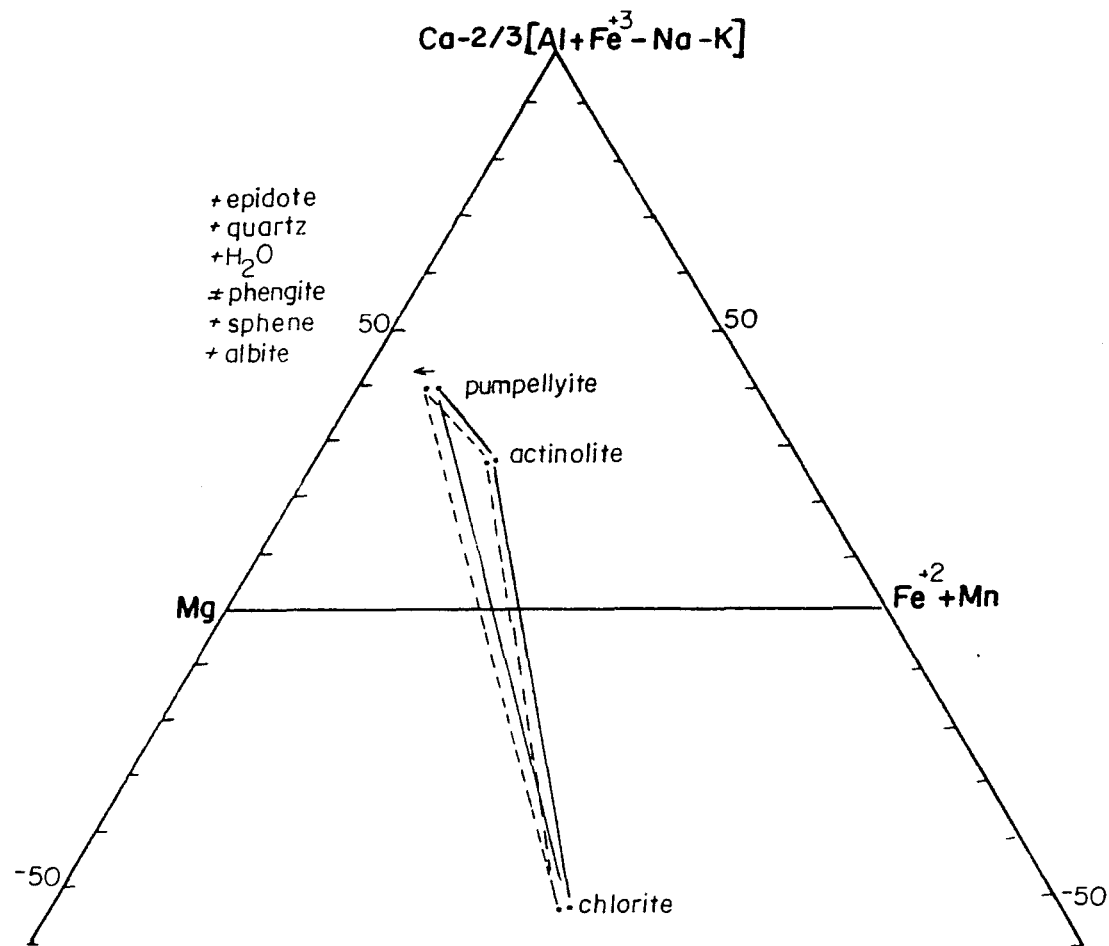


Figure 42. Expected variation in Mg ratio during pumpellyite consuming reactions. In chlorite rich rocks the three phase field becomes progressively more magnesian until all pumpellyite is consumed. In pumpellyite rich rocks the assemblage becomes more magnesian until all chlorite is consumed.

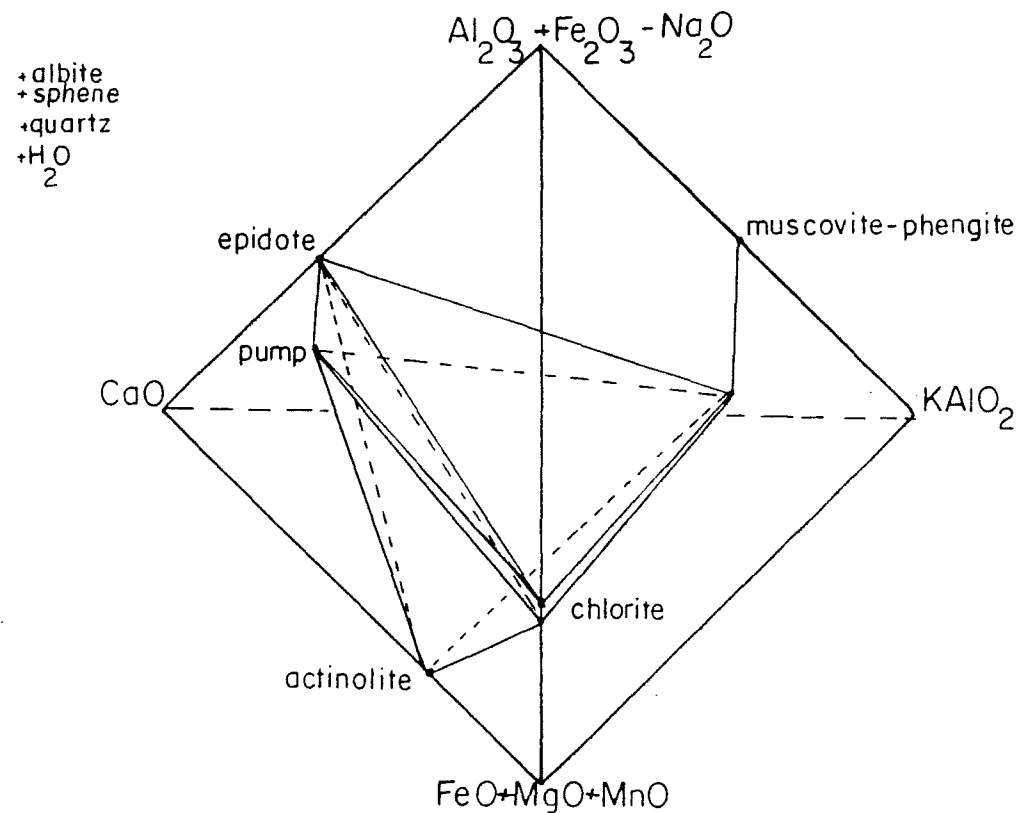


Figure 43. Illustration of the possible phase relations for sample 77. Some domains of the rock are represented by chlorite-pumpellyite-epidote-phengite, while others are represented by act- chlorite-and pumpellyite.

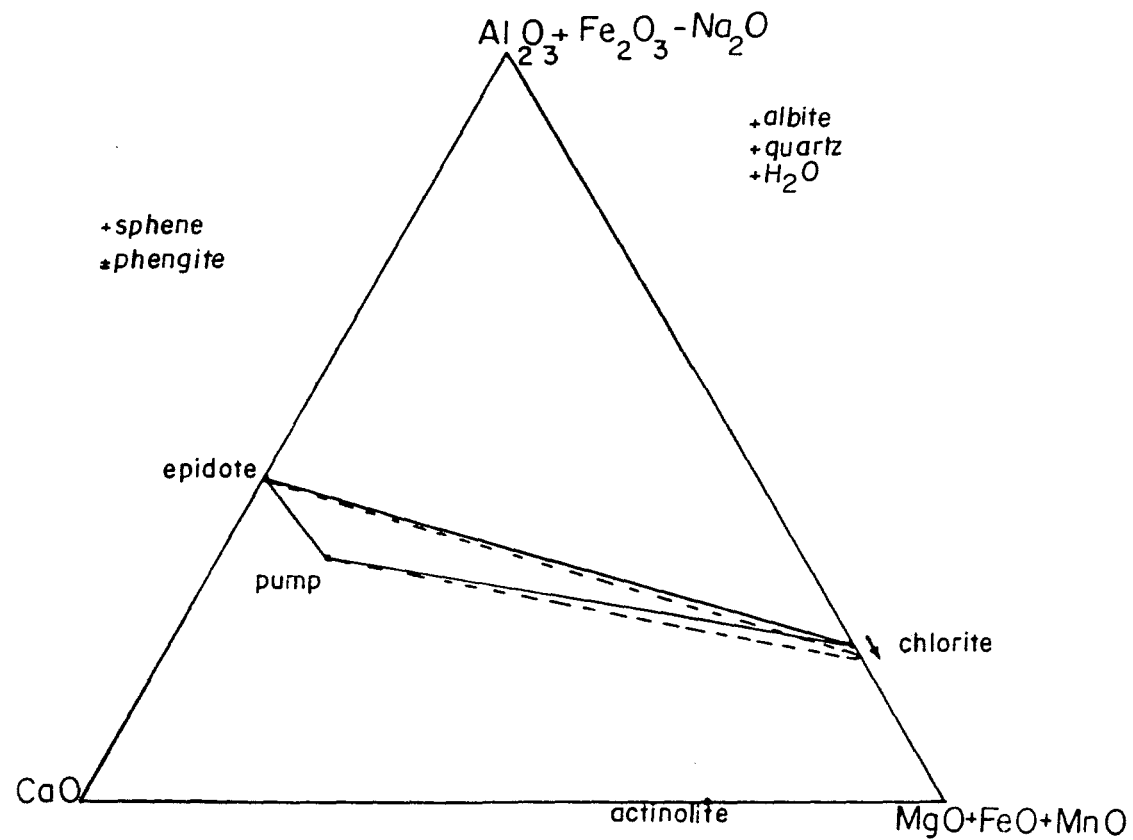


Figure 44. Illustration of the reaction pumpellyite+Al-chlorite= epidote + less-Al chlorite for three phase assemblage rocks.

maximum thermal stability of Mg-Al pumpellyite.

In Chatham Island schist, with the three-phase assemblage epidote-chlorite-pumpellyite with quartz and H_2O , Fe^{3+} -pumpellyite reacts to form less ferric pumpellyite and more aluminous epidote. The reaction is illustrated in Figure 44. On the ACF diagram the reaction is pumpellyite + Al-chlorite = less Al-chlorite + more epidote + H_2O . This reaction, as in the actinolite-bearing assemblages, will occur at lower temperatures in rocks that have higher ferric iron content and at higher temperatures in rocks that have less ferric iron. This reaction will continue until all the ferric pumpellyite is gone and the rock is within the two-phase field, epidote-chlorite, or the reaction is intersected by the actinolite-producing reaction. It seems likely that small domains of sample 77 followed this path (Figure 44).

Other reactions that destroy pumpellyite and form actinolite are possible, but petrographic evidence or mineral data do not suggest that they are important in Chatham Island schists. For example, Bishop (1972) suggested pumpellyite + calcite + hematite = epidote + actinolite + H_2O + CO_2 , and pumpellyite + quartz + CO_2 = epidote + actinolite +

calcite + H_2O as reactions that lead to the disappearance of pumpellyite. The absence of hematite, the scarcity of calcite, and the abundance of pumpellyite indicate that these reactions are not significant.

PHASE RELATIONS AND MINERAL REACTION INVOLVING GARNET

Garnet is an uncommon metamorphic mineral in very low grade rocks worldwide. The occurrence and mineral chemistry of spessartine-grossular garnets has been described commonly (Lee et al., 1962; Ernst et al., 1970; Hermes, 1970; Muller and Schneider, 1971). However, there have been no reactions proposed for the formation of these garnets.

At Chatham Island, garnet is thought to have formed by two different geologic processes. In one occurrence in sample 331 garnet has formed by a metasomatic reaction between an unusual manganiferous carbonate nodule and surrounding greenschist. Unpublished microprobe analyses by R. J. Tracy (pers. comm. 1976) from the carbonate nodule are shown in Table 15 and are plotted in terms of Ca - Fe+Mg - Mn in Figure 45. The fairly systematic arrangement of compositions, where carbonate within the nodule interior is very Mn-rich and carbonate outside the interior and especially near garnet is depleted in Mn, suggests that the garnet has formed by the following generalized reaction: Mn-Ca carbonate + chlorite schist = spessartine garnet + Ca-richer carbonate + H_2O + CO_2 (Robinson, personal communication).

The second occurrence of garnet is within siliceous schist sample 210B not associated with manganiferous carbonate nodules. This garnet probably formed in a more straight-forward metamorphic reaction. Electron microprobe analyses of chlorite, calcite, and garnet are shown

GARNET

SiO ₂	36.74	37.12	36.19
TiO ₂	0.41	0.31	0.37
Al ₂ O ₃	21.26	20.88	20.74
Cr ₂ O ₃	0.08	0.00	0.02
FeO	0.20	0.79	1.32
MnO	38.20	36.99	35.96
MgO	0.00	0.00	0.00
CaO	<u>4.53</u>	<u>4.19</u>	<u>4.66</u>
	101.42	100.28	99.26
Si	2.955	3.006	2.970
Al	<u>.045</u>	<u> </u>	<u>.030</u>
	3.000	3.006	3.000
Al	1.971	1.995	1.977
Ti	.025	.019	.023
Cr	<u>.005</u>	<u> </u>	<u>.001</u>
	2.001	2.014	2.001
Fe	.014	.053	.091
Mn	2.604	2.540	2.501
Ca	<u>.391</u>	<u>.364</u>	<u>.410</u>
	3.009	2.957	3.002
alm	0.47	1.79	3.03
spess	86.54	85.90	83.31
gross	12.99	12.31	13.66

Table 15. Unpublished microprobe analyses (Tracy, unpublished data, 1976) of garnet and carbonate from a manganiferous carbonate nodule from Chatham Islands.

CARBONATE

	adjacent to garnet					interior		
CaO	32.89	44.26	51.45	52.60	5.14	24.67	28.36	38.49
MnO	19.40	14.58	5.16	2.60	50.68	29.78	22.45	16.14
FeO	0.38	0.30	0.78	0.48	0.09	0.43	0.43	0.73
MgO	<u>0.49</u>	<u>0.17</u>	<u>0.27</u>	<u>0.12</u>	<u>0.62</u>	<u>0.42</u>	<u>0.30</u>	<u>0.35</u>
	53.16	59.31	57.66	55.80	56.53	55.30	51.54	55.35
Mg	.014	.004	.007	.003	.019	.012	.013	.009
Fe	.006	.004	.011	.007	.008	.007	.005	.005
Mn	.312	.205	.072	.037	.868	.479	.378	.245
Ca	<u>.668</u>	<u>.787</u>	<u>.910</u>	<u>.953</u>	<u>.115</u>	<u>.502</u>	<u>.604</u>	<u>.741</u>
	1.000	1.000	1.000	1.000	1.000	1.000	1.000	1.000

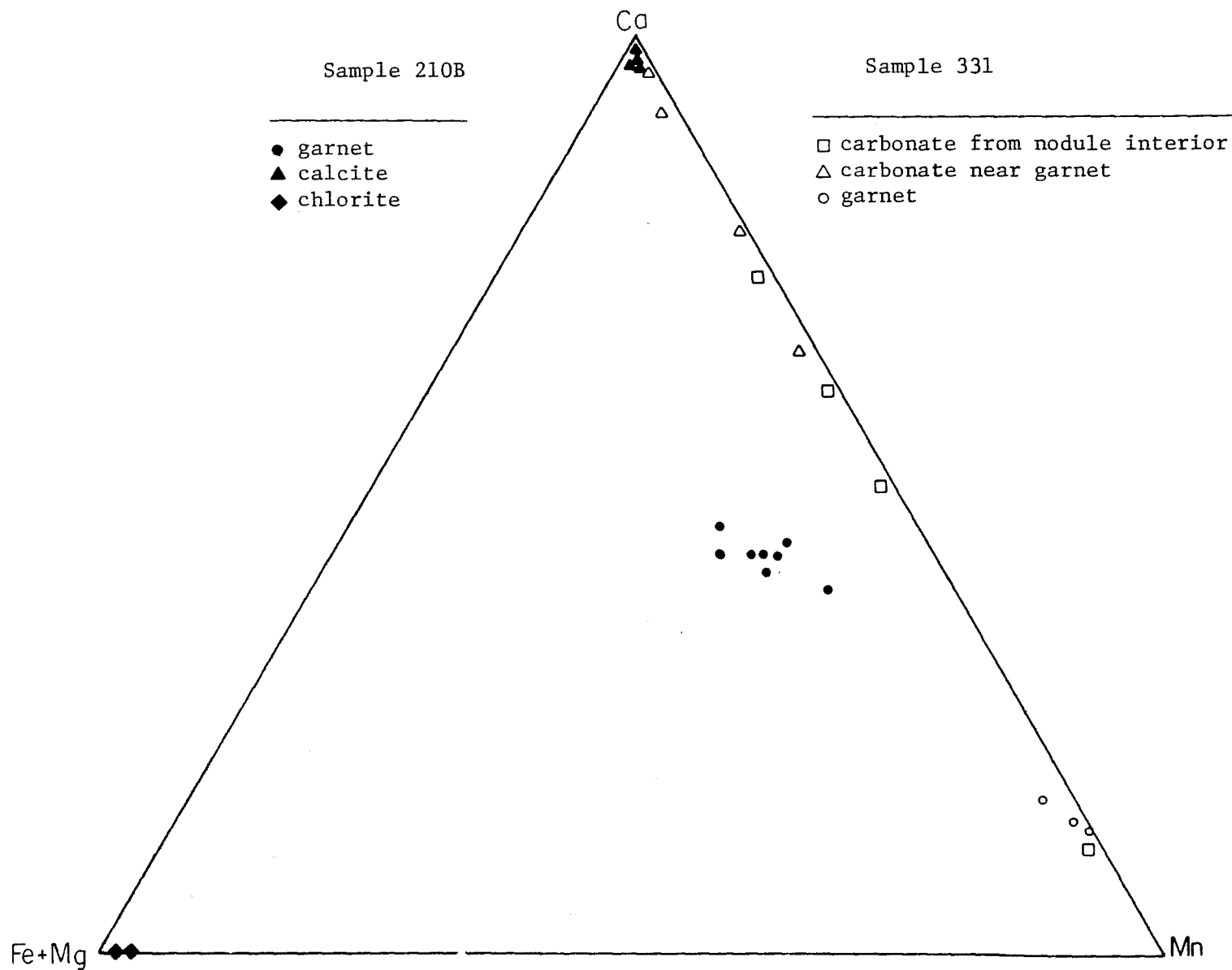


Figure 45. Microprobe analyses of garnet and carbonate from a manganiferous carbonate nodule (sample 331), and for comparison garnet, chlorite, and calcite analyses from a garnet-bearing schist (sample 210B).

in Figure 45 and are also shown on an ACF diagram in Figure 46. Figure 46 shows that garnet might form by several different reactions dependent upon the bulk composition of the protolith: The first reaction appears in Figure 46 as a discontinuous one which first produces garnet from the surrounding minerals: 1) epidote + chlorite + calcite = garnet + H_2O + CO_2 (where garnet appears within the three-phase triangle). The second

and third reactions appear in Figure 46 as continuous ones in which the garnet field expands at the expense of other minerals: 2) epidote + calcite = garnet + H_2O + CO_2 (where garnet moves toward grossular), and 3) epidote + chlorite = garnet + H_2O (where garnet moves toward

spessartine and almandine). The first reaction is most interesting particularly when it is recognized that the components lumped in the A, C, and F apices of Figure 46, make the real reaction a continuous one. As this reaction produces garnet, the minerals continuously change composition and modal abundance, until one of the reactants is consumed. The amount of H_2O and CO_2 given off is dependent upon reactant mineral compositions at each stage of the reaction.

The substantial MnO component in garnet and the other minerals is obscured in the ACF diagram. A more realistic portrayal of the phase relations and reactions that are important in this garnet reaction are obtained by expanding the ACF diagram into a tetrahedron, considering MnO as a separate component. Figure 47 is an $[\text{Al}_2\text{O}_3 + \text{Fe}_2\text{O}_3] - [\text{CaO}] - [\text{FeO} + \text{MgO}] - [\text{MnO}]$ tetrahedron on which averaged mineral analyses from sample 210B are accurately plotted. Figure 47 suggests that the continuous metamorphic reaction that produced garnet was: epidote + Mn-calcite + Mn-chlorite = CaMn-garnet + H_2O + CO_2 . This continuous, dehydration and decarbonation reaction initially forms spessartine-rich garnets which are progressively enriched in grossular and almandine components as the reaction proceeds, while the reactants are rapidly depleted of Mn components. To see this continuous reaction even more effectively the phase relations are illustrated by projecting from epidote onto the basal plane of the $[\text{Al}_2\text{O}_3 + \text{Fe}_2\text{O}_3] - [\text{CaO}] -$

$[\text{MgO} + \text{FeO}] - [\text{MnO}]$ tetrahedron (Figure 48). This reaction consumes chlorite and epidote to form garnet but the garnet chemistry, at each stage of the reaction is dependent on its spatial proximity to other minerals.

Chlorite in sample 210B is interesting petrographically because some chlorite has abnormal brown interference colors in the cores and abnormal violet and even blue interference colors along the rims, especially when the chlorite is near garnet or touching garnet. Microprobe analyses show that chlorite near garnet has interiors with $\text{Mg}/(\text{Mg} + \text{Fe} + \text{Mn}) = .46$ whereas some chlorite rims near garnet have $\text{Mg}/(\text{Mg} + \text{Fe} + \text{Mn}) = .49$ indicating that the rims are depleted in FeO. Also chlorite interiors have $\text{Al}/(\text{total octahedral cations}) = .22$ whereas some chlorite rims in contact with garnet or near garnet have $\text{Al}/(\text{total octahedral cations}) = .18$. The chlorite composition therefore is highly



Figure 46. ACF diagram depicting phase relations for garnet-bearing schist sample 210B. Notice the position of the carbonate substantially away from calcite and the composition of garnet intermediate between grossular and spessartine.

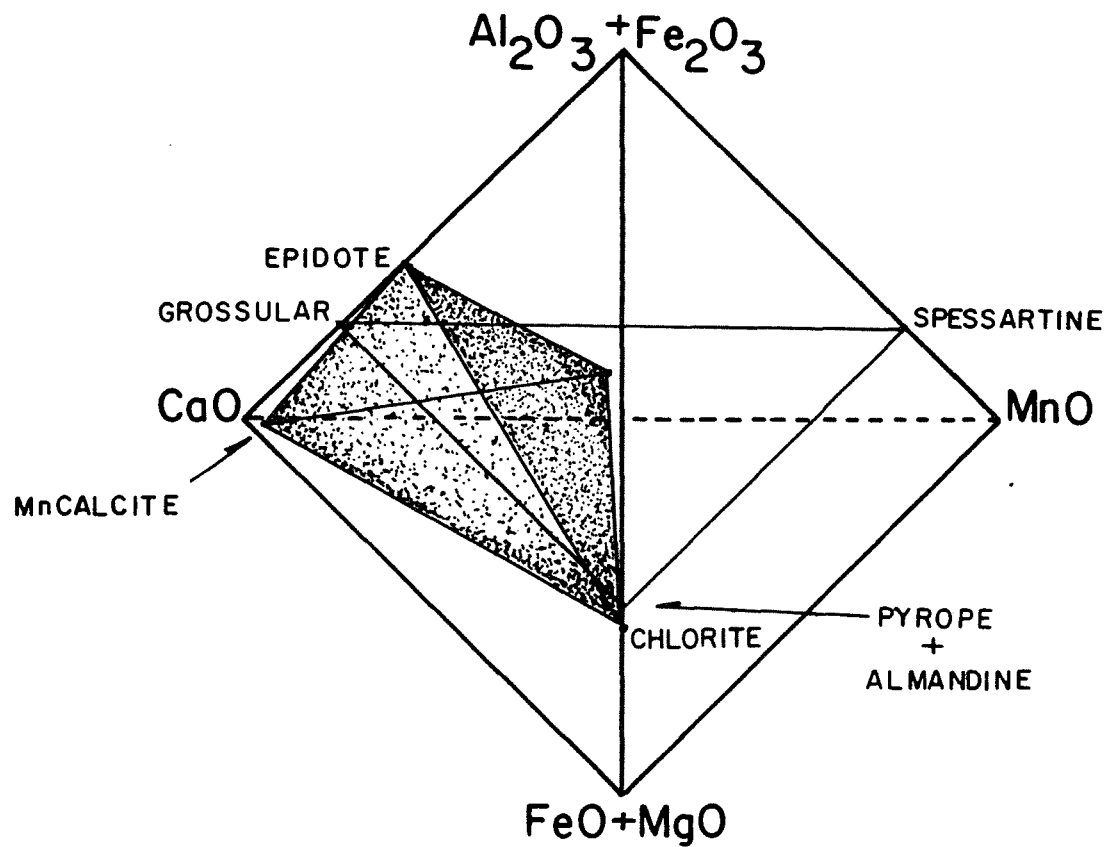


Figure 47. Expanding the ACF diagram into a tetrahedron by adding MnO as a separate component clearly shows the substantial spessartine component in garnet.

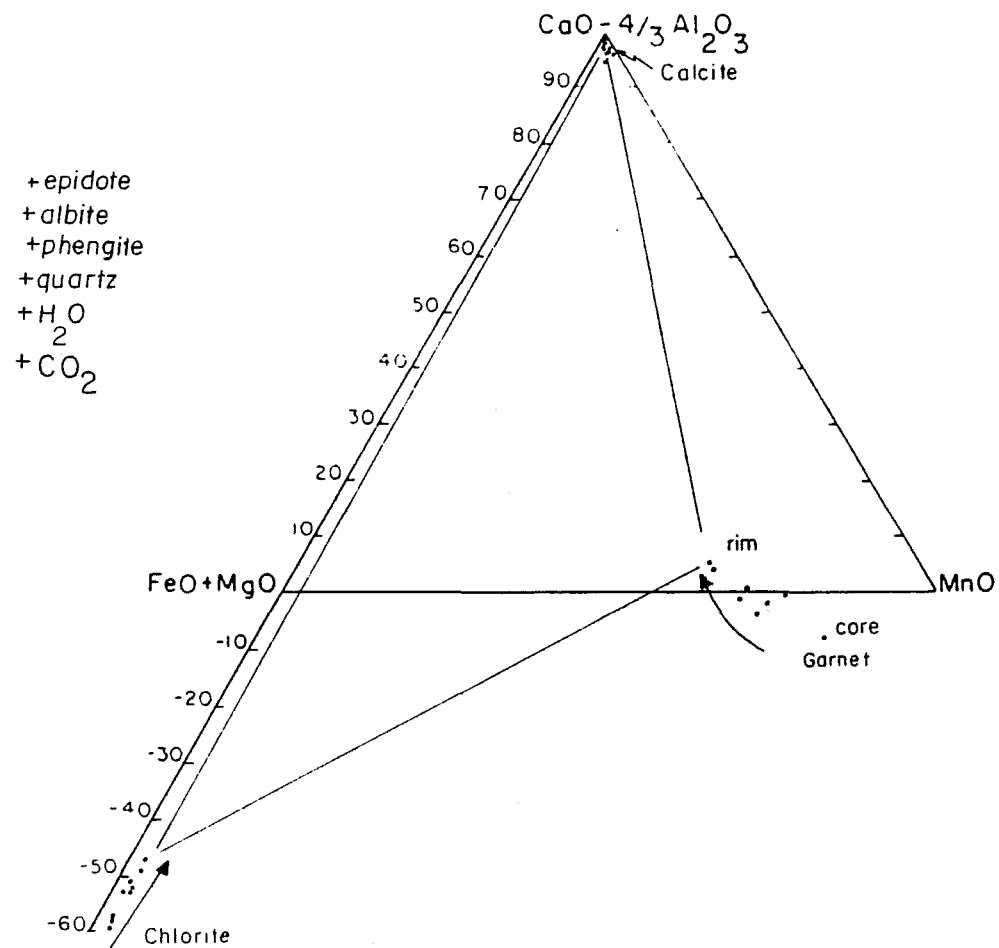
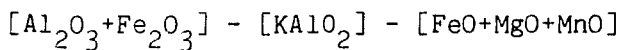


Figure 48. Epidote projection onto the basal plane $\text{CaO}-\text{FeO}+\text{MgO}-\text{MnO}$ permits detailed analysis of $\text{MnO}-\text{Al}_2\text{O}_3$ - and $\text{FeO}+\text{MgO}$ variation in chlorite, epidote, and carbonate.

variable both with respect to its position in the thin section and with respect to any individual grain analysis.

Epidote is also interesting in this sample and the petrographic diversity and range of mineral composition is complicated. Some clearly zoned epidotes are elongated parallel to the second-phase foliation and have wide colorless rims in this direction but no rims or very thin rims perpendicular to this direction. Microprobe analyses show that the wide rims are less ferric than the thin rims. Also, some epidotes in contact with garnet have more ferric rims than epidote rims not in contact with garnet. Some epidotes are more evenly zoned from yellow-green cores to colorless rims. Epidote also occurs as strongly colored inclusions within garnet.

The mineral data and petrographic evidence suggest that the garnet equilibrium composition depends on the proximity of each garnet grain to epidote and chlorite. If garnet is closer to chlorite it has a slightly higher almandine component whereas garnet near epidote may have a higher grossular component. The garnet appears to have formed from Mn-rich calcite, epidote and chlorite and as Mn was used up or became trapped in the cores of garnet the effective bulk composition became more iron rich. At this later stage of the reaction, garnet nucleation and growth became heavily dependent on diffusion of Fe^{2+} and Al out of chlorite such that only chlorite rims were able to react with epidote, calcite, and garnet. The random distribution and the large number of garnet grains suggests that garnet nucleation continued as garnet grew (Kretz, 1973). In general the short distances that material could travel along intergranular diffusion paths probably limited garnet growth. The chemically zoned chlorites indicate that in some areas of the thin section the limiting step in the garnet reaction may have been slow volume diffusion in chlorite so that only the rims were able to react and equilibrate with garnet (Kretz, 1973; Tracy, 1982) in this quartz-rich rock. These small distances of diffusion were in marked contrast to the longer distances that material had to diffuse for the garnet formation and growth in the metasomatic garnet reaction on the edges of the Mn carbonate nodule. In particular Al diffusion and large movement of CO_2 had to occur in order for the reaction to proceed.



If potassium is considered as an additional component, white mica is the only additional phase stabilized in Chatham Island schists. In general, greenschists contain only small amounts of K_2O ; not enough to stabilize a potassic phase, sample 299 being the exception.

The AKF diagram (Figure 49) is useful for illustrating white mica - chlorite phase relations. The white mica - chlorite two-phase region will not in general limit white mica to the maximum phengite composition at a particular metamorphic grade (Guidotti and Sassi, 1976). The compositional variability of white micas and chlorite is similar to white mica and chlorite analyses from other pumpellyite-actinolite

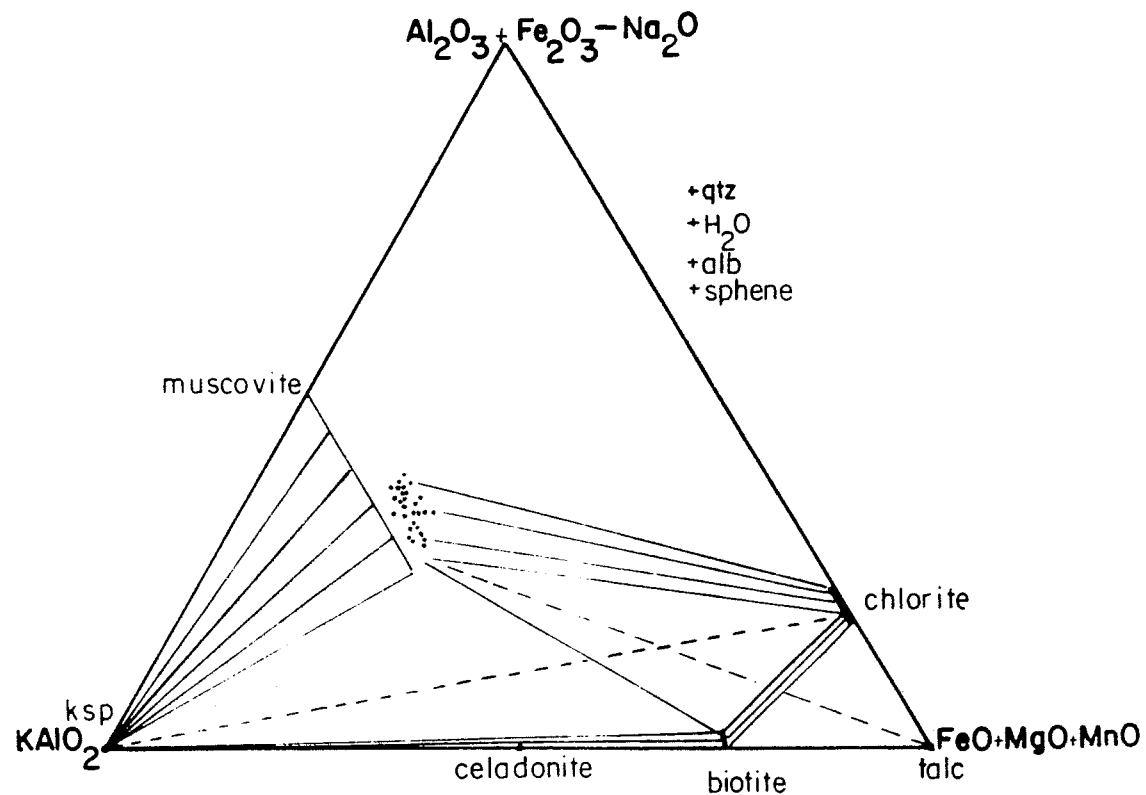


Figure 49. AKF diagram illustrates the expanded compositional stability field of white mica in Chatham Island schists.

facies terranes (Kawachi, 1975; Coombs et al., 1976). The large composition field of white mica in Figure 49 illustrates that white mica - chlorite two-phase stability is maintained for a large range in bulk compositions, as opposed to the white mica - chlorite - K-feldspar, or white mica - chlorite - biotite three-phase assemblages that could be important under other metamorphic conditions or for other bulk compositions.

An increase in temperature or decrease in pressure decreases the compositional stability range of white mica and permits white mica and chlorite to coexist with other AKF phases (Ernst, 1963; Korikovski, 1965; Velde, 1965; van der Plas, 1959; Mather, 1970; Thompson, 1976). Many reactions have been proposed to explain the decrease in celadonite component. All produce a less phengitic white mica, modally less white mica, and modally more biotite and/or K-feldspar, as the reaction proceeds.

Velde (1965) experimentally determined that in white mica - chlorite - K-feldspar assemblages the celadonite component increases with increased pressure. Ernst, 1963 found that, for the reaction phengite + chlorite = muscovite + biotite + quartz + H₂O, unit cell data indicate

that the left hand side of the reaction is favored by an increase in pressure. The exchange reaction phengitic white mica + Al chlorite = Al-white mica + MgFe chlorite (Guidotti, 1984, p. 403) is particularly important in the understanding of how white mica composition at low metamorphic grades changes with changing pressures. Particularly critical is determining the direction of the reaction with increased pressure.

As indicated on the AKF diagram in Figure 50 the compositional differences between chlorites in sample 298, 77, and 44 and the compositional differences between white micas from the samples 298, 77, and 44 are very small. These small differences are examined in detail in terms of the tschermaks exchange, following Tracy (1975), in Figure 51.

In Figure 51 chlorite-white mica tie lines from Chatham Island are compared with other diverse occurrences of these minerals. Chlorite-white mica pairs from Lincoln Mountain, Vermont (Albee, 1965) are low kyanite zone pelitic schists. The central Massachusetts data (Hollocher, 1981) are from schists from the Devonian Littleton Formation retrograded to the biotite zone. These two occurrences contrast markedly with chlorite-white mica pairs from Chatham Island and chlorite-white mica pairs from the blueschist terrane of the Shirataki district, Japan (Ernst et al., 1970). The unusual tie lines from the Shirataki blueschists suggest that Al is favored in chlorite over phengite under very high pressure, low temperature metamorphic conditions.

The close spatial association of white mica and pumpellyite along with their close Mg values in quartz-albite schists indicates that they

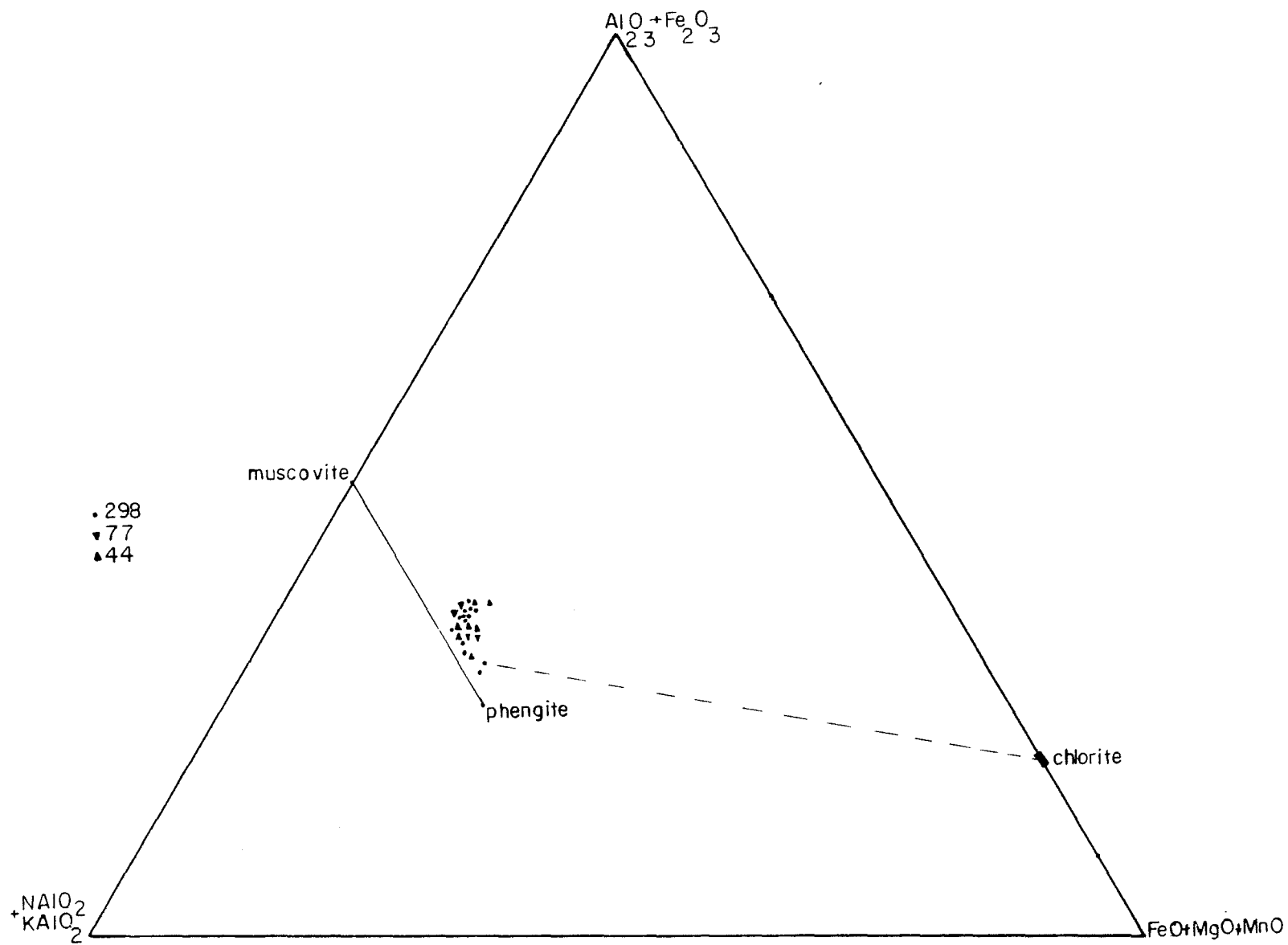


Figure 50. AKF diagram illustrating white mica and chlorite analyses from Chatham Island schists.

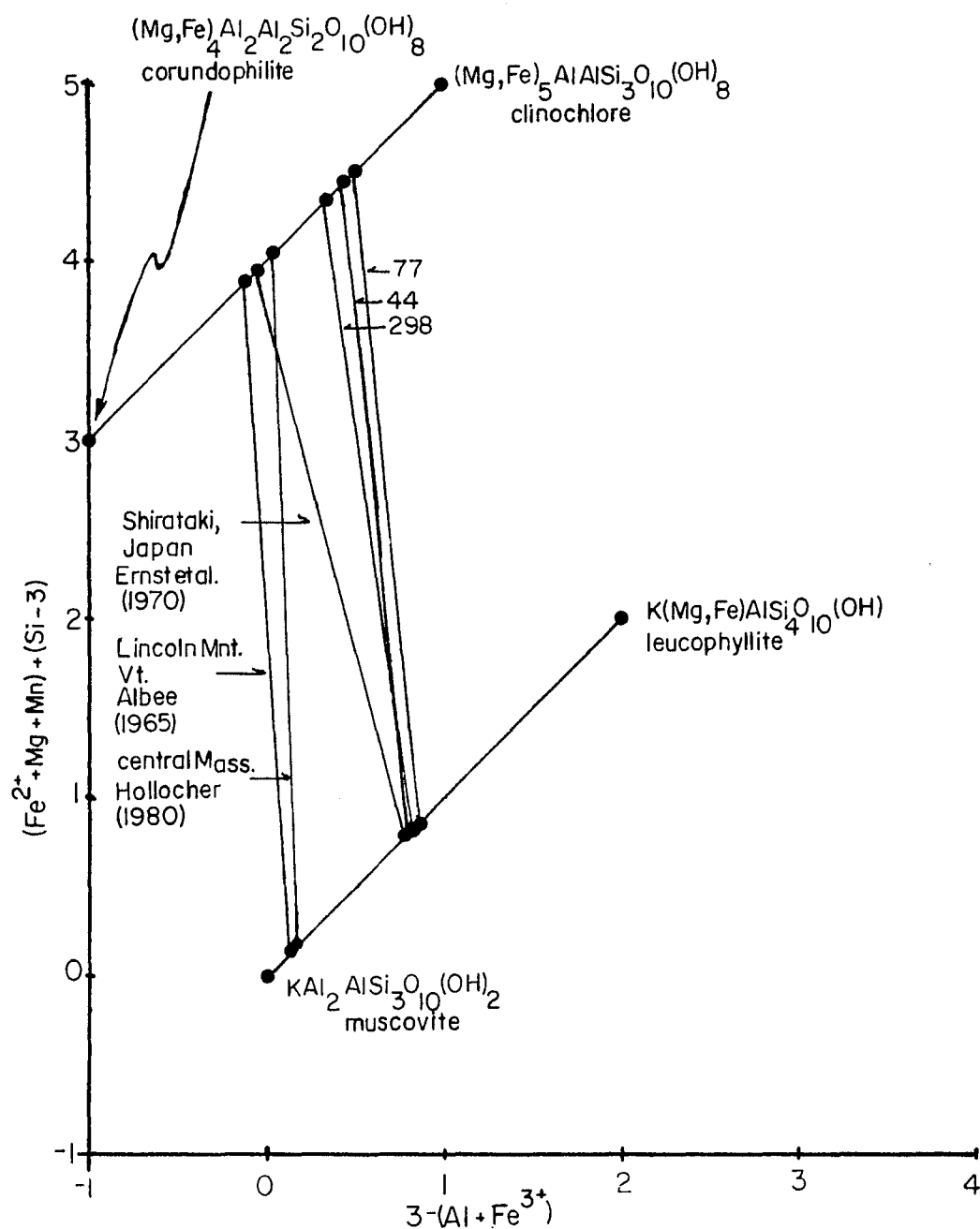


Figure 51. This figure illustrates the tschermak substitution in white micas and chlorites from Chatham Island schists. The figure is from Tracy (1975). For comparison data from Albee (1965); Ernst et al. (1970); and Hollister (1980) are shown.

may have formed by a reaction such as pumpellyite + muscovite = phengite + chlorite + epidote + H_2O . This reaction, when considered as a

continuous reaction involving both Fe_2O_3 - Al_2O_3 fractionation and FeO-

MgO fractionation, may be ferric pumpellyite + muscovite = phengite + Al-pumpellyite + epidote + chlorite + H_2O , and may occur with increasing

temperature associated with pumpellyite-actinolite facies metamorphism. This type of equilibrium may be responsible for the zoning trends in pumpellyite in quartz-albite schists without actinolite.

CONDITIONS OF METAMORPHISM

Some estimates of metamorphic conditions can be made based on phase relations of coexisting minerals from Chatham Island schists. Petrographic observations indicate that the most ferric pumpellyites detected occur as aggregate crystals, some possibly pseudomorphing pyroxene, and now enclosed by the second-phase foliation. This implies an early pumpellyite-forming metamorphism prior to crystallization of the present dominating matrix mineral assemblages. The pervasive second-phase deformation and the localized third-phase deformation are associated with prograde reactions that consumed ferric pumpellyite and ferric epidote; and produced actinolite, more aluminous epidote, and more aluminous pumpellyite.

Metamorphic mineral segregation and grain-size reduction associated with the second phase of deformation were important in allowing intergranular diffusion to occur over thin-section-sized areas and promoting equilibrium between coexisting minerals. The development of the strong second-phase foliation in the southwest appears to have increased intergranular diffusion and reaction rates in that area permitting relatively large actinolite crystals to grow. This interpretation is consistent with theoretical models (Brady, 1983) which predict maximized intergranular diffusion along grain boundaries aligned parallel to the diffusion gradient.

Some metamorphic temperature estimates have been discussed during the previous section. Geothermometers based on element fractionation data are not generally available, possibly due to the inability to directly measure Fe^{3+} and the complexity of the mineral chemistry of calcium aluminosilicates such as pumpellyite. However, some partitioning data has accumulated in the literature and this can be used to compare and estimate temperatures.

$\frac{(Mg/Fe)_{act}}{(Mg/Fe)_{chl}}$. A comparison of fractionation data from

actinolite-bearing assemblages from Chatham Island schist with those of Coombs et al., (1976) from Loeche, Switzerland suggests temperatures of 270-340 degrees centigrade.

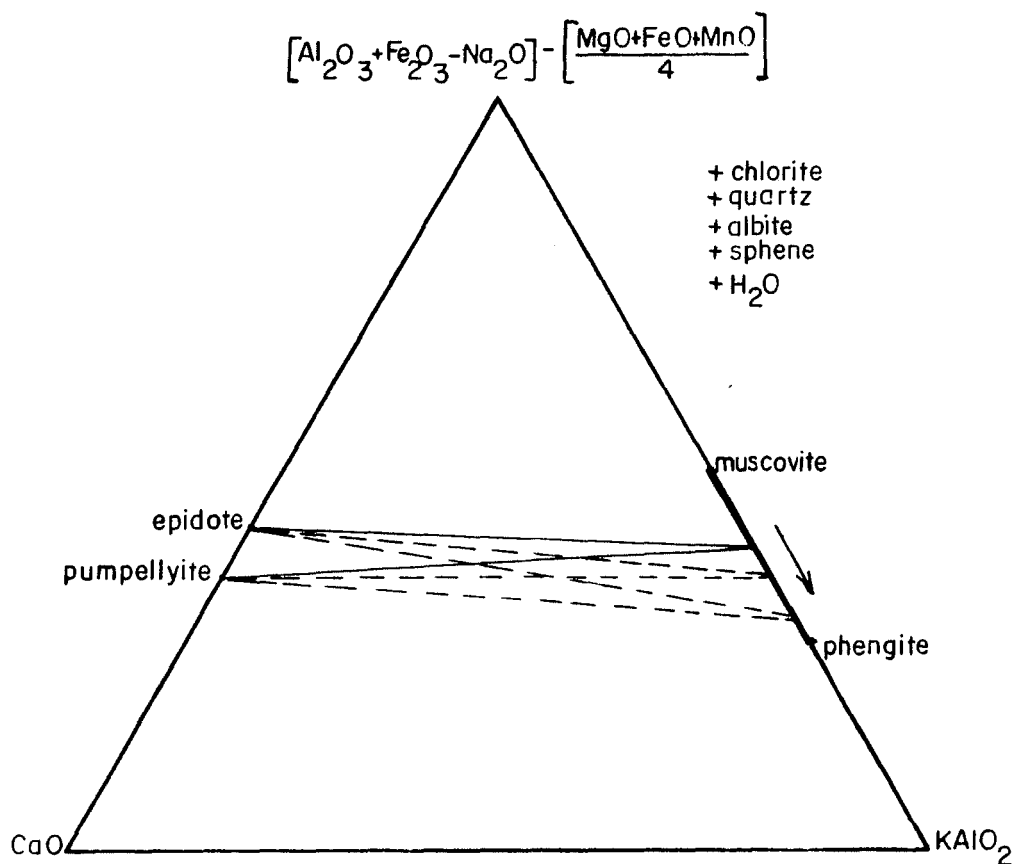


Figure 52. Projection from chlorite onto the $[\text{Al}_2\text{O}_3 + \text{Fe}_2\text{O}_3 - \text{Na}_2\text{O}] - [\text{CaO}] - [\text{KAIO}_2]$ face of the $[\text{Al}_2\text{O}_3 + \text{Fe}_2\text{O}_3 - \text{Na}_2\text{O}] - [\text{CaO}] - [\text{FeO} + \text{MgO} + \text{MnO}] - [\text{KAIO}_2]$ tetrahedron. This figure illustrates how white mica becomes progressively more phengitic during a continuous, dehydration reaction which consumes pumpellyite.

$\text{Fe}^{3+}/(\text{Fe}^{3+} + \text{Al})_{\text{epidote}}$. Nakajima et al. (1977) proposed a

geothermometer for the assemblage epidote-chlorite-pumpellyite-actinolite based on the Fe^{3+} content of epidote. Their model makes some assumptions about the maximum Fe^{3+} content possible in epidote at greenschist facies conditions, specifies chlorite with $\text{Mg}/(\text{Mg} + \text{Fe}) = 0.45-0.50$, and arbitrarily establishes a temperature of 300 degrees centigrade for rocks with this assemblage with epidote $X\text{Fe}^{3+} = 0.34$. The most ferric rim composition determined in this study, from sample 224B, gives $X\text{Fe}^{3+}$ of 0.214, and an estimated temperature from this model of 340°C.

Experimental work. Some experimental work helps one to estimate the maximum temperature and pressure for Chatham Island metamorphism. Experiments by Nitsch (1971) with natural iron-bearing pumpellyite with the composition $\text{Fe}^{3+}/(\text{Fe}^{3+} + \text{Al}) = 0.094$ and $\text{Mg}/(\text{Mg} + \text{Fe}^{2+}) = 0.86$, (compare with Figure 26) indicated that pumpellyite is consumed in the reaction pumpellyite + chlorite = actinolite + epidote + H_2O at 340°C at 4

kbar and 370°C at 7 kbars. Schiffman and Liou (1980) have determined that the maximum thermal stability of synthetic pure Mg-Al pumpellyite, where it breaks down to clinozoisite + grossular + chlorite + quartz + H_2O , is 350°C at 5 kbars and 375°C at 8 kbars.

Previous experimental work with garnet can also provide some temperature and pressure information. Hsu (1968) determined the equilibrium pressure and temperature curve for the reaction Mn-chlorite + quartz = spessartine + H_2O occurs at $414^\circ \pm 5^\circ \text{C}$ at 2 kbars,

$405^\circ \pm 5^\circ \text{C}$ at 1 kbar, and $368^\circ \pm 5^\circ \text{C}$ at 0.5 kbars. Hsu (1968) also investigated the equilibrium Fe-chlorite + quartz = almandine + H_2O with fO_2 controlled by iron + quartz = fayalite buffer. He determined that almandine formed at $525^\circ \pm 5^\circ \text{C}$ at 3 kbars, $542^\circ \pm 5^\circ \text{C}$ at 2 kbars, $528^\circ \pm 5^\circ \text{C}$ at 1 kbar and $502^\circ \pm 5^\circ \text{C}$ at 0.5 kbar. At more oxidized conditions almandine forms at higher temperatures by dehydration of chlorite + quartz + magnetite. It would be expected that the garnet-forming reactions studied by Hsu (1968) would proceed at considerably lower temperatures if the fluid were diluted by CO_2 . Using the data of Gordon and Greenwood (1971) for the reaction calcite + zoisite + quartz = grossular + 5CO_2 + $1\text{H}_2\text{O}$, Shoji (1975) calculated that grossular is stable in water-rich environments ($X\text{CO}_2 < 2$ mole %) at temperatures less than 400°C at 2 kbar. If one could consolidate all the divalent oxides into one, then one could consider the reaction assemblage chlorite-quartz-carbonate-epidote-garnet to be at an isobaric invariant point fixed at an $X\text{CO}_2$ of intermediate composition. Such an invariant point would also represent the lowest possible temperature for the stability of garnet in this assemblage.

Quantitative reliable pressure indicators using natural mineral compositions for geobarometry are not available for Chatham Island assemblages. Qualitative estimates based on pumpellyite composition

(Figure 24) suggest intermediate to high pressures similar to other intermediate- to high-pressure low-temperature pumpellyite-actinolite schists.

Phengite content can be used in rocks with the appropriate assemblages to estimate pressure. Chatham Island schists do not contain K-feldspar, but a minimum pressure can be estimated using the data of Velde (1965). Using the Si content of white mica at 3.5 per 11 oxygen formula and choosing temperatures of 250, 300, 325, and 350° C gives minimum pressure estimates of 4.8, 5.6, 6.1, and 6.7 kbars respectively. Unpublished experimental work by Massonne (1981) in the system $K_2O - MgO - Al_2O_3 - SiO_2 - H_2O$ can also be used to estimate minimum

pressures. He investigated the reaction $Mg \text{ phengite} + \text{quartz} = \text{phlogopite} + K\text{-feldspar} + H_2O$. Using his reaction curves and an average Si content of 3.47 per 11 oxygens for Chatham Island phengites indicates pressures of 9.3 kbars at 250°C and 10.5 kbars at 350°C. These last conditions seem unrealistic in that one would expect glaucophane to appear under these conditions in rocks with bulk compositions similar to those on Chatham Island.

Although no rigorous analysis of fluid composition was attempted in this paper, the mineral equilibria give some qualitative indications about the composition of fluid during metamorphism. Pumpellyite stability is restricted to low XCO_2 by the reaction $\text{pumpellyite} + CO_2 = \text{epidote} +$

$\text{calcite} + \text{chlorite} + H_2O$. The small modal proportions of epidote and calcite in sample 427, which has the reaction assemblage, and the large amounts of pumpellyite, suggest that XCO_2 was low during metamorphism. This is probably generally true for most samples studied. However, local larger values of XCO_2 may be responsible for the absence of pumpellyite in some samples (e.g. 210B, or 429). The presence of sphene + calcite at low temperatures as opposed to rutile + calcite + quartz may also indicate low XCO_2 during metamorphism (Ernst, 1972). The

absence of hematite or other stable oxides suggests that none of the metamorphic fluids were oxidizing during metamorphism.

CONCLUSIONS

1) This thesis provides microprobe analyses of phengite, chlorite, epidote, pumpellyite, actinolite, albite, sphene, calcite, and garnet from volcanogenic sediments metamorphosed under pumpellyite-actinolite facies conditions. The mineral data indicates that coexisting minerals in Chatham Island schists are similar in composition to other pumpellyite-actinolite facies schists metamorphosed at intermediate to high pressures.

2) Unusually well developed prismatic crystal faces of pumpellyite in these schists has made it possible to relate some optical properties to crystallographic orientation. By combining information on the

complex pattern of crystal zoning in end sections, the extinction angles ZAc and XAa , and microprobe analyses, it can be shown that some of these pumpellyites grew as hollow-ended "hopper" crystals.

3) The optic orientation of pumpellyite in one greenschist sample appears to be different than in any previous reports. This pumpellyite has the X vibration direction, as opposed to the Y vibration direction, parallel to the b -axis that is the long direction of the crystal. Also, the Z vibration direction appears to be within the obtuse angle β , rather than the acute angle β as in other pumpellyites studied. Microprobe analyses do not as yet indicate the exact relationship between optic orientation and chemical composition, but it appears to be related to their low iron content.

4) Detailed graphical analyses indicate that Chatham Island schists with quartz and albite are characterized by two three-phase ACF assemblages: chlorite-pumpellyite-epidote, and chlorite-pumpellyite-actinolite. Rocks with the actinolite assemblage also contain epidote which is stabilized by higher Fe_2O_3 . Cation-normalized microprobe data

indicate that $XMg_{pumpellyite} > XMg_{actinolite} > XMg_{chlorite}$ where $XMg = Mg/(Mg+Fe^{2+})$.

5) Possible reactions which relate the chemistry of two compositionally diverse types of pumpellyite are presented. In rocks with the actinolite assemblage ferric pumpellyite is consumed during a continuous reaction which produces more aluminous epidote, more aluminous pumpellyite, and actinolite. Ferric pumpellyite and aluminous chlorite can also break down to epidote, less aluminous chlorite and more aluminous pumpellyite in rocks without actinolite. This analysis indicates that actinolite forms in rocks with higher Fe_2O_3 contents well before the final breakdown of pumpellyite. In less ferric bulk compositions pumpellyite should break down at higher temperatures. Mg-Fe fractionations between pumpellyite, actinolite, and chlorite indicate that these three ferromagnesian phases become progressively enriched in Mg during pumpellyite-consuming reactions until all pumpellyite is consumed in chlorite-rich rocks. In pumpellyite-rich rocks the three ferromagnesian phases should become progressively enriched in Mg until all chlorite is consumed.

6) Phengite is the only potassic phase, apparently stabilized by K_2O as an additional component. In rocks with phengite, a possible pumpellyite-consuming dehydration reaction is $pumpellyite + muscovite + quartz = phengite_{3+} + epidote + chlorite + H_2O$, a complex continuous reaction when Fe^{3+} -Al and Mg- Fe^{2+} fractionations are considered.

7) Garnet formation in very low-grade rocks is rare. The results presented here show that garnet formation is highly dependent on manganese-rich bulk compositions. One possible reaction is a continuous devolatilization $Mn\text{-calcite} + Mn\text{-chlorite} + epidote = garnet + H_2O + CO_2$. This reaction may have produced the spessartine-grossular garnet

in garnet-bearing schists at Chatham Island.

8) Element fractionation data and experimental data constrain metamorphism in the temperature range 270 to 340°C and pressures of 4.8 to 7 kbar. One method gives a pressure estimate around 10 kbar, which seems unreasonable in view of the absence of glaucophane. The metamorphic fluids were dominated by H₂O during metamorphism, but locally, higher values of XCO₂ may have prevented pumpellyite assemblages from occurring.

REFERENCES

- Adams, C.J.D., and Robinson, Peter, 1977, Potassium-argon ages of schists from Chatham Island, New Zealand Plateau, Southwest Pacific: *New Zealand Journal of Geology and Geophysics*, v. 20, p. 287-301.
- Aiba, K., 1982, Sanbagawa metamorphism of the Nakatsu-Nanokawa district, the northern subbelt of the Chichibu belt in western central Shikoku, Japan: *Journal of the Geological Society of Japan*, v. 88, p. 875-885.
- Albee, A.L., 1965, Phase equilibria in three assemblages of kyanite zone pelitic schist, Lincoln Mountain Quadrangle, central Vermont: *Journal of Petrology*, v. 6, p. 246-301.
- _____, and Ray, Lily, 1970, Correction factors for electron probe microanalysis of silicates, oxides, carbonates, phosphates, and sulfates: *Analytical Chemistry*, v. 42, p. 1408-1414.
- Allmann, P., and Donnay, G., 1971, Structural relations between pumpellyite and ardennite: *Acta Crystallographica*, v. B27, p. 1871-1875.
- Amstutz, G.C., 1968, Spilites and spilitic rocks, *in* Hess, H.H. and Poldervaart, Arie, editors, *The Poldervaart Treatise on Rocks of Basaltic Composition*: Interscience (Wiley) New York, p. 737-754.
- Andrews, A.J., 1977, Low temperature fluid alteration of oceanic layer II basalts DSDP Leg 37: *Canadian Journal of Earth Science*, v. 4, p. 911-926.
- Bailey, S.W., 1984, Crystal chemistry of true micas, *in* Bailey, S. W. editor, *Reviews in mineralogy*, v. 13 micas: Mineralogical Society of America, Washington, D.C., p. 13-57.
- Bamba, T., 1974, A series of magmatism related to the formation of spilite, *in* Amstutz, G.C., editor, *Spilites and Spilitic Rocks*: Springer Verlag, New York, p. 83-112.
- Bancroft, G. M., Maddock, A.G., and Burns, R.G., 1967, Application of Mossbauer effect to silicate mineralogy. I Iron silicates of known crystal structure: *Geochemica et Cosmochemica Acta*, V. 31, p. 2219-2246.
- Barker, F., 1979, *Trondhjemites, Dacites and Related Rocks*: Elsevier, Amsterdam, 659 p.
- Bence, A.E., and Albee, A.L., 1968, Empirical correction factors for the electron microanalysis of silicates and oxides: *Journal of Geology*, v. 76, p. 382-403.
- Bishop, D.G., Bradshaw, J.D., Landis, C.A., and Turnball, I.M., 1976, Lithostratigraphy and structure of the Caples terrane of the Humboldt Mountains; *New Zealand Journal of Geology and Geophysics*, v. 19, p. 827-848.
- Brady, John B., 1983, Intergranular diffusion in metamorphic rocks: *American Journal of Science*, v. 283-A p. 181-200.
- Brown, E.H., 1967, The greenschist facies in part of eastern Otago, New Zealand: *Contributions to Mineralogy and Petrology*, v. 14, p. 259-292.

- Butler, B.C.M., 1967, Chemical study of minerals from the Moine Schists of the Ardnamurchan area, Argyllshire, Scotland: *Journal of Petrology*, v. 8, p. 233-267.
- Carter, R.M. and Norris R.J., 1976, Cainozoic history of southern New Zealand: an accord between geological observations and plate tectonic predictions: *Earth and Planetary Science Letters*, v. 31, p. 85-94.
- Cheney, J.T. and Guidotti, C.V., 1979, Muscovite-plagioclase equilibria in sillimanite- and quartz-bearing metapelites, Puzzle Mountain area, northwest Maine: *American Journal of Science*, v. 279, p. 411-434.
- Chopin, C., 1981, Talc-phengite a widespread assemblage in high grade pelitic blueschists of the Western Alps: *Journal of Petrology*, v. 22, p. 628-650.
- Coombs, D.S., 1953, The pumpellyite mineral series: *Mineralogical Magazine*, v. 30, p. 113-135.
- _____, Nakamura, Y., and Vuagnat, M., 1976, Pumpellyite-actinolite facies schists of the Taveyanne Formation near Loeche, Valais, Switzerland: *Journal of Petrology*, v. 17, p. 440-471.
- _____, Landis, C.A., Norris, J.M., Sinton, J.M., Borns, D.J., and Craw, D., 1976, The Dunn Mountain ophiolite belt, New Zealand, its tectonic setting, constitution, and origin, with special reference to the southern portion: *American Journal of Science*, V. 276, p. 561-603.
- _____, Horodyski, R.J., and Naylor, R.S., 1970, Occurrence of prehnite-pumpellyite facies metamorphism in northern Maine: *American Journal of Science*, V. 268, p. 142-156.
- Crook, K.A.W. and Feary, D.A., 1982, Development of New Zealand according to the fore-arc model of crustal evolution: *Tectonophysics*, v. 87, p. 65-107.
- Dickinson, W.R., 1971, Clastic sedimentary sequences deposited in shelf slope and trough settings between magmatic arcs and associated trenches: *Pacific Geology*, v. 3, p. 15-31.
- Dollase, W.A., 1968, Refinement and comparison of the structure of zoisite and clinozoisite: *American Mineralogist*, v. 53, p. 1882-1898.
- _____, 1971, Refinement of the crystal structures of epidote, allanite, and hancockite: *American Mineralogist*, v. 56, p. 447-464.
- Ernst, W.G., 1963, Significance of phengitic micas from low grade schists: *American Mineralogist*, v. 48, p. 1357-1373.
- _____, Seki, Y., Onuki, H., and Gilbert, M.C., 1970, Comparative study of low-grade metamorphism in the California Coast Ranges and the outer metamorphic belt of Japan: *Geological Society of America, Memoir* 124, 276 p.
- _____, 1972, CO₂ poor composition of the fluid attending Franciscan and Sanbagawa low-grade metamorphism: *Geochemica et Cosmochemica Acta*, v. 36 p. 497-504.
- _____, 1975, Subduction zone metamorphism: Halsted Press, Stroudsburg, Penn. p. 1-445.

- Eskola, Pentti, 1915, On the relations between the chemical and mineralogical composition in the metamorphic rocks of the Orijarvi region: Bulletin de la Commission geologique de Geol. Finlande, v. 44.
- Evans, B.W., and Guidotti, C.V., 1966, The sillimanite-potash feldspar isograd in western Maine U.S.A.: Contributions to Mineralogy and Petrology, v. 12, p. 25-62.
- Ewart, A., 1979, A review of the mineralogy and chemistry of Tertiary-Recent dacitic, latitic, rhyolitic and related salic volcanic rocks, in F. Barker, editor, Trondhjemites, dacites and related rocks: Elsevier, New York, 1979, p. 13-112.
- Ferry, J.M., 1976, P, T, and $f\text{CO}_2$ and $f\text{H}_2\text{O}$ during metamorphism of calcareous sediments in Waterville-Vassalboro area, south-central Maine: Contributions to Mineralogy and Petrology, v. 57, p. 119-143.
- Finch, J., Gainsford, A.R., and Tennant, W.C., 1982, Polarized optical absorption and ^{57}Fe Mossbauer study of pegmatitic muscovite: American Mineralogist, v. 67, p. 59-68.
- Fleming, A.M., 1970, The Mesozoic of New Zealand: chapters in the history of the circumPacific mobile belt: Geological Society of London, Quarterly Journal, v. 125, p. 125-170.
- Floyd, P.A., and Winchester, J.A., 1978, Identification and discrimination of altered metamorphosed volcanic rocks using immobile elements: Chemical Geology, v. 21, p. 291-306.
- Galli, E., and Alberti, A., 1969, On the crystal structure of pumpellyite: Acta Crystallographica, v. B25, p. 2276-2281.
- Giese, R.F., 1984, Electrostatic energy models of micas, in Bailey, S.W., ed., Reviews in mineralogy, v. 13 micas: Mineralogical Society of America, Washington, D.C., 1984, p. 125-141.
- Goldschmidt, V.M., 1912, Die gesetze der gesteinsmetamorphose mit beispielan aus der geologie des sudlichen Norwegens: Vidensk. Skr. I, Mat.-Natur v. K1, no. 22.
- Gordon, T.M., and Greenwood, H.J., 1971, The stability of grossularite in $\text{H}_2\text{O}-\text{CO}_2$ mixtures: American Mineralogist, v. 56, p. 1674-1680.
- Graham, C.M., 1974, Metabasite amphiboles of the Scottish Dalradian: Contributions to Mineralogy and Petrology, v. 47, p. 165-185.
- Gray, D.R., 1979, Microstructure of crenulation cleavages, an indicator of cleavage origin: American Journal of Science, v. 279, p. 97-128.
- Green, T.H., 1981, Synthetic high-pressure micas compositionally intermediate between the dioctahedral and trioctahedral mica series: Contributions to Mineralogy and Petrology, v. 78, p. 452-458.
- Greenwood, H.J., 1967, The n-dimensional tie line problem: Geochemica et Cosmochemica Acta, v. 31, p. 465-490.
- Grindley, G.W., Adams, C.J.D., Lumb, J.T., 1977, Paleomagnetism, K-Ar dating and tectonic interpretation of Upper Cretaceous and Cenozoic volcanic rocks of the Chatham Islands, New Zealand: New Zealand Journal of Geology and Geophysics, v. 20, p. 425-467.
- Guidotti, C.V., 1969, A comment on "A chemical study of minerals from the Moine schists of the Ardnamurchan area, Argyllshire, Scotland" by B.C.M. Butler and its implications for the phengite problem: Journal of Petrology, v. 10, p. 164-170.

- _____, 1970, The mineralogy and petrology of the transition from the lower to upper sillimanite zone in Oquossoc area, Maine: *Journal of Petrology*, v. 11, p. 277-336.
- _____, 1973, Compositional variation of muscovite as a function of metamorphic grade and assemblage in metapelites from northwestern Maine: *Contributions to Mineralogy and Petrology*, v. 42, p. 33-42.
- _____, 1974, Transition from staurolite to sillimanite zone, Rangeley Quadrangle, Maine: *Geological Society of America Bulletin*, v. 85, p. 479-490.
- _____, 1978, Compositional variation of muscovite in medium to high grade metapelites of northwest Maine: *American Mineralogist*, v. 63, p. 878-884.
- _____, 1984, Micas in metamorphic rocks: in Bailey, S.W., editor, *Reviews in mineralogy*, v. 13 micas, Mineralogical Society of America, 1984, Washington, D.C.
- _____, and Sassi, F.P., 1976, Muscovite as a petrogenetic indicator mineral in pelitic schists: *Neues Jahrb. Mineralogie Abh.*, v. 127, p. 97-142.
- Harte, B., and Graham, C.M., 1975, The graphical analysis of greenschist to amphibolite facies mineral assemblages in metabasites: *Journal of Petrology*, v. 16, p. 347-370.
- Hashimoto, M., 1966, On the prehnite-pumpellyite metagraywacke facies: *Journal of the Geological Society of Japan*, v. 72, p. 253-265.
- _____, 1972, Reactions producing actinolite in basic metamorphic rocks: *Lithos*, v. 5, p. 19-31.
- Hay, R.F., Mutch, A.R., and Walter, W.A., 1970, Geology of the Chatham Islands: *New Zealand Geological Survey Bulletin* 23, 86 p.
- Hekinian, R., 1971, Petrological and geochemical study of spilites and associated rocks from St. John, U.S. Virgin Islands: *Geological Society of America Bulletin*, v. 82, p. 659-682.
- Hietanen, A., 1974, Amphibole pairs, epidote minerals, chlorite and plagioclase in metamorphic rocks, northern Sierra Nevada, California: *American Mineralogist*, v. 59, p. 22-40.
- Hildreth, Wes, 1981, Gradients in silicic magma chambers: Implication for lithospheric magmatism: *Journal of Geophysical Research*, v. 86, p. 10153-10197.
- Hey, M.H., 1954, A new review of the chlorites: *Mineralogical Magazine*, v. 30, p. 277-292.
- Holdaway, M.J., 1965, Basic regional metamorphic rocks in part of the Klamath mountains, northern California: *American Mineralogist*, v. 50, p. 953-977.
- Hollocher, K.T., 1981, Retrograde metamorphism of the Lower Devonian Littleton Formation in the New Salem area, west central Massachusetts: Contribution No. 37 (M.S. thesis), Department of Geology and Geography, University of Massachusetts, Amherst, 268 p.
- Hsu, L.C., 1968, Selected phase relations in the system Al-Mn-Fe-Si-O-H; A model for garnet equilibria: *Journal of Petrology*, v. 9, p. 40-83.

- Humphris, S.E., and Thompson, G., 1978, Hydrothermal alteration of oceanic basalts by seawater: *Geochemica et Cosmochemica Acta*, v. 42, p. 107-125.
- _____, and _____, 1978, Trace element mobility during hydrothermal alteration of oceanic basalts: *Geochemica et Cosmochemica Acta*, v. 42, p. 127-136.
- Kanehira, K., and Banno, S., 1960, Ferriphengite and aegirinejadeite in a crystalline schist of the Iimori district, Kii Peninsula: *Journal of the Geological Society of Japan*, v. 66, p. 654-659.
- Kawachi, Yosuke, 1975, Pumpellyite-actinolite and contiguous facies metamorphism in part of Upper Wakatipu District, South Island, New Zealand: *New Zealand Journal of Geology and Geophysics*, v. 18, p. 401-441.
- Korikovski, S.P., 1973, Changes in the composition of muscovite-phengite during metamorphism, in: *Phase equilibrium processes of mineral formation: Moscow, Nauka*, p. 71-95 (in Russian).
- Korzhinski, D.S., 1959, Physicochemical basis of the analysis of the parageneses of minerals: Consultants Bureau, New York, 142 p.
- Kretz, R., 1973, Kinetics of the crystallization of garnet at two localities near Yellowknife: *Canadian Mineralogist*, v. 12, p. 1-20.
- Kuniyoshi, S., and Liou, J.G., 1976, Contact metamorphism of the Karmutsen volcanics, Vancouver Island, British Columbia: *Journal of Petrology*, v. 17, p. 73-99.
- Laird, Jo, 1980, Phase equilibria in mafic schists from Vermont: *Journal of Petrology*, v. 21, p. 1-37.
- _____, and Albee, A.L., 1981, High pressure metamorphism in mafic schists from northern Vermont: *American Journal of Science*, v. 281, p. 97-126.
- Landis, C.A., and Bishop, D.G., 1972, Plate tectonics and regional stratigraphic and metamorphic relations in the southern part of the New Zealand Geosyncline: *Geological Society of America, Bulletin*, v. 83, p. 2267-2284.
- Leake, E., 1964, The chemical distinction between ortho- and para-amphibolites: *Journal of Petrology*, v. 5., p. 238-254.
- _____, 1978, Nomenclature of amphiboles: *Canadian Mineralogist*, v. 16, p. 501-520.
- Lee, D.E., Coleman, R.G., and Erd, R.C., 1962, Garnet types from the Cazadero area, California: *Journal of Petrology*, v. 4, p. 460-462.
- Liou, J.G., 1973, Synthesis and stability relations of epidote $\text{Ca}_2\text{Al}_2\text{FeSi}_3\text{O}_{12}(\text{OH})$: *Journal of Petrology*, v. 14, p. 381-413.
- _____, Kuniyoshi, S., and Ito, K., 1974, Experimental studies of the phase relations between greenschist and amphibolite facies in basaltic systems: *American Journal of Science*, v. 274, p. 613-632.
- _____, 1979, Zeolite facies metamorphism of basaltic rocks from the east Taiwan ophiolite: *American Mineralogist*, v. 64, p. 1-14.

- _____, Kim, Hyung, Shik, and Maruyama, Shingenori, 1983, Prehnite-epidote equilibria and their petrologic applications: *Journal of Petrology*, v. 24, p. 321-342.
- Loughnan, F.C., 1969, Chemical weathering of silicate minerals: American Elsevier Publishing Co. Inc., New York, 154 p.
- Mather, J.D., 1970, The biotite isograd and the lower greenschist facies in the Dalradian rocks of Scotland: *Journal of Petrology*, v. 11, p. 253-275.
- Maruyama, Shingenori, and Liou, J.G., 1985, The stability of Ca-Na pyroxene in low-grade metabasites of high-pressure intermediate facies series: *American Mineralogist*, v. 70, p. 16-29.
- Miyashiro, Akiho, and Seki, Yotaro, 1958, Enlargement of the compositional field of epidote and piemontite with rising temperature: *American Journal of Science*, v. 256, p. 423-430.
- Moll, Elizabeth J., 1981, Geochemistry and petrology of mid-Tertiary ash flow tuffs from the Sierra El Virulento area, eastern Chihuahua, Mexico: *Journal of Geophysical Research*, v. 86, p. 10321-10334.
- Moore, Diane E., and Liou, J.G., 1980, Detrital glaucophane schist pebbles from Franciscan metaconglomerate of the northeast Diablo Range, California: *American Journal of Science*, v. 280 p. 249-264.
- Mueller, George, and Schneider, Alfred, 1971, Chemistry and genesis of garnets in metamorphic rocks: *Contributions to Mineralogy and Petrology*, v. 31, p. 178-200.
- Nakajima, T., Banno, S., and Suzuiki, T., 1977, Reactions leading to the disappearance of pumpellyite in low-grade metamorphic rocks of the Sanbagawa metamorphic belt, central Shikoku, Japan: *Journal of Petrology*, v. 18, p. 263-284.
- _____, 1982, Phase relations of pumpellyite-actinolite metabasites in the Sanbagawa metamorphic belt in central Shikoku, Japan: *Lithos*, v. 15, p. 267-280.
- Nitsch, K.H., 1971, Stabilitätsbeziehungen von prehnit- und pumpellyithaltigen paragenesen: *Contributions to Mineralogy and Petrology*, v. 30, p. 240-260.
- Nockolds, S.R., 1954, Average chemical composition of some igneous rocks: *Geological Society of America Bulletin*, v. 65, p. 1007-1032.
- Norrish, K., and Chapple, B.W., 1967, X-ray fluorescence spectrography: in Zussman, Jack, ed., *Physical methods in determinative mineralogy*: Academic Press, New York, p. 161-214.
- Norrish, K., and Hutton, J.T., 1969, An accurate X-ray spectrographic method for the analysis of a wide range of geologic samples: *Geochemica et Cosmochemica Acta*, v. 33, p. 431-454.
- Nystrom, J.O., 1983, Pumpellyite-bearing rocks in central Sweden and extent of host rock alteration as a control of pumpellyite composition: *Contributions to Mineralogy and Petrology*, v. 83, p. 159-168.
- Osberg, P.H., 1971, An equilibrium model for Buchan type metamorphic rocks, south-central Maine: *American Mineralogist*, v. 56, p. 570-586.

- Passaglia, E., and Gottardi, G., 1973, Crystal chemistry and nomenclature of pumpellyite and julgoldite: *Canadian Mineralogist*, v. 12, p. 219-223.
- Pearce, J.A., and Cann, J.R., 1972, Tectonic setting of basic volcanic rocks determined using trace element analysis: *Earth and Planetary Science Letters*, v. 19, p. 290-300.
- Pearce, J.A., and Norry, M.J., 1979, Petrogenetic implications of Ti, Zr, Y, and Nb variations in volcanic rocks: *Contributions to Mineralogy and Petrology*, v. 69, p. 33-47.
- Raith, Michael, 1976, The Al-Fe(III) epidote miscibility gap in the metamorphic profile through the Perinee series of the Tauern window, Austria: *Contributions to Mineralogy and Petrology*, v. 57, p. 99-117.
- Reed, J.J., 1957, Petrology of the lower Mesozoic rocks of the Wellington district: *New Zealand Geological Survey Bulletin*, M.S. 57, 60 p.
- Robinson, Peter, and Jaffe, H.W., 1969, Chemographic exploration of amphibole assemblages from central Massachusetts, and south-western New Hampshire: *Mineralogical Society of America Special Paper No. 2*, p. 251-274.
- Robinson, Peter, Spear, F.S., Schumacher, J.C., Laird, Jo, Klein, C., Evans, B.W., and Doolan, B.L., 1982, Phase relations of metamorphic amphiboles: natural occurrence and theory: *in* Veblen, D.R., and Ribbe, P.H., eds. *Reviews in mineralogy*, vol. 9B. *Amphiboles: petrology and experimental phase relations*: Mineralogical Society of America, Washington, D.C. p. 1-227.
- Rumble, D., III, 1977, Mineralogy and petrology and oxygen isotopic geochemistry of the Clough Formation, Black Mountain, western New Hampshire, U.S.A.: *Journal of Petrology*, v. 19, p. 319-340.
- Schiffman, Peter, and Liou, J.G., 1980, Synthesis and stability relations of Mg-Al pumpellyite $\text{Ca}_4\text{Al}_5\text{MgSi}_6\text{O}_{21}(\text{OH})_7$: *Journal of Petrology*, v. 21, p. 441-474.
- Schumacher, J.C., 1983, Stratigraphic, geochemical, and petrologic studies of the Ammonoosuc Volcanics, north central Massachusetts, and southwestern New Hampshire: Ph.D. dissertation, University of Massachusetts, Amherst, 273 p.
- Scott, R.B., 1971, Alkali exchange during devitrification and hydration of glasses in ignimbrite cooling units: *Journal of Geology*, v. 79, p. 100-110.
- Seki, Yotaro, 1961, Pumpellyite in low-grade metamorphism: *Journal of Petrology*, v. 2, p. 407-423.
- _____, 1969, Facies series in low-grade metamorphism: *Journal of the Geological Society of Japan*, v. 75, p. 255-266.
- Shearer, C.K., 1983, Petrography, mineral chemistry, and geochemistry of the Hardwick Tonalite and associated igneous rocks, central Massachusetts. Ph.D. thesis, University of Massachusetts, Amherst, 265 p.
- Shoji, T., 1975, Role of temperature and CO_2 pressure in the formation of skarn and its bearing on mineralization: *Economic Geology*, v. 70, p. 739-740.

- Sparks, R.S.J., Self, S., and Walker, G.P.L., 1973, Products of ignimbrite eruptions: *Geology*, v. 1, p. 115-118.
- Spear, F.S., 1982, Phase equilibria of amphibolites from the Post Pond volcanics, Mt. Cube Quadrangle, Vermont: *Journal of Petrology*, v. 23, p. 383-426.
- Spry, A., 1969, *Metamorphic textures*: Pergamon, Oxford.
- Stephens, M.B., Glasson, M.J., and Keays, R.R., 1976, Structural and chemical aspects of metamorphic layering development in metasediments from Clunes, Australia: *American Journal of Science*, v. 279, p. 129-160.
- Stout, J.H., 1978, Phase petrology and mineral chemistry of coexisting amphiboles from Telemark, Norway: *Journal of Petrology*, v. 13, p. 99-145.
- Strens, R.G.J., 1965, Stability relations of the Al-Fe epidotes: *Mineralogy Magazine*, v. 35, p. 464-475.
- Surdam, R.C., 1969, Electron microprobe study of prehnite- and pumpellyite from the Karmutsen group, Vancouver Island, British Columbia: *American Mineralogist*, v. 54, p. 256-266.
- Thompson, J.B., Jr., 1957, The graphical analysis of mineral assemblages in pelitic schists: *American Mineralogist*, v. 42, p. 842-858.
- _____, 1979, Tschermak replacement and reactions in pelitic schists: in *Problems of physical and chemical petrology*, v. 1, p. 146-159 (in Russian).
- Tracy, R.J., 1978, High-grade metamorphic reactions and partial melting of pelitic schist, west central Massachusetts: *American Journal of Science*, v. 278, p. 150-178.
- Trzcienski, W.E., and Birkett, T.C., 1982, Compositional variation of pumpellyite along the western margin of the Quebec Appalachians: *Canadian Mineralogist*, v. 20, p. 203-209.
- van der Plas, L., 1959, Petrology of the northern Adula region, Switzerland: *Leidse-Geol. Med.*, v. 24, p. 415-602.
- Velde, Bruce, 1965, Phengitic micas, synthesis, stability, and natural occurrence: *American Journal of Science*, v. 263, p. 886-913.
- Wellman, H.W., 1952, The Permian-Jurassic stratified rocks: in *Symposium sur les series de Gondwana (Nouvelle-Zelande)*, International Geological Congress, 19th, Algiers, 1952. p. 13-24.
- Wise, W.S., and Eugster, H.P., 1964, Celadonite: synthesis, thermal stability, and occurrence: *American Mineralogist*, v. 49, p. 1021-1083.
- Zen, E-an, 1963, Components, phases, and criteria of equilibria in rocks: *American Journal of Science*, v. 261, p. 929-942.
- _____, 1974, Prehnite- and pumpellyite bearing mineral assemblages west side of the Appalachian metamorphic belt, Pennsylvania to Newfoundland: *Journal of Petrology*, v. 15, p. 197-242.

